Synthesis and Surface Modification of Luminescent Nanocrystals: Their Performance and Potential as Optical Bioimaging Agents

by

Jothirmayanantham Pichaandi
B.Tech., Chemical Technology, Nagpur University, 2003
M.Tech., Polymer Engineering and Science, Mumbai University, 2005

A Dissertation Submitted in Partial Fulfillment
of the Requirements for the Degree of

DOCTOR OF PHILOSOPHY
in the Department of Chemistry

University of Victoria

Supervisory Committee

Synthesis and Surface Modification of Luminescent Nanocrystals: Their Performance and Potential as Optical Bioimaging Agents

by

Jothirmayanantham Pichaandi

B.Tech., Chemical Technology, Nagpur University, 2003

M.Tech., Polymer Engineering and Science, Mumbai University, 2005

Supervisory Committee

Dr. Ir. Franciscus C. J. M. van Veggel (Department of Chemistry)

Supervisor

Dr. David A. Harrington (Department of Chemistry)

Departmental Member

Dr. Dennis K. Hore (Department of Chemistry)

Departmental Member

Dr. Robert D. Burke (Department of Biochemistry and Microbiology)

Outside Member

Abstract

Supervisory Committee

Dr. Ir. Franciscus C. J. M. van Veggel (Department of Chemistry)

Supervisor

Dr. David A. Harrington (Department of Chemistry)

Departmental Member

Dr. Dennis K. Hore (Department of Chemistry)

Departmental Member

Dr. Robert D. Burke (Department of Biochemistry and Microbiology)

Outside Member

In this thesis, luminescent lanthanide-doped nanocrystals, and lead-based quantum dots nanocrystals are explored as alternative bioimaging agents to fluorescent proteins and organic fluorophores for deep-tissue imaging. The first chapter gives a brief introduction on the aforementioned nanocrystals and their special optical properties. In chapter 2 the simple changes in the drying and baking temperature of the Yb^{3+} and Ho^{3+} doped LaF_3 nanocrystals-silica sol-gel mixture aid in the explanation of the formation of two types of silica. The difference in the phonon energies of the two types of silica is found to control effectively the ratio of red to green emissions obtained from the upconversion process. However, the nanocrystals do not disperse in water making them unsuitable for bioimaging. Chapter 3 describe the synthesis of $NaYF_4$ nanocrystals doped with Yb^{3+}/Er^{3+} or Yb^{3+}/Tm^{3+} ions followed by two surface modification strategies (intercalation and crosslinking) to disperse them in physiological buffers and biological growth media. Of the two methods, the crosslinked polymer coating of the nanocrystals

alone exhibits stability in aforementioned media. In chapter 4 the applicability of lanthanide-doped $NaYF_4$ nanocrystals are studied as bioimaging agents in two-photon upconversion laser scanning microscopy for deep-tissue imaging. Their performance as bioimaging agents was not better than fluorescent proteins and organic molecules. On the other hand with two-photon upconversion wide field microscopy (TPUWFM), brain blood vessels over a depth of 100 µm could well be separated. Furthermore, with the 800 nm emission from Tm^{3+} ions one can image twice as deep as the green emission with TPUWFM. In chapter 5, probing the $NaYF_4$ nanocrystals with energy-dependent XPS shows that, the Y^{3+} ions on the surface of the nanocrystals are different from the ones present inside the nanocrystals. This chapter is concluded with a preliminary investigation of Yb^{3+} and Tm^{3+} doped $NaYF_4$ with resonant XPS. Chapter 6 examines four different types of surface modification strategies to transfer hydrophobic lead-based quantum dots to physiological buffers and biological growth media. Of the four methods, the crosslinked polymer coating of quantum dots alone exhibits colloidal stability and the QDs retain their luminescence in aforementioned media over several months. The conclusions and future outlook for the work are elucidated in chapter 7.

Table of Contents

List of Tables

List of Figures

Abbreviations

BHMT	Bis(hexamethylene)triamine
CLS	Canadian Light Source
CW	Continuous Wave
EDS	Energy Dispersive X-ray Spectroscopy
EELS	Electron Energy-Loss Spectroscopy
E_g	Energy Gap
ESA	Excited State Absorption
EPR	Electron Paramagnetic Resonance
ET	Energy Transfer
eV	Electron Volt
FTIR	Fourier Transform Infrared Spectroscopy
GSA	Ground State Absorption
HAADF	High Angle Annular Dark Field Imaging
HF	Hydrofluoric Acid
IR	Infrared
IMFP	Inelastic Mean Free Path
LEET	Looping Enhanced Energy Transfer
Ln	Lanthanide
MBE	Molecular Beam Epitaxy
MOCVD	Metal Organic Chemical Vapor Deposition
MRI	Magnetic Resonance Imaging
NMR	Nuclear Magnetic Resonance
ODE	Octadecene
OA	Oleic Acid
PEG	Polyethyleneglycol
PL	Photoluminescence
PMAO	Poly(maleicanhydride-*alt*-1-octadecene)
PMT	Photo-Multiplier Tube

PVP	Polyvinylpyrrolidone
QDs	Quantum dots
SANS	Small Angle Neutron Scattering
SEM	Scanning Electron Microscopy
SGM	Spherical Grating Monochromator
SILAR	Successive Ion Layer Adsorption and Reaction
TCE	Tetrachloroethylene
TEM	Transmission Electron Microscopy
TEOS	Tetraethyl Orthosilicate (Tetraethoxysilane)
TGA	Thermogravimetric Analysis
$(TMS)_2S$	Bis(trimethylsilyl) sulfide
TOP	Trioctylphopshine
TPLSM	Two-Photon Laser Scanning Microscopy
TPULSM	Two-Photon Upconversion Laser Scanning Microscopy
TPUWFM	Two-Photon Upconversion Wide Field Microscopy
UV	Ultra-Violet
XPS	X-ray Photoelectron Spectroscopy
XRD	X-ray Diffraction

Acknowledgments

Every student needs a mentor and teacher to achieve his target. I am blessed with a mentor and teacher in Prof. Frank C. J. M. Van Veggel who taught me how to think and fearlessly explore new avenues. He once told me don't fear failure; rather take it as an opportunity to learn from those mistakes and failures. I am very much like the excited ions of lanthanides with long lifetimes in the excited state. He advised me that optimum time at the excited state is essential rather than a long or short time there. My stay in his group has taught me to be patient and persevere at all situations. I am indebted to him, for all his guidance and patience, during the 6 years of my stay in his group.

I would like to express my gratitude to Prof. Kerry Delaney for all his help in performing the *in-vivo* experiments in chapter 4. He stayed till midnight for quite a few days to help me finish the experiments. His passion for research ingrained in me the aspect that I need to be passionate, focussed, and unrelenting to succeed. I would say that he is my second advisor. A special thanks to all his group members for all their help.

My work at the Canadian Light Source would not have been possible without the help of Tom Regier and David Chevrier. Thank you, Tom and Dave for all your help and guidance at the beamline.

My special thanks to Prof. Mati Raudsepp for performing quite a few XRD measurements on samples and their Rietveld refinements on them.

I thank my committee members Prof. David Harrington and Prof. Dennis Hore all their helpful suggestions and discussions.

My special gratitude towards my external committee member Prof. Robert Burke. His suggestions and help in imaging the LNCaP cells with upconverting nanocrystals were invaluable. I wish to thank Prof. Jonathan G. C. Veinot from University of Alberta for agreeing to be my external examiner for my oral defense.

Research environment should be conducive which was provided by my group members. Thank you all for putting up with all my idiosyncrasies and making my stay a memorable one. I will definitely not forget the discussions and arguments about research topics, to movies, to world politics. Without my former and my current group members, research environment would have been boring.

I would like to extend my heartfelt thanks to my Petch labmates (Moffitt group members). Without the instrument and machine shop technicians and chemistry stores people, my thesis work would not have been a smooth ride. Thank you all for your help.

My special thanks to Archanaji, Prashantji, Vikram bhai, Jasleenji, Ishita, Kailashji, Akshayji, Sriramji, Jerome, Nirmala, Ram, and Varun. I learnt a lot from you all in terms of research and life. My life outside research would not have been fun without you people.

I should mention that my housemate Ilamparithi made my stay with him pleasant and intellectually stimulating for the past 4 years.

My lifelong friends Nikhil, Pradeep, Piyush, Naren, Prashant, Deepak, Amrit, and Karthicks helped me in my most difficult times.

Furthermore I could not have done this without the constant support and guidance from my family. I cannot imagine a better family than the one I have got.

Last but not the least I find my inspiration and imagination from the lives of my three most favorite scientists: Albert Einstein, Marie Curie, and A. P. J. Abdul Kalam.

Dedication

To

Amma & Appa

.

Chapter 1. Introduction

Nanocrystals are particles in the size regime of 1 to 100 nm that often show unique properties in this size regime when compared to their atomic and bulk counterparts. The small size and unique properties make them attractive for a variety of applications ranging from electronics, coatings, aviation, security labels, photovoltaics, cosmetics, and bioimaging contrast agents.[1-7] The first known nanocrystals were gold colloids, which date back to 5th century when humans used it for medicinal purposes. After this, the Romans employed gold colloids to color glass and ceramics.[8] Various sizes of gold colloids were used to achieve different colors for coating (e.g. window coloring).[9] The different colors employed by Romans for coloring the windows can be explained by the size-dependence surface plasmon effect of gold colloids at the nanoscopic level. Interestingly, at both those times human beings did not know that that they were making gold colloids in the nano-size regime. In the mid 19th century, the famous scientist Michael Faraday discovered that the gold applied for coloring glass and ceramics were colloids and that they were small.[8] He explained that these were gold nanocrystals and they change their color depending on the size. This could be called as the beginning of nanotechnology. In 1951 Turkevich developed the first modern synthesis gold nanocrystals through a reduction process.[10] The advent of quantum mechanics and transistors in the mid 20th century propelled many scientists to explore matter at the nanoscopic level. This was further fuelled by the famous statement made by the physicist Richard Feynman's statement "There is plenty of room at the bottom".[11]

Around the end of 1980's, Mark Reed a scientist from Yale university coined the term quantum dots for small semiconductor nanocrystals (< 10 nm) due to their size dependence optical properties, which could only be explained by quantum mechanics.[12] This kick-started the revolution of nanocrystal synthesis of several materials like gold, silver, iron oxide, cobalt, platinum, semiconductor quantum dots, and many more. These nanocrystals could be applied in a variety of fields. In the last decade, attention has been given towards the medicinal applications of nanocrystals. For example, gold and silver colloids have been found to be applicable as therapeutic agents.[13] In addition, iron oxide, and gadolinium-based nanocrystals have shown great potential as clinical MRI imaging agents.[14-15] Furthermore, CdSe/ZnS core/shell quantum dots have been shown to be better optical imaging agents (reduction in photobleaching, photooxidation and low autofluorescence, high signal to noise ratio) which could be a potential replacement for organic molecules and fluorescent proteins.[16]

The goal of this thesis is to explore alternative optical imaging agents for deep-tissue bioimaging (> 500 μm). The first question to arise is why there is a necessity to develop alternatives for fluorescent proteins and organic molecules. The advantage of using fluorescent proteins and organic molecules is that they have a high quantum yield (> 90 % for one-photon and two-photon absorption) coupled with the ability to be conjugated to bio-molecules.[17-20] In case of fluorescent proteins they can be expressed genetically in cells. Both these class of molecules could be used to image up to a depth of 500 μm inside the brain of a mouse without the loss of resolution (capillaries smaller than 10 μm) of the image.[21] The imaging is done using two-photon laser scanning microscopy

(TPLSM) with organic molecules or fluorescent proteins as imaging agents. The advantage of using two-photon absorption is that the emission comes from the point of focus alone and not either from above or below the focus. The difference between the one- and two-photon processes can be seen clearly in Figure 1.1. This aid in resolving structures separated by a depth of 10 to 20 μm clearly as imaging is performed inside a tissue.[22] This is possible because the two-photon process occurs only at high power density which is provided only at the focal point. The two-photon absorption occurs only when two photons of equal or different energies (generally near-IR photons) are simultaneously absorbed by the fluorophore to go from the ground state to the excited state. When the fluorophore relaxes to the ground state they give out a higher-energy photon (generally visible photons) in the process. The probability of simultaneous absorption of the two photons by a fluorophore is a low, because it happens within a space of few femtoseconds. The high power densities and femtosecond time frame for the process is generally provided by an expensive femtosecond laser.[23]

However, there are several disadvantages encountered when these molecules are used as optical bioimaging agents. Organic molecules and fluorescent proteins photo-bleach fast (less than an hour) and the power densities required for the two-photon absorption cause photo-damage. Moreover, the emitted visible light (generally green and red light) from two-photon and one-photon absorption gets absorbed and scattered by tissues and cells. Therefore, there is the necessity to develop materials which have overcome the aforementioned obstacles faced by organic molecules and fluorescent proteins and still have most of the advantages of these molecules. Two types of nanocrystals are proposed

in this thesis as alternative imaging agents; 1) lanthanide-doped nanocrystals; 2) lead-based quantum dots (PbSe and PbS).

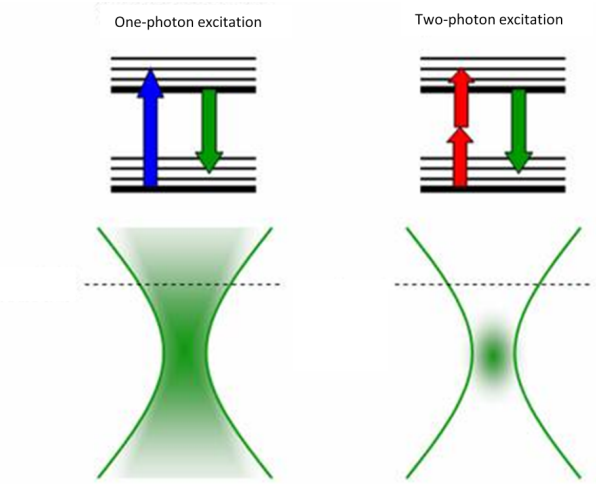

Figure 1.1. Difference between one- and two-photon absorption microscopy. In the one-photon process emission comes from out of focus planes as well where as in the two-photon process emission comes only from the focus spot.

1.1 Lanthanides

In the last decade, lanthanide-doped nanocrystals have been explored for their unique optical properties. The optical properties of the lanthanide ions stem from the forbidden 4f-4f transitions. Lanthanides lie near the bottom of the Periodic Table along with the actinides. The lanthanides, along with yttrium and scandium were thought to be rare-earth elements because they were hard to separate and purify from their ores. However, the abundance of these elements in China and Canada coupled with the efficient present purification methods has made the name rare-earth elements a misnomer. These lanthanide ions have known to be applicable in optical amplifiers (Er^{3+})[24], supermagnets

(Nd^{3+})[25], MRI contrast agents (Gd^{3+})[26], lasers (Nd^{3+})[27], lighting phosphors (Ce^{3+}, Eu^{3+})[28], and catalysts (Ce^{3+}, Ce^{4+}, Y^{3+}, Lu^{3+}, Sc^{3+})[29]. Most recently, lanthanide-doped nanocrystals have attracted attention due to their potential as a bioimaging agent. In general, lanthanides ions are doped in optically inactive matrices to use their photoluminescence properties. The most common nanocrystal matrices for doping lanthanides are LaF_3, La_2O_3, Y_2O_3, $LaPO_4$, $NaYF_4$, $NaGdF_4$, and $LiYF_4$. Lanthanides show high affinity towards oxides and fluorides due to their high electronegativity.[28] The high affinity towards electronegativity is exploited by doping them in oxide and fluoride matrices. In addition to this, fluoride matrices have low phonon energies (300 to 500 cm^{-1}). Due to the low phonon energy, there is a reduction in the quenching of the emission.

Hence the lanthanides studied in this thesis were all doped in a fluoride matrix to take advantage of their low phonon energy. The energy levels and most important optical transitions of the lanthanides are given in Figure 1.2 and Table 1.1 respectively. The interactions between the $4f^n$ electrons, (i.e. Coloumb repulsion and spin-orbit coupling) in the lanthanides lead to the energy levels shown in Figure 1.2. When the lanthanide ion is incorporated in a crystal the electric field of the ligands produce a crystal field, which splits the multiplets from the spin-orbit coupling into crystal field levels or Stark levels. Due to the interaction between the $4f^n$ electrons and the electric field, the crystal field splitting is small (up to a few hundred cm^{-1}). The energy levels are named by the Russell-Saunders notation, $^{(2S+1)}\Gamma_J$ where 2S+1 is the spin multiplicity with S being the total spin of the 4f electrons, Γ is the total angular momentum, and J is the total angular momentum quantum number.

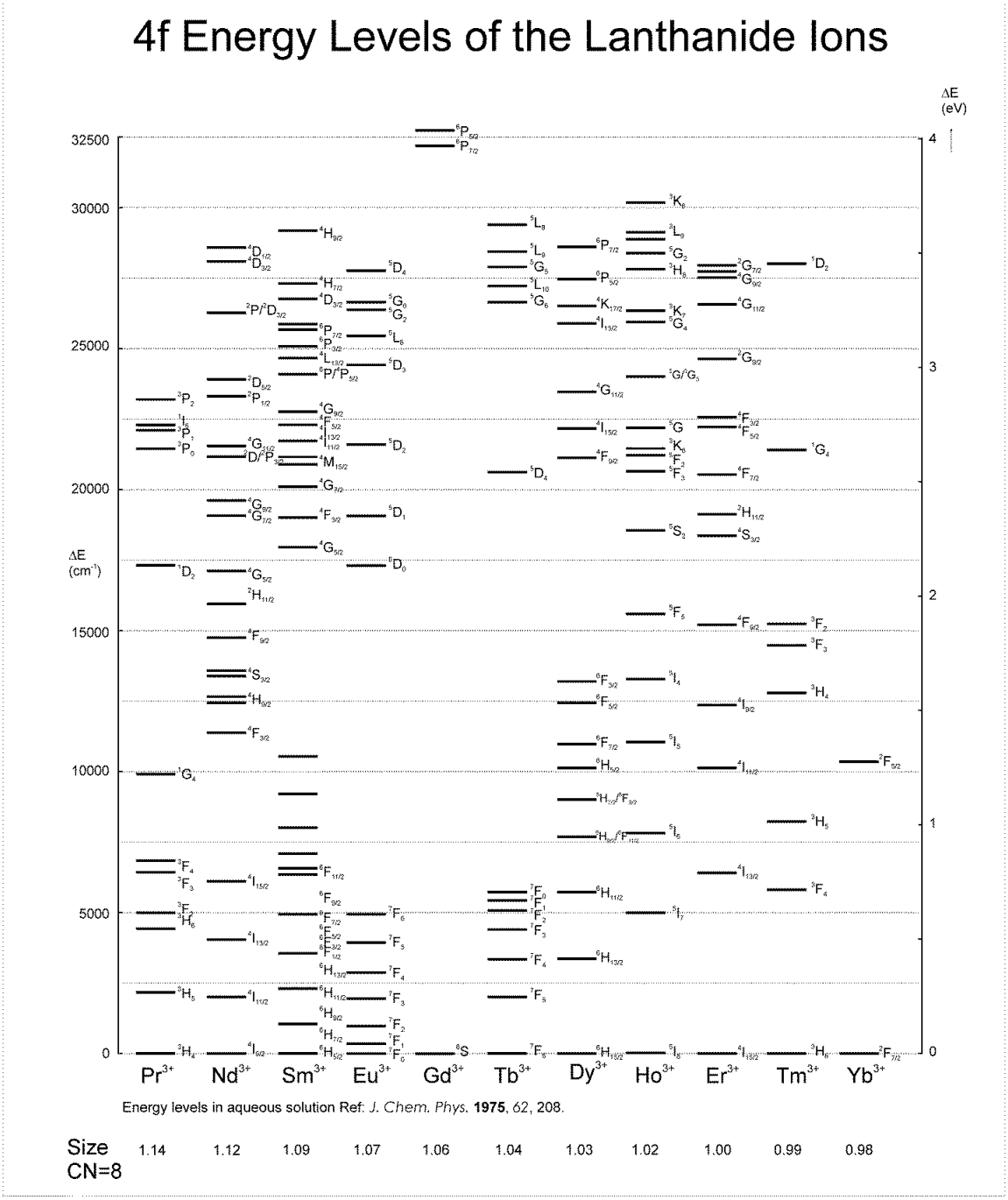

Figure 1.2. Energy level of lanthanide ions in aqueous solution (the sizes are taken from *CRC Handbook of Chemistry and Physics*).

Table 1.1. Most important transition emission lines of lanthanide ions.

Lanthanide ion	Transition	Wavelength (nm)
Pr^{3+}	$^1G_4 - {}^3H_5$	1330
Nd^{3+}	$^4F_{3/2} - {}^4I_{11/2}$	1064
Eu^{3+}	$^5D_0 - {}^7F_1$, $^7F_2$	591 and 612
Tb^{3+}	$^5D_4 - {}^7F_5$	545
Dy^{3+}	$^6F_{11/2} + {}^6H_{9/2} - {}^6H_{15/2}$	1330
Ho^{3+}	$^5S_2 - {}^5I_8$ $^5F_5 - {}^5I_8$	540 654
Er^{3+}	$^4S_{3/2} - {}^4I_{15/2}$ $^4F_{9/2} - {}^4I_{15/2}$ $^4I_{13/2} - {}^4I_{15/2}$	540 654 1550
Tm^{3+}	$^1D_2 - {}^3F_4$ $^1G_4 - {}^3H_6$ $^3H_4 - {}^3H_6$ $^3H_4 - {}^3F_4$	450 475 800 1480
Yb^{3+}	$^2F_{5/2} - {}^2F_{7/2}$	980

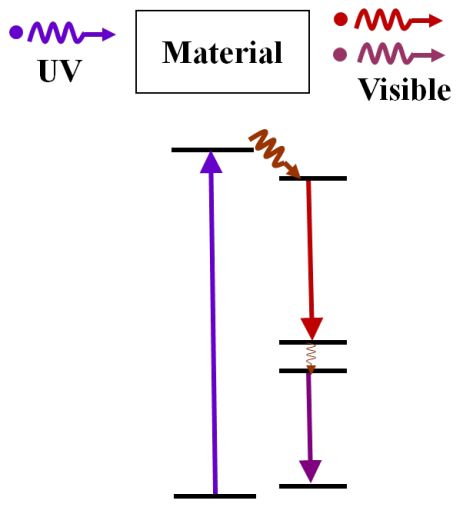

A

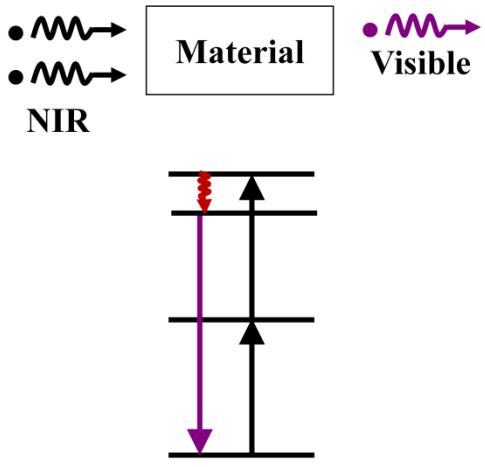

B

Figure 1.3. (A) Downconversion Process (B) Upconversion Process.

One of the interesting aspects about lanthanides is that they are known to upconvert and downconvert light. Upconversion is a process which converts two or more lower-energy photons to one higher-energy photon generally through a step-wise two-photon process. This is the process which will be exploited for bioimaging. The advantages of using lanthanides for this process are explained in detail in chapter 2, 3, and 4. Downconversion is the process in which one higher-energy photon is converted into two or more lower-energy photons. A representative schematic process for both these processes is shown in Figure 1.3. In the next section upconversion process will be explained in detail.

1.1.1 Upconversion

There are five types of upconversion processes: 1) ground state/excited state absorption; 2) energy transfer upconversion mechanism; 3) co-operative upconversion process; 4) photon- avalanche upconversion process; 5) Hetero-LEET upconversion mechanism

Ground state/excited state absorption (GSA/ESA)

This is the simplest of all the four upconversion mechanisms. It involves a single lanthanide ion and a sequential step-wise multi-photon absorption process. The lanthanide ion is excited to a long-lived or meta-stable intermediate energy level, followed by the absorption of one more photon to push the lanthanide ion to a higher excited state energy level. The lanthanide ion then usually relaxes to a meta-stable level or the ground level giving out a higher-energy photon in the process. This is different from the two-photon absorption process observed for an organic molecule. In the two-photon absorption process for an organic molecule, the simultaneous absorption of the

two lower-energy photons has to happen within a very short time frame (~ few femtoseconds). This reduces the probability of this process resulting in the necessity for a high power density (~10^5 W/cm^2). This process is normally achieved using a femtosecond laser. The biggest advantage of the GSA/ESA process is that it does not require a high power density to kick-start the process. The reason is due to the fact the lanthanide ion is excited to an actual meta-stable state (up to several milliseconds) rather than a virtual state in the case of a typical two-photon absorption process. The long-lived first excited state of the lanthanide ion provides ample time for it to absorb a second photon to go to a higher excited state.

In addition, due to the long-lived meta-stable energy level, this process can be performed using a cheap continuous wave diode laser to excite the lanthanide ions to their excited state. Like the two-photon absorption process for an organic molecule, the GSA/ESA also exhibits a quadratic power dependence for the emission process with respect to its excitation power. Er^{3+} and Ho^{3+} ions are the best example to observe this process. Many research groups have studied this mechanism in various oxide and fluoride matrices.[30-34] A schematic representation in Figure 1.3B explains the GSA/ESA process clearly. This process generally occurs when the dopant concentration of the lanthanide ion is low. If the concentration of the doped lanthanide ion (Er^{3+}, Ho^{3+}) goes up, other than ESA/GSA process, energy transfer between the ions is also observed. The next section will explain the energy transfer process in detail.

Energy transfer upconversion mechanism

The upconversion mechanism is similar to the ESA/GSA process. The difference here is that instead of the one lanthanide ion there will be at least two lanthanide ions involved. The lanthanide ion in the first excited state transfers its energy to its neighboring ion (energy transfer ET1) which then absorbs another photon from a nearby excited lanthanide ion (energy transfer ET2) to move to a higher-energy state Figure 1.4. From there it relaxes to a lower-energy state giving out a higher-energy photon in the process. A schematic representation is shown below to elucidate the process. This energy transfer upconversion mechanism was given its name by Auzel in 1966.[35] This process can happen between the same lanthanide ions as well. If two different lanthanide ions are used, the lanthanide ion that transfers its energy is called the sensitizer or the donor. The ion that accepts the energy is called the acceptor.

The best example for this process is codoping Yb^{3+} with Er^{3+}, or Tm^{3+} or Ho^{3+} ions.[34,36-38] After the first step in the process, the long-lived $^2F_{5/2}$ excited state of Yb^{3+} ion transfers its energy to a nearby Er^{3+} ion. The excited Er^{3+} ion absorbs one more photon from a different Yb^{3+} ion or the same to go to the next excited state. The primary reason for choosing Yb^{3+} as the sensitizer (donor) is because it has a higher absorption cross-section area (10^{-20} cm^2) when compared to other lanthanide ions (typically 10^{-21} cm^2 or less).[39] The higher absorption cross-section area and meta-stable $^2F_{5/2}$ of Yb^{3+} makes it a perfect candidate to be used as a sensitizer among all lanthanides for the energy transfer upconversion process.

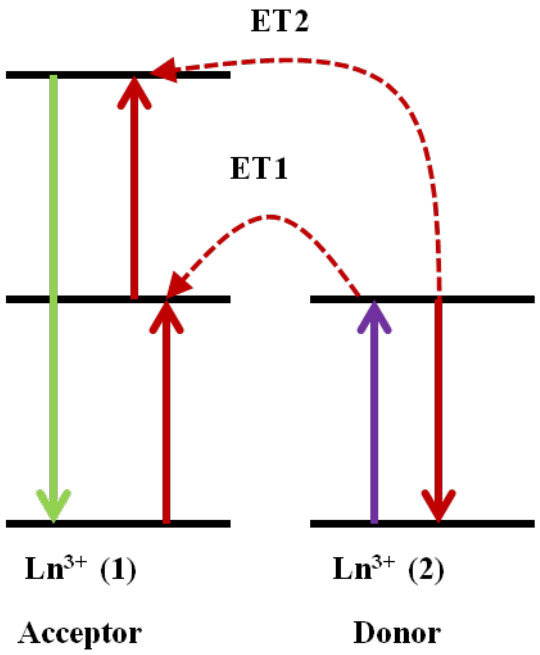

Figure 1.4. Schematic representation of energy transfer upconversion mechanism.

Co-operative upconversion mechanism

Co-operative mechanism is the process where two excited state sensitizer ions from a meta-stable level simultaneously transfer their energy to the acceptor ion to transfer it to a higher excited energy level from where it comes down to the ground state releasing a higher-energy photon in the process (Figure 1.5).[40] This can be of two types: 1) co-operative upconversion mechanism involving the same lanthanide ions; 2) sensitized co-operative upconversion mechanism. A simple cooperative mechanism happens when two Yb^{3+} ions simultaneously give its energy to another Yb^{3+} ion to help it reach a virtual state. From there the excited Yb^{3+} ion relaxes to the ground state giving out a higher-energy photon in the process. The sensitized co-operative mechanism can be observed when Eu^{3+} or Tb^{3+} is codoped with Yb^{3+} in a matrix. Two Yb^{3+} ions in the excited $^2F_{5/2}$

state transfer their energy simultaneously to Tb^{3+} or Eu^{3+} ion.[41-43] Following this, the Eu^{3+}, or Tb^{3+} ion then relaxes down giving out visible light in the process. The probability of two Yb^{3+} transferring their energy to a nearby Tb^{3+} or Eu^{3+} ions is low when compared to simple energy transfer between Yb^{3+} and Er^{3+} or Tm^{3+} or Ho^{3+} ion. Researchers have estimated that the co-operative process is 130 times weaker than the normal upconversion energy transfer process (Yb^{3+}/Er^{3+} or Ho^{3+} or Tm^{3+}).[44]

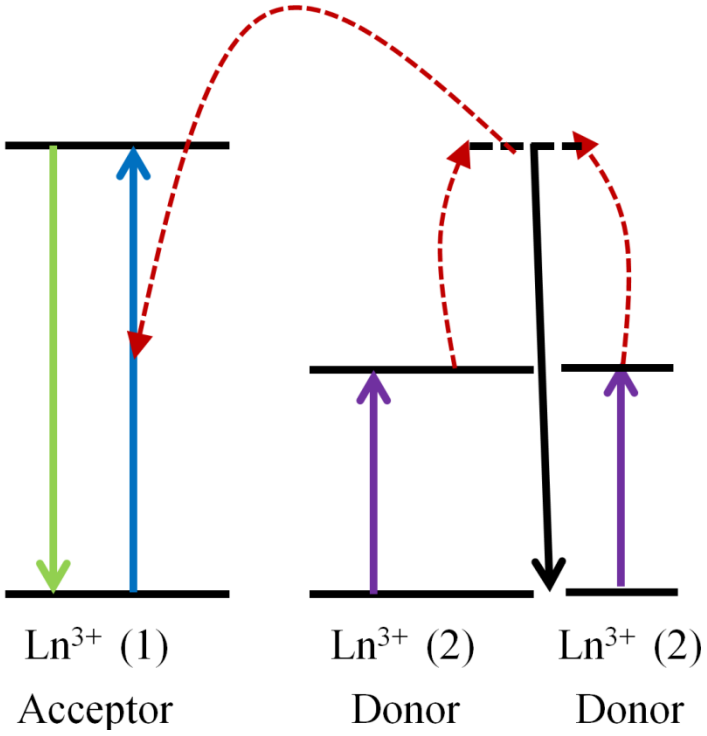

Figure 1.5. Schematic representation of co-operative upconversion mechanism.

Photon-avalanche upconversion process

This is the most recent upconversion process discovered in Pr^{3+} doped $LaCl_3$ or $LaBr_3$ crystals.[45-46] This is a process in which the first step is a *non-resonant* ground state absorption followed by resonant energy transfer absorption process. The difference is

instead of relaxing to the ground state the lanthanide ion in the second excited state reaches the meta-stable state due to an efficient cross-relaxation process. During the relaxation process the lanthanide ion transfers its energy to a nearby lanthanide ion through a cross-relaxation process to bring it to the metastable state from its ground state. Due to this process there are now two ions in the key meta-stable state which get excited to the second excited state again through resonant ESA process. Again these two ions relax to the first excited state bringing two more ions to meta-stable state. This process of looping goes on populating the first excited level which is similar to population inversion in a lasing process. That's why this is called a photon avalanche process (Figure 1.6).

This process happens only beyond a threshold pump power. The process is non-linear and can be confirmed from a power dependence graph where the slope is more than two (could be a number around 8 to 10 depending on the lanthanide) at the inflection point indicating a step-wise two-photon process.[47-48] The graph will look like an S-shaped curve for the photon avalanche process. After a certain power density the process gets saturated and slope starts falling down. A detailed pictorial representation of the process is shown in Figure 1.6. The limitation of the process is that it depends on a *non-resonant* GSA and a resonant ESA process of which the 1st process is inefficient when compared to the energy transfer upconversion process. Furthermore this photon avalanche process is slow to start with (up to minutes) when compared to the other processes as it requires a threshold laser-power for the looping process to start. This process can also occur when a sensitizer is used (Figure 1.7). There is a similar process called Hetero-LEET which also involves this kind of looping process. This report was reported by our group in LaF_3

doped with Yb^{3+} and Er^{3+} embedded in a silica thin film.[49] The mechanism was much more efficient due to the fact that the power density required to achieve the looping process was just around 5 W/cm^2. The increase in slope can be observed in Figure 1.8.

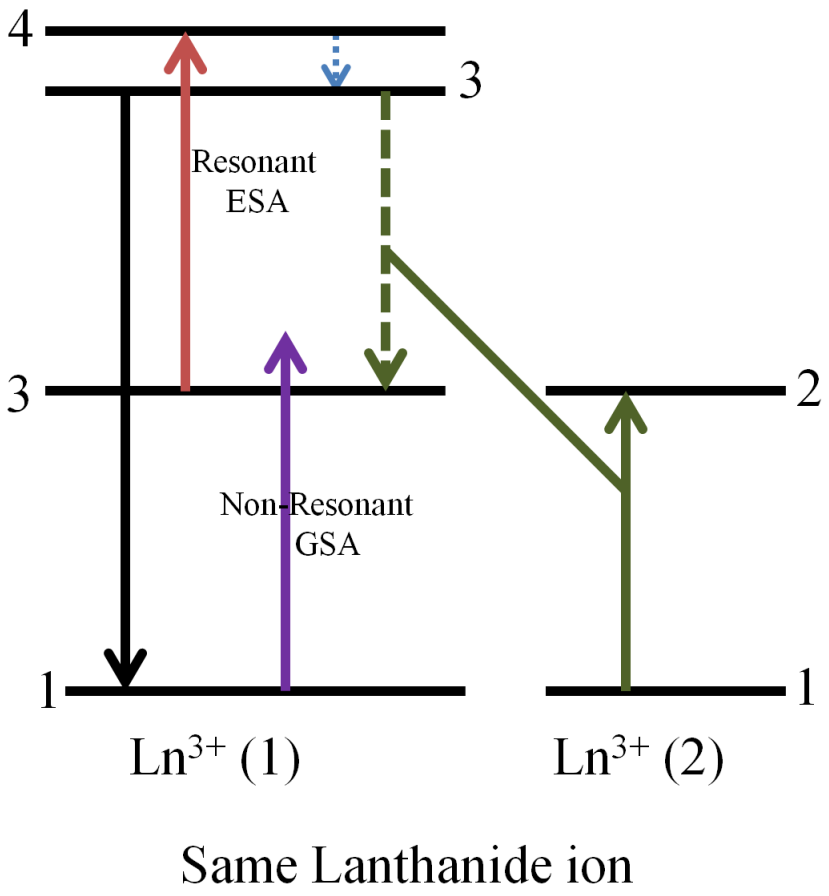

Figure 1.6. Schematic representation of the photon avalanche process.

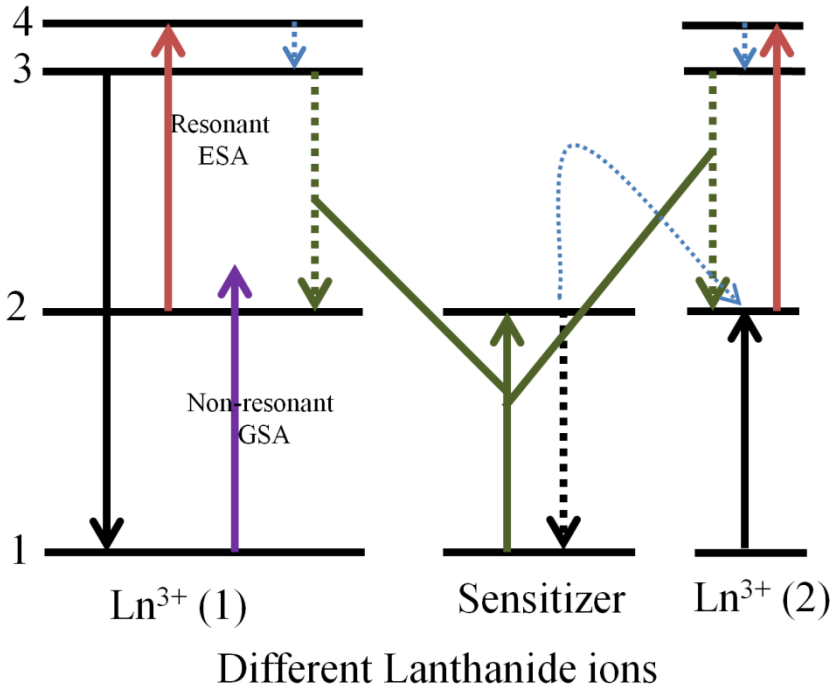

Figure 1.7. Schematic representation of the sensitized photon avalanche process.

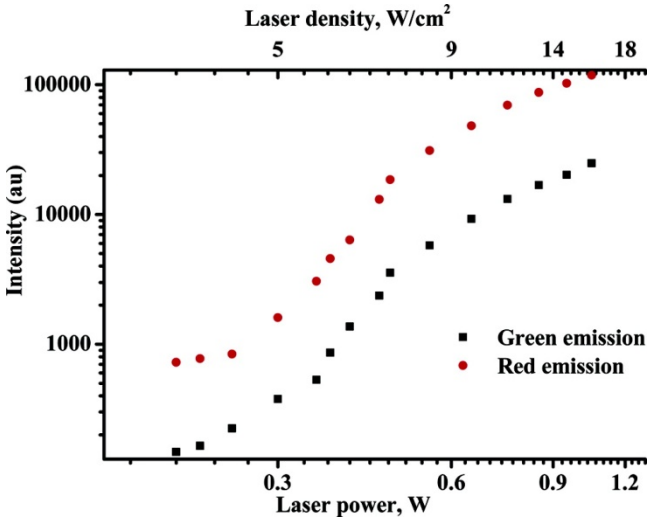

Figure 1.8. Power dependence curve for the Hetero-LEET mechanism.

Utilizing upconversion for bioimaging

Energy transfer upconversion from lanthanide-doped nanocrystals can be used as imaging agents and has several advantages over fluorescent proteins and organic molecules. In this thesis the process will just be called upconversion. The step-wise two-photon upconversion process can be performed with a cheap 980 nm CW laser at a low power density (10 to 50 W/cm^2) which will likely not cause phototoxicity.[50] Furthermore, the excitation wavelength minimizes autofluorescence coupled with the fact that it will get scattered less by tissues. The main reason to excite at 980 nm is the fact that the sensitizer ion Yb^{3+} can be excited. Furthermore the excitation wavelength also lies in the region where the biological tissue is most transparent. Depending on the codopant we can obtain a variety of emission from UV to NIR. In this thesis Yb^{3+} ions will be codoped with Er^{3+} or Ho^{3+} or Tm^{3+} ions.[51] If Er^{3+} or Ho^{3+} ions are codoped with Yb^{3+}, a green and a red emission are obtained from upconversion, whereas with Tm^{3+} ion as a codopant a blue and an 800 nm emission are observed.[52]

The 800 nm emission from Tm^{3+} ions is useful for the fact that this also lie in the near-infrared region where the tissue is transparent. Doping Tm^{3+} with Yb^{3+} ions will make sure that the excitation and emission wavelengths will lie in the region where tissues and cells are most transparent. Moreover, at these wavelengths autofluorescence from tissues and cells are minimal. The aforementioned lanthanide ions will be doped in two matrices: 1) LaF_3; 2) $NaYF_4$. These are low-phonon energy nanocrystals matrices (LaF_3-300 cm^{-1} and $NaYF_4$-550 cm^{-1}). A low-phonon energy (< 600 cm^{-1}) is necessary because it will not quench the emission from the lanthanides to a large extent when compared to high

phonon energy matrices like oxides, and silicates. The nanocrystals can be synthesized by two general methods: 1) Aqueous; 2) Organic.

Aqueous synthesis

Our group was the first to develop a synthetic procedure to make LaF_3 nanocrystals in aqueous media.[53] Nanocrystals synthesized from this technique as such do not disperse in solvents. They need a stabilizing ligand to disperse them in solvents. The ligand coordinates onto the surface of the nanocrystals thereby making the nanocrystals colloidally stable. In this aqueous synthesis, citrate molecules are used as ligands. These nanocrystals were dispersible in water for several months with no precipitation. The size of the nanocrystals was generally around 5 to 7 nm. This synthesis was basically developed so that these particles can be modified with a silica shell which is a process similar to the Stöber process.[54] The reason being that silica is a non-toxic material and furthermore it could be applied in a variety of applications like integrated optics, planar waveguides, upconversion lasers, and fiber amplifiers and bioimaging.[55] The synthesis was done at a relatively low temperature of 75 ^{o}C in water with citric acid, lanthanide nitrate salts and sodium fluoride. Ammonium hydroxide was employed to deprotonate the citric acid. The reaction was normally carried out for 1 hour followed by precipitating the nanocrystals in methanol. The nanocrystals were dried in air and stored as a dry powder.

The silica modification was done using tetraethyl orthosilicate (TEOS) as the silica source with an acid catalyst to make silica sol-gel with nanocrystals in it. This process is robust and the optical properties of different lanthanide ions were studied in detail by doping them in LaF_3 nanocrystals.[55] Another aqueous method to synthesize water-

dispersible lanthanide-doped nanocrystals. In this polyol synthesis, diethylene glycol, glycol, or glycerol is used both as the solvent and as the coordinating ligand. This reaction is normally carried out at higher temperature of 140 to 160 ^{o}C for long hours to improve the crystallinity of the nanocrystals.[56-58] A similar process is to use water as the solvent with a coordinating ligand like citric acid or similar small molecule with the reaction being carried out in an autoclave at elevated pressures. This also results in nanocrystals of 15 to 20 nm in size with excellent water dispersibility.[59-62] The main drawback with all the above processes is that it is hard to get uniform nanocrystals (<5% polydispersity) and high crystallinity. This can be solved by synthesizing the nanocrystals in an organic medium at high temperatures.

Organic synthesis

This involves high temperature reactions with a high boiling solvent like octadecene with oleic acid or oleyl amine as the coordinating ligand. Organic synthesis is generally used for preparing tetrafluoride matrices like $NaYF_4$, $NaGdF_4$, $LiYF_4$, etc. Furthermore the crystallinity obtained from this kind of synthesis is high which results in better optical properties than the nanocrystals synthesized through an aqueous synthesis. There are two types of synthesis: 1) thermolysis[63-68] 2) coprecipitation.[69-70] In thermolysis the precursors are separately prepared by reacting the respective rare-earth oxide with trifluoroacetic acid as the fluoride source. The precursors were mixed with octadecene, sodium trifluoroacetate (sodium source), and oleic acid or oleyl amine and heated to 300 ^{o}C and maintained at that temperature for 1 to 2 hours. In some cases the temperature was kept at 330 ^{o}C and the reaction time was about 30 minutes to 2 hours. At such high temperatures,

the lanthanide and sodium precursors decompose to form the nanocrystals. These nanocrystals are precipitated using ethanol or methanol followed by dispersing them in various apolar organic solvents.

Coprecipitation involves the formation of the oleate complex of the lanthanide salts (acetate or chlorides) at 120 to 140 ^{o}C, followed by the addition of a sodium and a fluoride source at a lower temperature of 30 to 50 ^{o}C. The reaction mixture is stirred for 30 to 40 minutes and subsequently heated to 300 - 330 ^{o}C. In this case as well, oleic acid and/or oleyl amine is used as the coordinating ligand. For thermolysis and coprecipitation syntheses, the use of oleic acid as the coordinating ligand resulted in a hexagonal crystal lattice while the oleyl amine resulted in a cubic crystal lattice. The hexagonal lattice has been found to be the best matrix for the upconversion process. The most common matrices used to dope lanthanides are $NaYF_4$[71], $NaGdF_4$[72], $NaLuF_4$[73], and $LiYF_4$.[74] The size of the nanocrystals can be varied from 7 to 35 nm depending on the ratio of the reactants, temperature, and the time of the reaction. This synthesis yields nanocrystals that exhibit superior optical properties than the ones obtained through aqueous synthesis. However, due to the hydrophobic nature of the nanocrystals and the surface ligands they do not disperse in water. This is solved by a surface modification step to make them dispersible in water and other aqueous media like buffers. The surface modified nanocrystals can then be used for bioimaging applications.

Surface modification

Surface modification step is performed with nanocrystals to make them suitable for bioimaging. There are three major surface modifications; 1) ligand exchange; 2) polymer

encapsulation; 3) silica coating (e.g. by microemulsion). The merits and demerits of these methods will be discussed in detail in chapter 3 and 5.

1.2 Quantum Dots

The other alternative proposed for bioimaging is the use of lead-based quantum dot (QD) nanocrystals as bioimaging agents. Quantum dots are different from their bulk semiconductor counterparts due to their unique bandgap structure at the nanoscopic level.[75] A semiconductor has a continuous energy bands due to the large number of molecular orbitals with overlapping energy.[76] However, at the molecular level they are present as discrete energy levels. Quantum dots bridge the gap between the molecular level and the bulk level. In the bulk semiconductor the energy band gap is fixed, however in case of QDs the band gap changes with respect to their size. The electronic excitations "feel" the presence of boundaries of the nanocrystals (generally less than 10 nm). Due to this, they respond to changes in the particle size by changing their bandgap energy.[77] This can be seen in Figure 1.9. This is due to quantum confinement at such sizes. Quantum confinement is observed when the size of nanocrystals is smaller than the exciton Bohr radius. Exciton Bohr radius is the distance between the electron in the conduction band and the hole it had created when it left the valence band.[78-81] The quantum confinement of quantum dots is generally explained using the particle in a box situation. Furthermore, the quantum dots are zero dimensional structures due to which quantum confinement occurs in all three dimensions. The exciton Bohr radii for CdSe and PbSe quantum dots are 5.6 nm and 46 nm, respectively.[82] In case of quantum wells and quantum rods the confinement occurs in 1 and 2, dimensions respectively.[77]

As the size of the nanocrystals decreases the band gap energy increases shifting the absorption spectra peak towards the blue. The best example for this is the CdSe quantum dots where a shift in the absorption spectra towards the blue, as the size decreases (Figure 1.10).[83] In this thesis, lead-based quantum dots are studied so that they could be employed as a bioimaging agent. Lead-based quantum dots emit in the near-infrared region ranging from 700 to 3000 nm which is due to their large exciton Bohr radius.[82] There are three major methods to synthesize the quantum dots: 1) preparation in glass hosts; 2) self-assembled quantum dots 3) colloidal synthesis of quantum dots. In this thesis the lead-based quantum dots studied were synthesized by the colloidal method. This is explained in detail in the next section.

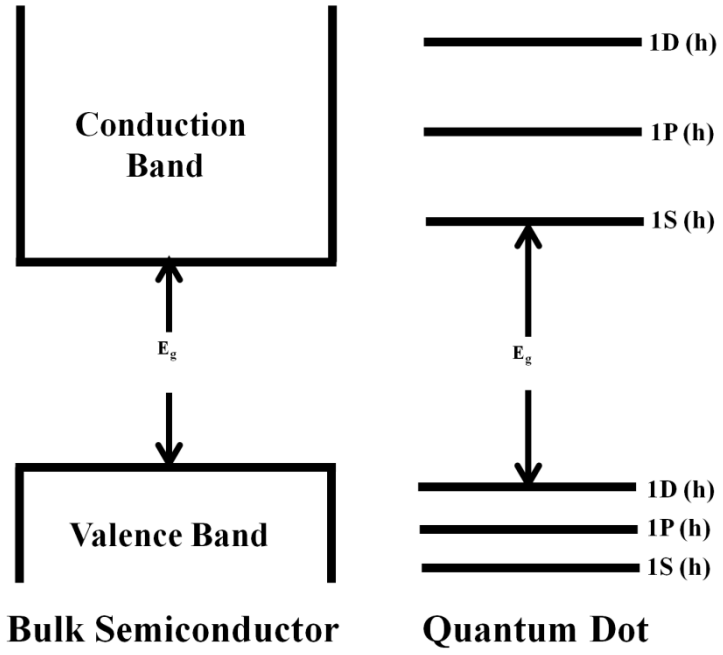

Figure 1.9. Band gap energy diagram for bulk semiconductor and a quantum dot.

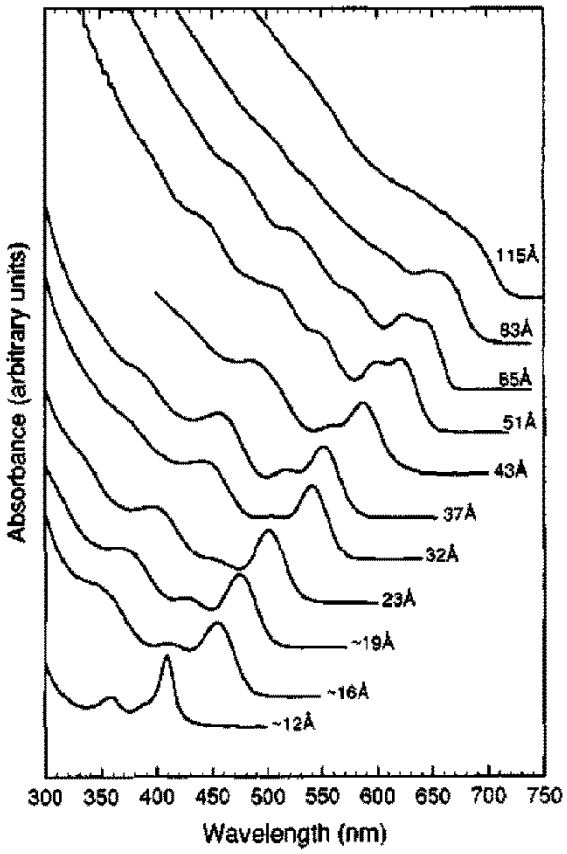

Figure 1.10. The shift in the absorption spectra towards the red is observed as the size of the CdSe quantum dot increases.[83] Reprinted with permission from American Chemical Society.

1.2.1 Synthesis of quantum dots in glass hosts

The earliest method to synthesize quantum dots of different sizes is by embedding them in glass hosts. The method involves doping molten glass with semiconductors followed by a rapid cooling and secondary heating method (400 to 700 ^{o}C).[84-85] This causes the semiconductors to crystallize inside the glass forming the quantum dots. The time and temperature of the secondary heating decides the size of the quantum dot. The big disadvantage is that the glass host is not processible once the quantum dots are

synthesized which makes this method unattractive for device applications and bioimaging.

1.2.2 Synthesis of self-assembled quantum dots

Molecular Beam Epitaxy (MBE) and Metal Organic Chemical Vapor Deposition (MOVCD) are the two major methods to grow quantum dots in a self-assembled fashion.[86-87] The low band gap semiconductors are generally embedded in a large band gap semiconductor matrix. The quantum dots are formed because there is a lattice mismatch between the substrate (large band gap semiconductor) and the quantum dots (small band gap semiconductor). Due to this the small band gap semiconductors when they are deposited on the substrate form islands instead of growing smoothly over the substrate. This kind of growth is explained by the Stranski-Krasnatov instability theory. Fabrication and the control over the size and the position of the quantum dots is challenging and to achieve them it's expensive.

1.2.3 Synthesis of colloidal quantum dots

The colloidal synthesis is completely different from the above two methods. This synthesis results in a semiconductor quantum dot core with their surface protected by a ligand.[88-90] Ligand molecules passivate the surface of the quantum dots thereby protecting the emission from quenching effects by solvents, surface defects, and dangling bonds.[91-93] The ligands also help in controlling the growth, shape, and the size of the nanocrystals. The colloidal quantum dots are generally synthesized through a hot injection method. In this method the metal complexes with the chosen ligands in presence of a solvent are pre-

made, followed by the rapid injection of the selenium or sulfur source.[77] The big advantage over the other two methods is that the size, shape, and crystallinity can easily be controlled with the reaction time, temperature, molar concentrations of the reactants, and the source of precursor elements. Murray *et al.* were the first to synthesize high quality cadmium selenide quantum dot nanocrystals through the hot injection method.[94] Subsequently, the hot injection method was employed for synthesizing a variety of seminconductor nanocrystals like, CdS, ZnSe, PbS, PbSe, HgSe, PbTe, CdTe, etc. Most of these nanocrystals need a good surface passivation to avoid the emission being quenched by surface defects, solvent, and to a little extent by ligands. Furthermore, on exposure to ambient atmosphere these quantum dots starts oxidizing from the surface eventually losing their luminescence efficiency.

In order to solve this, a protective shell is grown over the nanocrystals which improve their stability.[88,95] The most common method to grow a protective shell layer is the Successive Ion Layer Adsorption and Reaction (SILAR) technique.[96] The details will not be presented in this thesis. There is a recent method to grow a shell material through a process called cation exchange. As the name suggests, the cations of the quantum dot are exchanged with another cation (taken in large excess) while the anionic matrix is maintained. The process can be controlled with the help of temperature of the process, the ratio between the excess cations, and the type of quantum dots. The cation exchange process in nanocrystals was first observed and explained by Alivisatos and coworkers in 2004.[97] They showed that CdSe can completely be converted to AgSe and back to CdSe through this process. The crystal shape remains the same before and after the process

showing that this happens through cation exchange. However, until 2008, this methodology was not employed to grow core/shell structures. Hollingsworth and coworkers employed this technique to grow a shell of CdSe over PbSe.[98-99] The reason they chose this process is because of the fact that the SILAR technique could not be used for growing any kind of protective shell over lead-based quantum dots. On the other hand, the cation exchange process is efficient, and the thickness of the shell can easily be controlled by the temperature of the reaction. Due to the cation exchange process the overall size of the quantum dots do not change. The formation of a protective shell through this process results in the reduction of the size of the core of the QDs. This results in a blue shift in the emission after the exchange when compared to the original emission.

The cation exchange process is faster for smaller quantum dots (2 nm) when compared to the large ones (6 nm).[99] This could be due to the large surface to volume ratio for the smaller QDs and the large number of surface defects generally associated with smaller QDs. The protective shell through the cation exchange process improves the photostability and also increases the luminescence efficiency of the lead-quantum dots. Furthermore to provide evidence for the core/shell structure obtained after the cation exchange process, our group employed HAADF, EELS mapping, SANS, and energy-dependent XPS. All the above techniques help in proving that a core/shell structure is indeed formed after the cation exchange process.[99] Lead-based quantum dots have a band gap energy which results in the emission lying in the near-infrared region. They can emit from 700 to 3000 nm depending on the size of the nanocrystals. CdSe has been shown to

have a efficient two-photon absorption process due to their high two-photon absorption crosssection area (47000 GM units).[100] Researchers have theoretically predicted that all quantum dots would have a high two-photon absorption crosssection area. As lead-based quantum dots can be tuned to emit in the 700 to 1200 nm region which is the most transparent region of the biological tissue, they can be exploited for bioimaging. Furthermore the two-photon absorption process could potentially be used for imaging. However, there is a big challenge in employing the lead-based quantum dots as bioimaging agents. This is because there is no surface modification strategy to disperse the hydrophobic quantum dots in water and make them stable under physiological conditions. There are four surface modification strategies discussed in chapter six to obtain stable dispersion in physiological conditions.

1.3 Outline for the thesis

The last two sections give an overall idea about the two types of nanocrystals which have been studied in this thesis. Chapter 2 will discuss the synthesis and surface modification of LaF_3 nanocrystals with Yb^{3+} and Ho^{3+} as the dopants. These nanocrystals exhibit varied ratios of red to green emissions from the upconversion process depending on the type of silica they are embedded in. The effective control over the ratio of the red to green emissions is explained with the help of X-ray diffraction, low temperature measurements (77 K), and Fourier Transform Infra-Red spectroscopy (FTIR). Chapter 3 explores the advantage of using $NaYF_4$ as the successor matrix to LaF_3 to dope lanthanide elements. The first half of this chapter gives a detailed account on the synthesis and characterization of the nanocrystals. The second half explains two surface

modification techniques (intercalation and crosslinking) using two amphiphilic polymers. The pros and cons of both the surface modification strategies to disperse the nanocrystals in buffers, different pH values, and serum-supplemented growth media are demonstrated. Chapter 4 deals with the application of $NaYF_4$ nanocrystals doped with Yb^{3+} and Er^{3+} or Tm^{3+} ions as imaging agents in *in-vivo* and *in-vitro* experiments. A critical evaluation of these nanocrystals as imaging agents has been done by using two-photon upconversion laser scanning microscopy (TPULSM) and two-photon upconversion wide field microscopy.

In chapter 5, energy-dependent X-ray photoelectron spectroscopy (XPS) is used to probe the structural architecture of the doped and undoped $NaYF_4$ nanocrystals. Furthermore, a preliminary study on lanthanides using resonant XPS is reported. The results in this chapter could possibly help in making nanocrystals which are much more efficient than the current ones reported in literature. The synthesis and surface modification of lead-based quantum dots are explored in chapter 6. Four different surface modification strategies are studied to examine which one would be the best for dispersing lead-based quantum dots in various aqueous media for biological applications. The obstacles faced in all four methods are also elucidated. The last chapter will explore possible further opportunities to extend the work done in this thesis and conclude on what has been achieved in this thesis.

Chapter 2. Effective Control of the Ratio of Red to Green Emission in Upconverting LaF_3 Nanocrystals Co-doped with Yb^{3+} and Ho^{3+} Ions Embedded in a Silica Matrix

2.1 Introduction

Upconversion is a process that converts two or more lower-energy photons into one higher-energy photon. Most of the upconversion processes in-case of lanthanide ions are stepwise two-photon processes.[5,51,102] However there are some exceptions like photon avalanche processes[51,103] and the stepwise three-photon[65,104-108] process for upconverted blue light from Tm^{3+} ions.[109] One such interesting photon avalanche type of process is the hetero-LEET mechanism which has been reported by our group.[49] Upconversion through lanthanide nanocrystals has been studied extensively in various matrices especially with Yb^{3+} and Er^{3+} ions.[33,37,57,67,69,110-115] Several matrices like LaF_3, $NaYF_4$, Y_2O_3, KYF_4, YVO_4, nanocrystals co-doped with Yb^{3+} and Er^{3+} ions have been synthesized and studied in detail. Effort has gone into understanding and synthesizing new nanocrystals for doping with Yb^{3+} and Er^{3+}. These nanocrystals are regarded as interesting materials for application in biolabels, LEDs, security labels, monitoring drug delivery etc.[67,105,116-123] Generally, Yb^{3+} and Er^{3+} co-doped systems give a bright green emission along with a weak red emission. On the other hand, Zhao *et al.*[124] reported enhanced red emission in

$NaYF_4$ nanocrystals co-doped with Yb^{3+} and Er^{3+} ions. They observed that the presence of citrate ligands, and OH groups from the hydrothermal synthesis result in the quenching of green emission and enhancement of red emission. In addition to this, Li *et al.*[125] argue that with high Yb^{3+} doping (> 25%) and calcination of Gd_2O_3 at lower temperatures result in enhanced red emission. Even though Yb^{3+} and Ho^{3+} co-doped nanocrystals are similar to Yb^{3+} and Er^{3+} systems in terms of upconversion properties, only a handful of papers deal with these nanomaterials.[38,126-128] These papers have studied the upconversion properties by changing the concentration of Yb^{3+} and Ho^{3+} ions in the nanocrystals. Typically, the upconversion through Yb^{3+} and Ho^{3+} co-doped systems result in an intense green emission accompanied by a weak red emission.

However, there are only a few reports on enhanced red emission from Yb^{3+} and Ho^{3+} co-doped upconversion process. The enhanced red emission observed by Yi *et al.*[129] in LaF_3 nanocrystals co-doped with Yb^{3+} and Ho^{3+} ions has been attributed to the presence of organic ligands stabilizing the particles that quench the green emission. Lisiecki *et al.*[130] have reported that high doping levels of Yb^{3+} ions and high phonon energy of YVO_4 nanocrystals facilitate the enhancement of red emission. Our group has also reported that when LaF_3 nanocrystals were co-doped with high levels of Yb^{3+} and Ho^{3+} ions and then coated with silica they got converted to lanthanum silicate which has phonon energy of 1200 cm^{-1}. So the lanthanum silicate matrix due to its higher phonon energy than LaF_3, quenches the $^5I_6$ level populating the $^5I_7$ level of Ho^{3+} ions.[131] This results in more and more photons reaching the $^5F_5$ level from the $^5I_7$ level which subsequently emits red light. This results in an increased red emission when compared to green emission. However,

there are no reports on how to control the ratio of visible emissions from upconversion. Controlling the emission in upconversion process will help in tuning the color of the light which will be useful for constructing e.g. an upconversion laser with near-infrared excitation. Furthermore a strong red emission from the nanocrystals will get less scattered by tissues and cells than green emission.

In this chapter the effective control of red to green ratio is shown in an upconversion process involving Yb^{3+} and Ho^{3+} ions co-doped in LaF_3 nanocrystals that are embedded in a silica matrix. LaF_3 was chosen as the matrix to be co-doped with Yb^{3+} and Ho^{3+} due to its low phonon energy (300 cm^{-1}).[132] There are two reasons for embedding lanthanide nanocrystals in a silica matrix using sol-gel technique. The first reason is that the as-synthesized nanocrystals do not show any emission due to upconversion. They have to be baked to remove OH groups and organic ligands which would quench all the energy levels involved in the upconversion process resulting in no emission. Baking would convert the nanocrystals into the bulk form of the material and render them not suitable for further modifications. To overcome this problem the nanocrystals were embedded in a silica matrix using sol-gel technique which makes the material a potential candidate for applications like integrated optics, planar waveguides, upconversion lasers, and fiber amplifiers.[103,133-135] The second reason is that silica also prevents the nanocrystals from aggregation and also improves the luminescent properties of the nanocrystals when compared to the doping of lanthanide ions directly in silica.[55] In addition silica is a non-toxic material which could make these nanocrystals suitable for bioimaging. An increase in the red emission is normally attributed to the high amount of Yb^{3+} doping in the

sample which results in increased energy transfer from Yb^{3+} ions to Ho^{3+} ions as well as the energy back transfer from $^5S_2$ level of Ho^{3+} ions to $^2F_{5/2}$ of Yb^{3+} resulting in quenching of green emission. In this chapter it is shown that high Yb^{3+} dopant concentrations in nanocrystals is not responsible for the control of red to green ratio, and provide concrete evidence for the fact that the ratio is controlled by the amount of cristobalite (crystalline silica) and amorphous silica present in the sample after the baking of the sol-gel.

2.2 Results and Discussion

2.2.1 Size and EDS Measurements

The LaF_3 nanocrystals co-doped with Yb^{3+} and Ho^{3+} ions were synthesized using methods similar to previously published protocols[53,55,123,136] and their size was found to be 5 to 7 nm from XRD measurements using the Scherrer equation. The doping level in nanocrystals is often expected to be the same as added in the reaction mixture, but this is not necessarily the case. Energy dispersive X-ray spectroscopy (EDS) results show that nominal doping levels of 50 ,40, 30, and 10, atom percent Yb^{3+} ions in the reaction resulted in 22, 17, 12, 4 atom percent, respectively, in the LaF_3 nanocrystals. A reaction mixture with 5 atom percent of Ho^{3+} ions resulted in 2 atom percent in the final product. A representative spectrum is shown in Figure A.1.

2.2.2 Influence of Aging Drying and Baking on Luminescent Properties

The ratio of red to green (Fig. 1A) could be controlled from 1:2.3 to 23:1 by changing the parameters like aging time, drying time, and baking pattern of the silica sol-gel. All three

parameters had to be changed in-order to get the desired ratio, so the overall effect is highly convoluted. Sample 1 (Table 2) which was aged for 2 days and dried in rotary evaporator for 45 minutes and baked at 800 ^{o}C gave a strong green emission when compared to red emission as shown in (Figure 2.1) which have a ratio of red to green of 1:2.3. The green (540 nm), red (654 nm) and 750 nm emissions correspond to $^{5}S_{2}$ to $^{5}I_{8}$, $^{5}F_{5}$ to $^{5}I_{8}$, and $^{5}S_{2}$ to $^{5}I_{7}$ transitions of Ho^{3+}, respectively (Figure 2.2 & Figure 2.3). When Ho^{3+} was excited at 450 nm we observed a green and 750 nm emission along with a weak red emission (Figure A.2 (A)). This suggests that green does not feed the red emission. To confirm whether the $^{5}S_{2}$ energy level is responsible for the 750 nm emission the sample was excited at 540 nm for which indeed a peak at 750 nm was observed (Figure A.2 (B)). The absence of red emission is further confirmation that the $^{5}S_{2}$ level is responsible for 750 nm emission. With the help of the aforementioned evidence and the report from Boyer *et al.*[38] a probable mechanism is proposed (Figure 2.3). A strong green emission in comparison with a weak red emission was observed for a similar sample like sample 1 when it was aged for 15 days and dried for 45 minutes in a rotary evaporator. When a sample was aged for 2 days and dried in a rotary evaporator for 5 hours the ratio of red to green was still 2.3 to 1.

As the aging time was varied from 2 to 15 days combined with a gradual increase in drying time of the sol, a progressive increase in the ratio of red to green was seen (Figure 2.1). The maximum ratio of 23:1 was obtained for sample 6 which was aged for 15 days and dried for 11 hours before annealing. This implied that drying plays a vital role in controlling the ratio. An interesting factor to note is that all ratios were observed for the

same composition i.e. $La_{0.76}Yb_{0.22}Ho_{0.02}F_3$ nanocrystals embedded in a silica matrix. Baking is also a decisive factor in observing enhanced red emission. The samples 1 to 4 were baked at 800 ^oC for 12 hours whereas samples 5 and 6 were baked at 300 and 500 ^oC before baking at 800 ^oC for 12 hours. For samples 5 and 6 baking at 300 and 500 ^oC was necessary along with the increase in aging and drying time to see an enhanced red emission. The above results provide strong evidence that all the three parameters (i.e. aging, drying, and baking) play an important role in controlling the ratio of red to green. This trend of high red to green ratio was seen for other doping levels of Yb^{3+} ions. The red to green ratio for 17% Yb^{3+} co-doped nanocrystals embedded in a silica matrix obtained was 42:1 (Figure 2.4 A). In case of 12 and 4 atom percent doping with Yb^{3+} ions the red to green ratio was 18:1 and 23:1 respectively (Figure 2.4 B&C). The varied red to green ratios was also observed for 12 mole percent Yb^{3+} concentrations (Figure A.3). As expected, with an increase in the amount of Yb^{3+} concentrations in the nanocrystals, the amount of red and green also increased which can be seen from Figure A.4.

The power dependence curves (Figure A.5) show that both green and red emissions are two-photon processes, and the ratio of red to green at various power densities remains the same. The slope over the first seven points is between 1.9 and 2.0, with a slight decrease of the slope to 1.6 to 1.7 at higher power densities because of saturation effects. The ratio of green to 750 nm emission changes for samples 1 to 6, which can be attributed to the change in the branching ratios of $^5S_2$ to $^5I_8$ and $^5I_7$ due to the subtle difference in the coordination sphere of the surface Ho^{3+} ions because of differences in amorphous silica

and cristobalite. There is precedent for this effect based on Eu^{3+} doped LaF_3 nanocrystals embedded in the silica matrix.[55]

Table 1. Change in Red (R) to Green (G) ratio as a function of aging and drying time of $La_{0.76}Yb_{0.22}Ho_{0.02}F_3$ embedded in a silica matrix*.

Sample	Aging time (days)	Drying time at 78 °C	Drying time at 92 °C	Baking 300 °C	Baking 400 °C	Baking 500 °C	Baking 800 °C	Red :Green ratio
1	2	45 min	0 min	0 min	30 min	0	12 hours	1:2.3
2	3	2 hours	0 min	0 min	30 min	0	12 hours	1:1.5
3	4	2 hrs 30 min	0 min	0 min	30 min	0	12 hours	1:1
4	4	2 hrs	2 hrs	0 min	30 min	0	12 hours	3.2:1
5	6	2 hrs	4 hrs	4 hrs	0 min	4 hrs	12 hours	6.3:1
6	15	2 hrs	11 hrs	8 hrs	0 min	8 hrs	12 hours	23:1

*All ramping procedures for samples are the same as detailed in the experimental part.

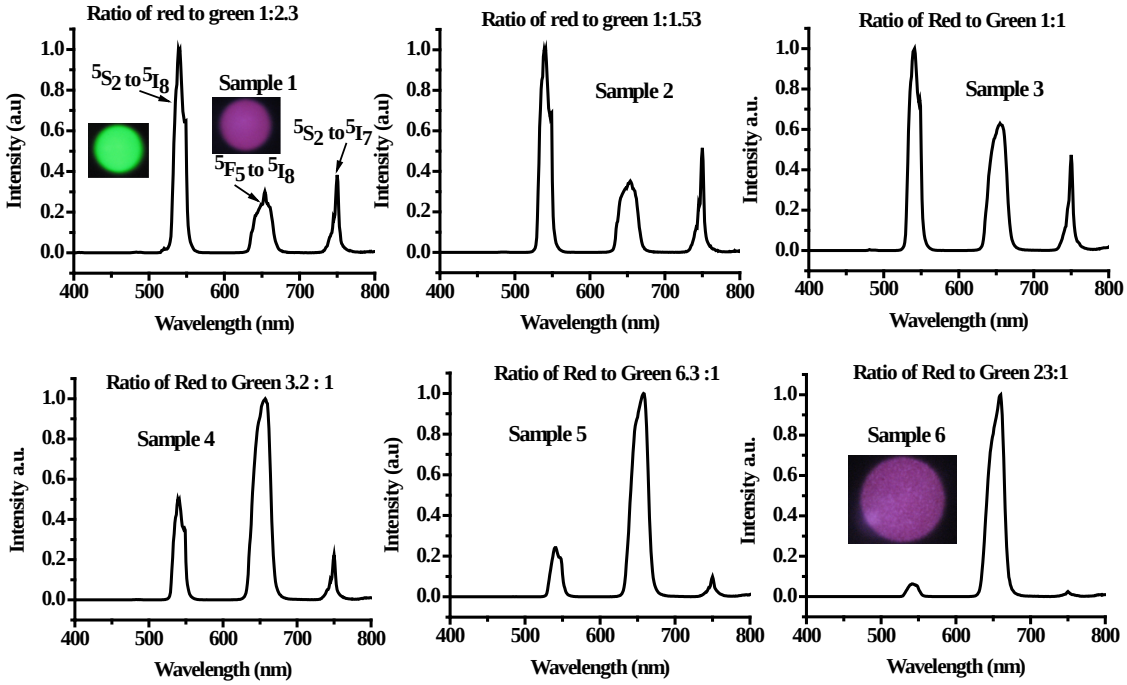

Figure 2.1. Different red to green ratio seen in upconversion luminescence from samples of the same composition ($La_{0.76}Yb_{0.22}Ho_{0.02}F_3$ embedded in a silica matrix). Insets - red light pictures in sample 1 and 6 were photographed using a 590 nm filter and no filter was used for green light in sample 1.

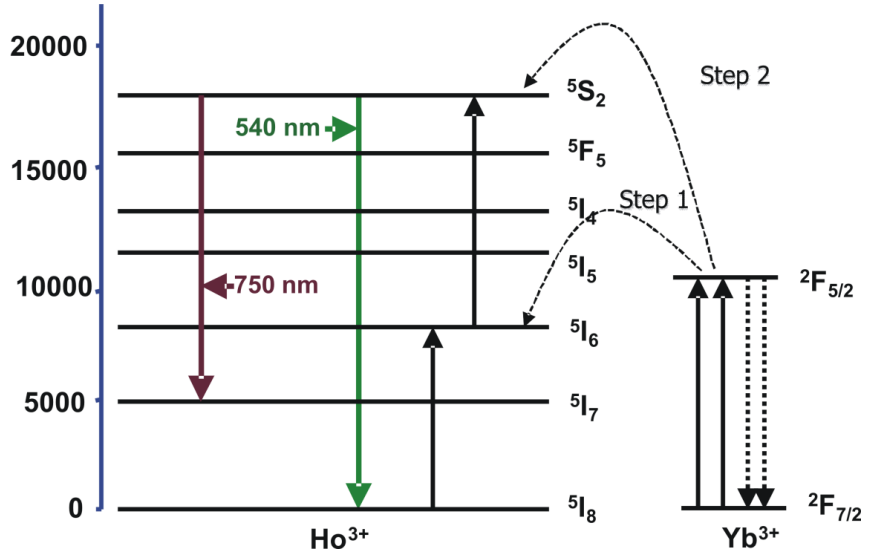

Figure 2.2. Probable mechanism for green emission (peak at 540 nm) and 750 nm emission.

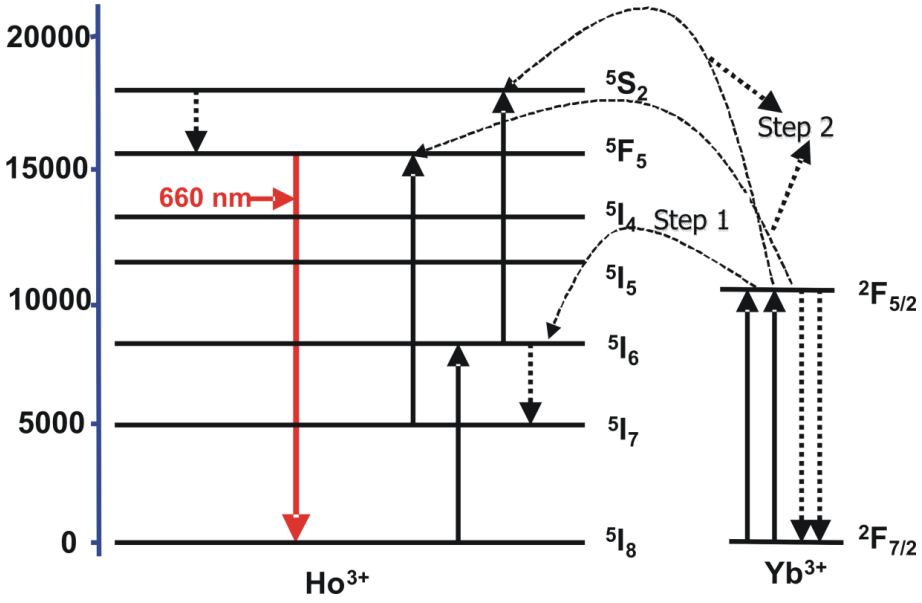

Figure 2.3. Probable mechanism for red emission (peak at 654 nm).

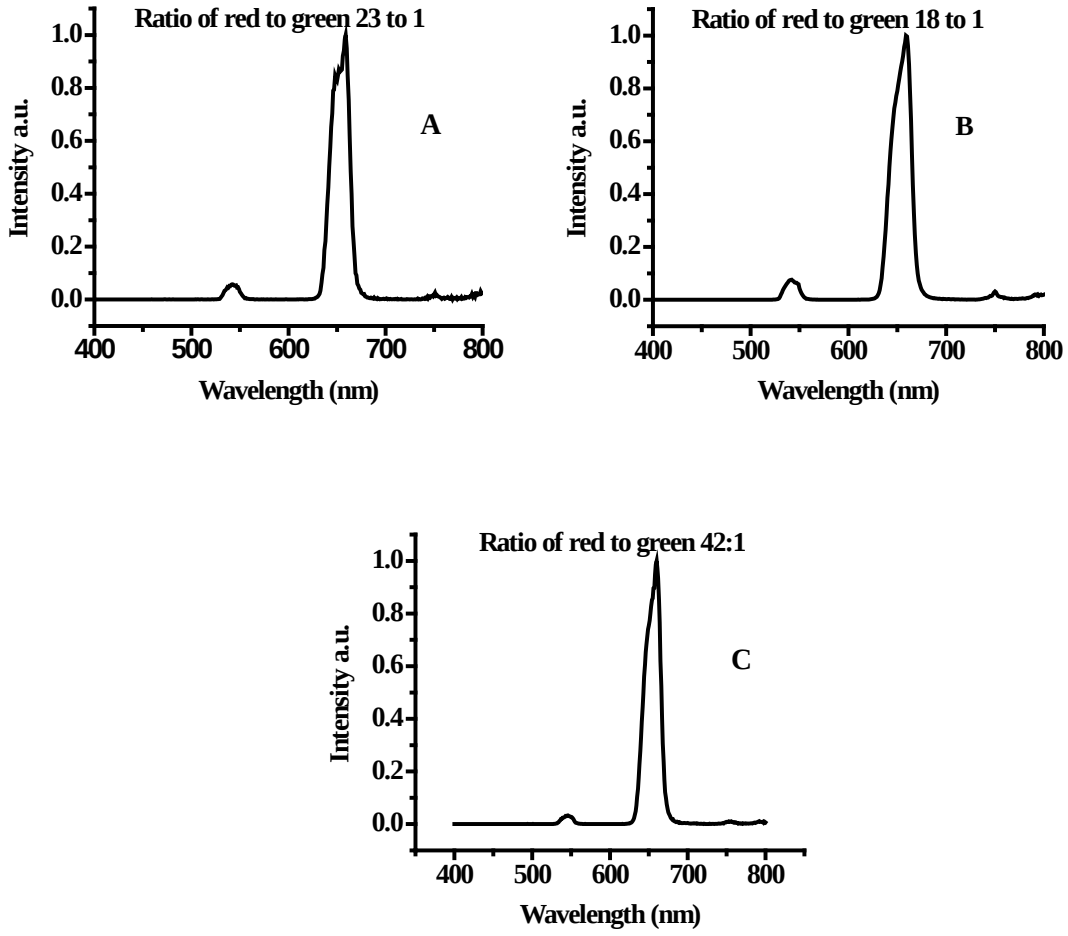

Figure 2.4. Different red to green ratio seen in upconversion luminescence from samples of the different composition (A) $La_{0.94}Yb_{0.04}Ho_{0.02}F_3$, (B) $La_{0.86}Yb_{0.12}Ho_{0.02}F_3$ (c) $La_{0.81}b_{0.17}Ho_{0.02}F_3$. All samples were embedded in a silica matrix.

2.2.3 XRD measurements and Etching with HF

Some of our previous reports initially suggested that the high red to green ratio obtained might be due to the fact that LaF_3 could have be converted to lanthanum silicate[55] which has a higher phonon energy than LaF_3. However, XRD results do not suggest the

presence of lanthanum silicate for samples showing high red to green ratio. Instead the XRD results indicated that sample 6 (Figure 2.5) had amorphous silica and no apparent traces of any other compound. This can be attributed to the fact that the presence of large amounts of amorphous silica masks the signal from LaF_3 and potentially others compounds. This is because the amount of LaF_3 in the sol is around ~7.5 wt% which is not very high when compared to that of amorphous silica (92.5 %). In order to find out whether LaF_3 was present along with amorphous silica, the sample was completely etched with 2 % HF. XRD results show that the compound had LaF_3 (Figure A.6) and not lanthanum silicate.[55] The reason why lanthanum silicate was not formed is because of the fact that the sol was dried in a rotary evaporator for a long time (see Table 1) which would have converted $Si(OH)_4$ in the sol to SiO_2. For lanthanum silicate to have formed, $Si(OH)_4$ has to react with LaF_3 at elevated temperatures to remove the fluoride as HF.

The formation of amorphous silica can be attributed to the drying process in vacuum in a rotary evaporator for long hours and annealing at 500 and 800 ^oC for several hours. Moreover the XRD results for sample 1 in Figure 2.6 (low red to green ratio) show a large amount of cristobalite along with amorphous silica and LaF_3. If the difference in XRD is just the amount of amorphous silica between sample 6 and 1, the plausible explanation for getting enhanced red to green ratio is that the phonon energy of amorphous silica has to be higher than that of cristobalite. One way to confirm that amorphous silica is responsible for the enhanced red to green ratio sample 6 was partially etched with 2 % HF. The partially etched sample still gave an enhanced red emission with reduction in ratio of red to green from 23:1 to 12:1 (Figure A.7). XRD results show

that the partially etched samples had LaF_3, a large hump for amorphous silica and a sharp peak for cristobalite (Figure 2.7). Amorphous silica etches faster when compared to crystalline silica[137] which corroborates our results where cristobalite and LaF_3 are observed after partial etching. The reason why cristobalite was not observed before etching might be due to the fact that the presence of large amounts of amorphous silica has masked the signal from cristobalite. The reduction in the red to green ratio after partial etching and a diminished red to green ratio for samples with large amounts of cristobalite imply that the ratio of cristobalite to amorphous silica is decisive for the ratio of red to green. If cristobalite is present in large amounts when compared to amorphous silica a decrease in the red to green ratio is observed whereas for amorphous silica a big augmentation in the red to green ratio is observed. This is further substantiated by the fact that sample 1 had large amounts of cristobalite along with LaF_3 and amorphous silica whereas sample D ($La_{0.86}Yb_{0.12}Ho_{0.02}F_3$, Figure A.8) had large amounts of amorphous silica along with cristobalite and LaF_3.

Excess amorphous silica can be seen from XRD which shows a broader peak for silica in sample D when compared to sample 1 referring to large amounts of amorphous silica. When sample 6 was completely etched a strong green was observed when compared to a weak red emission resulting in a much diminished red to green ratio of 1:2.3. This provides direct evidence that amorphous silica is responsible for enhancing the red to green ratio. Sample 1 was also completely etched to remove cristobalite to see whether there is a further decrease in the ratio of red to green from 1:2.3. The etched sample showed the same red to green ratio as before and XRD results show that LaF_3 was present

which can be seen in Figure A.9. This might be due to the fact that the XRD shows the presence of small amounts of silica, still attached to the LaF_3 nanocrystals even after nearly complete etching, and the presence of water on the surface of the nanocrystals. Both quench the green emission probably apparently resulting in the same red to green ratio as seen before etching.

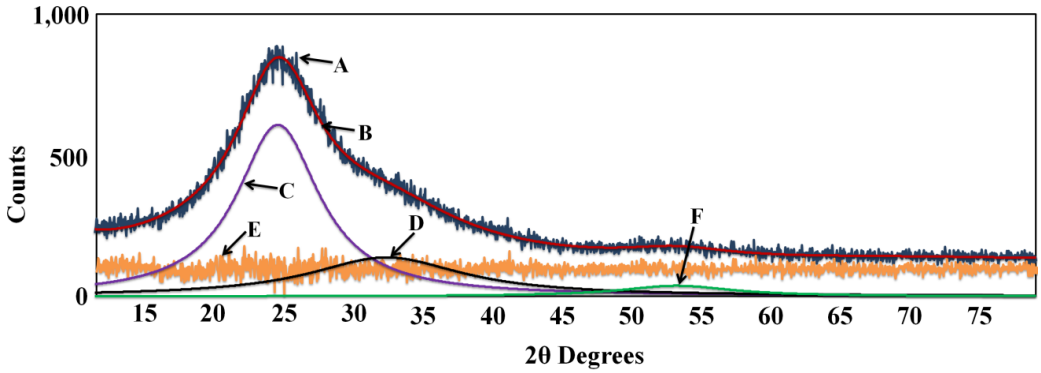

Figure 2.5. XRD pattern of baked $La_{0.76}Yb_{0.22}Ho_{0.02}F_3$ nanoparticles embedded in a silica matrix (enhanced red emission); Ratio of red to green 23:1 A) Observed Pattern, B) Calculated Pattern, (C, D, F) From peaks fitted to amorphous silica, E) Residual Curve.

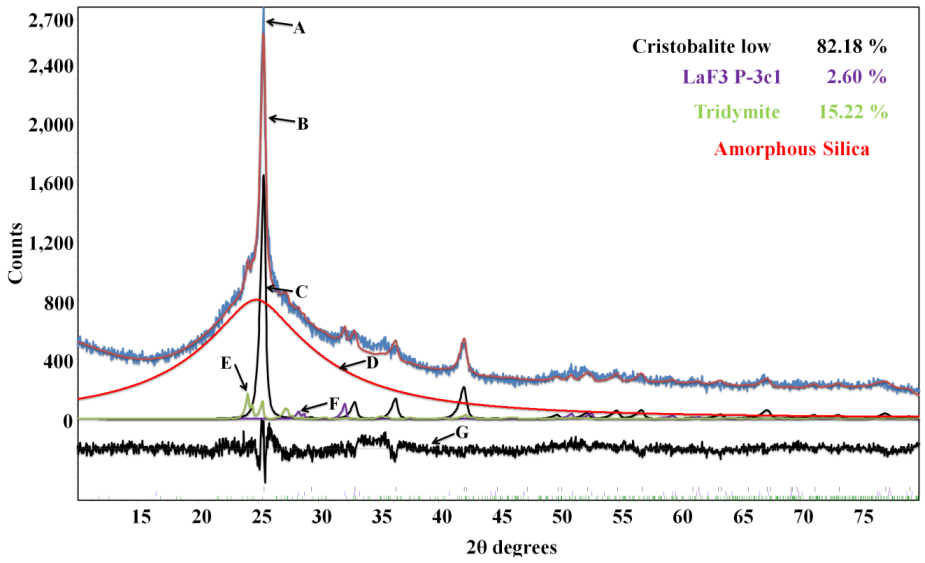

Figure 2.6. Rietveld refinement plot of baked $La_{0.76}Yb_{0.22}Ho_{0.02}F_3$ nanoparticles embedded in a silica matrix (enhanced green emission) ratio of red to green 1:2.3 sample. A) Observed Pattern, B) Calculated pattern, C) Cristobalite D) Amorphous Silica, E) Quartz low F) LaF_3 P-3c1, G) Residual curve. The weight percent does not include amorphous silica.

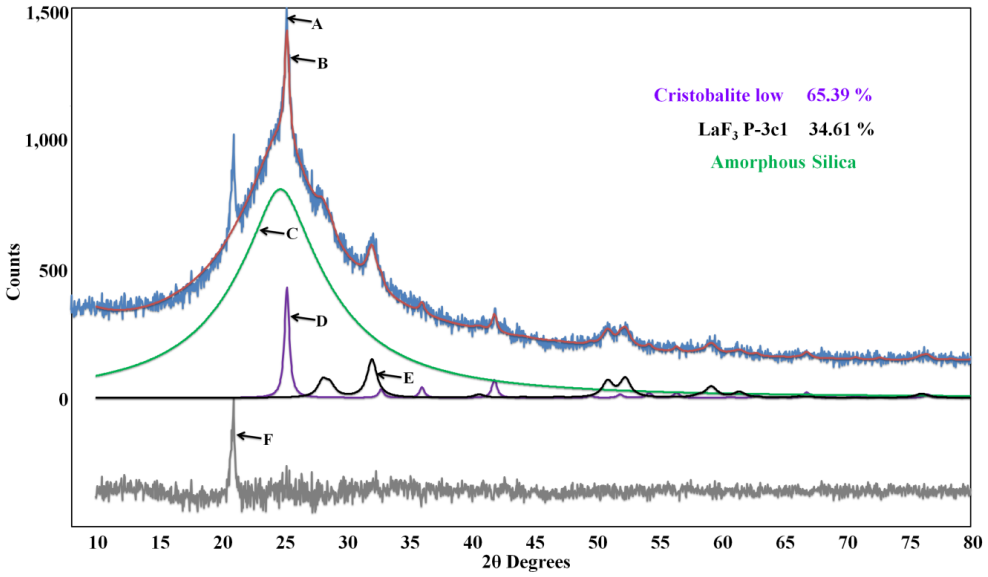

Figure 2.7. Rietveld refinement plot of partially etched $La_{0.76}Yb_{0.22}Ho_{0.02}F_3$ nanoparticles embedded in a silica matrix, the weight percent does not include amorphous silica A) Observed Pattern, B) Calculated Pattern, C) Amorphous Silica, D) Cristobalite, E) LaF_3 P-3c1, F) Residual peak. The weight percent does not include amorphous silica.

2.2.4 Low Temperature Upconversion Measurements at 77 K

Another way to substantiate that the differences in the phonon energy is responsible for the enhanced red emission, is to measure the upconversion spectrum at 77 K. The expected result at low temperatures was that, the red emission would diminish resulting in a significant change in the ratio of red to green would be observed. These measurements showed that the ratio of red to green for $La_{0.86}Yb_{0.12}Ho_{0.02}F_3$ nanocrystals embedded in a silica matrix indeed decreased from 18:1 to 5.8:1 as seen in Figure 2.8 A. When the low temperature measurements were carried out for the sample $La_{0.86}Yb_{0.12}Ho_{0.02}F_3$ (Figure 2.8 B) enhanced green emission was observed and the ratio changed from 1:2.3 to 1:9. This also corroborates the fact that the phonon energy at room temperature plays an important role in the amount of red which is observed and the control over the ratio of red to green. A slight shift in the peaks to higher wavelength, i.e. lower-energy, (Figure 2.8) is observed for the low temperature spectra, as expected based on the Boltzmann distribution.

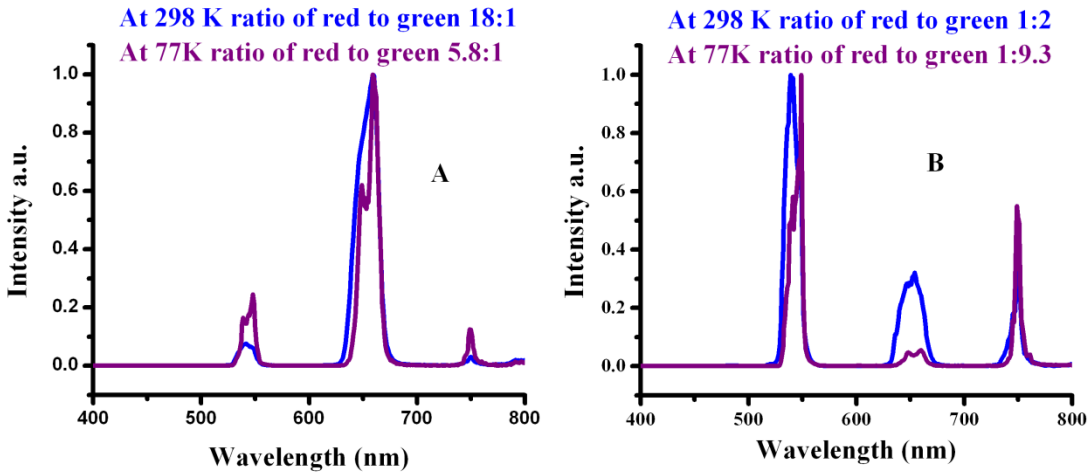

Figure 2.8. Upconversion spectra of $La_{0.86}Yb_{0.12}$ $Ho_{0.02}$ nanoparticles embedded in a silica matrix at 298 and 77 K, A) sample aged for 15 days; B) sample aged for 2 days.

2.2.5 Infra-Red (IR) Spectra

The third piece of evidence which supports this explanation was obtained for the IR spectra of the samples 1 and 6 which gave enhanced green and enhanced red respectively. Both samples show peaks at 1100 cm^{-1} corresponding to the Si-O-Si stretch. The sample giving enhanced red shows a broad peak at 1100 cm^{-1} when compared to the sample which shows a dominant green emission (Figure 2.9). This suggests that amorphous silica has a higher number of lower and higher-energy phonons when compared to cristobalite. Due to the broader phonon energy distribution of amorphous silica the difference in the energy levels of Ho^{3+} ions can more easily be matched with a number of higher and lower energy phonons. This makes the quenching process more efficient for amorphous silica than cristobalite.

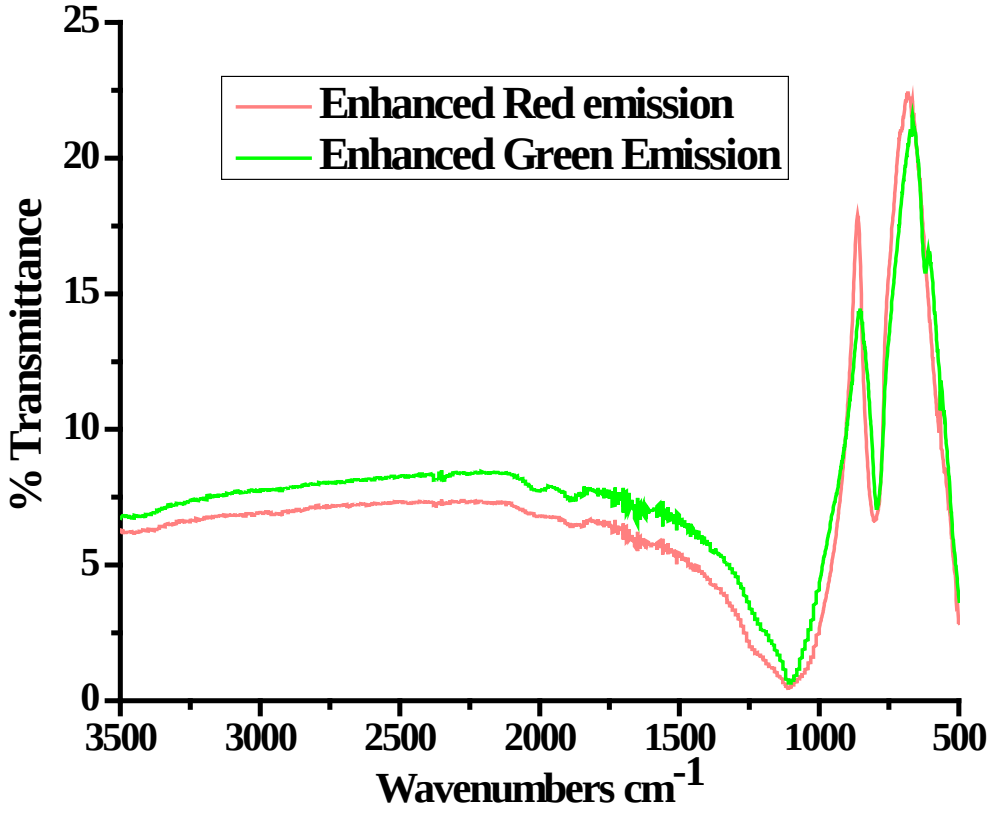

Figure 2.9. IR spectra for $La_{0.76}Yb_{0.22}Ho_{0.02}F_3$ nanoparticles embedded in a silica matrix (enhanced green emission and enhanced red emission) Enhanced green emission transmittance values were decreased by a factor of 1.5 in order to make an easy comparison with the enhanced red emission values.

2.2.6 Dispersibility in water

The baked LaF_3 nanocrystals embedded in a silica matrix did not disperse in water. The high temperature and the baking time removed most of the OH groups from the silica surface making the nanocrystals indispersible. The etching process with HF was performed with the idea that it would shed light on why excess red emission was

observed when compared to green emission and it would impart dispersibility to the nanocrystals in water. The etching process was expected to the make the silica rich in OH groups thereby making the nanocrystals dispersible in water. However, the partial etching process did not yield such results. Even the complete etching did not render the nanocrystals dispersible in water.

2.3 Conclusions

A simple change in the experimental conditions resulted in the enhancement of red emission and excellent control over red to green ratio in the upconversion process was observed from Yb^{3+} and Ho^{3+} ions codoped LaF_3 nanoparticles in a silica matrix. IR spectra, upconversion at 77 K and HF etching provided concrete evidence that the ratio of amorphous to crystalline silica is responsible for such big variations in the upconversion properties of these samples. A series of ratios for red to green from 1:2.3 to 23:1 was obtained. The interesting factor is that the ratios could be controlled in a single Yb^{3+} and Ho^{3+} doping composition. However, the nanocrystals embedded in silica after partial and complete etching process did not disperse in water. The process of embedding LaF_3 nanocrystals in a silica matrix and use them as an imaging agent did not yield water dispersible nanocrystals. This led to the strategy to dope lanthanides (Ln^{3+}) in $NaYF_4$ nanocrystals, which were synthesized through an organic route. The as-synthesized nanocrystals did not disperse in water due to their hydrophobic ligands on the surface. Two surface modification strategies will be explored in chapter 3 to render these nanocrystals in water and physiological buffers.

2.4 Experimental Section

2.4.1 Chemicals

All chemicals were obtained from Sigma-Aldrich and were used as such without any further purification. Lanthanide nitrate salts used were of the highest possible purity of 99.9%. An aqueous solution of ammonium hydroxide was used which had a concentration of 28.0 to 30.0 wt%.

2.4.2 Synthesis of LaF_3 nanocrystals co-doped with Yb^{3+} and Ho^{3+} ions

The synthesis of LaF_3 nanoparticles co-doped with Yb^{3+} and Ho^{3+} was adapted from the procedure published by our research group.[123] Citric acid (2 g) was mixed with 35 ml of distilled water which was purged with argon was heated to 75 ^{o}C. Ammonium hydroxide (1.2 ml) was added to bring the pH to between 5.5 and 6. To this solution, 1.33 mmol of lanthanide nitrate ($La_{(1-x-y)}$, Yb_x, Ho_y) salts dissolved in 2 ml of methanol was added drop-wise to the above solution. Following this, 3 mmol of NaF in 2 ml of distilled water was added drop-wise. The reaction was continued for 2 hours which was then cooled to room temperature. Ethanol (40 ml) was used to precipitate the nanoparticles and they were collected by centrifuging at 4500 rpm for 5 minutes to separate the particles. The particles were dried in air overnight to obtain a white powder, which was completely dispersible in water. Nanoparticles with varying doping levels of Yb^{3+} ions were synthesized keeping the Ho^{3+} doping level constant at five mole percent.

2.4.3 Silica sol-gel containing LaF_3 nanocrystals co-doped with Yb^{3+} and Ho^{3+} ions

Silica sol-gel containing LaF_3 nanoparticles co-doped with Yb^{3+} and Ho^{3+} ions was synthesized by adapting the procedure of Sivakumar *et al.*[123] Tetraethyl orthosilicate (TEOS) (2 ml) was mixed with 8 ml of ethanol to which 50 to 60 mg of the LaF_3 nanoparticles co-doped with Yb^{3+} and Ho^{3+} ions dissolved in 2 ml of distilled water was added. HCl of 0.1 M concentration was added in drops to bring the pH between 0 and 1. The sols were then aged for a minimum of 2 to a maximum of 15 days.

Two representative procedures will be described here and the details for all samples are presented in Table 1. The sol-gel sample (1) was aged for 2 days and then dried in a rotary evaporator under vacuum (using an aspirator) for 45 minutes at 78 ^{o}C to get a white powder. The sol-gel powder was then baked in a furnace with the following procedure. The sample was heated at the rate of 4 ^{o}C/min to reach 400 ^{o}C and kept at that temperature for 30 minutes. The sample was then heated to 800 ^{o}C at the rate of 3.33 ^{o}C/min, and maintained at that temperature for 12 hours. The sol-gel sample (6) aged for 15 days was dried in a rotary evaporator under vacuum at 78 ^{o}C for 2 hours. Following this the temperature was increased to 92 ^{o}C and kept at that temperature for 11 hours. The dried sol-gel was baked with the following procedure. The sample was heated to 300 ^{o}C at the rate of 3.33 ^{o}C/min and maintained at that temperature for 8 hours. Then the temperature was increased to 500 ^{o}C at 6.66 ^{o}C/min and was kept constant at that temperature for 8 hours. Eventually the sol-gel powder was heated to 800 ^{o}C at the rate of 2.5 ^{o}C /min and baked at that temperature for 12 hours.

2.4.4 HF etching of LaF_3 nanocrystals embedded in a silica matrix

Approximately 225 mg of LaF_3 nanoparticles embedded in the silica matrix were mixed with 36 ml of 1% HF and etched for 3 hours. The particles were centrifuged at 13500 rpm for 20 min which were then washed with 25 ml of water to remove HF. It was observed that 110 mg of particles was obtained after this etching step. The particles obtained from the above etching process were subjected to the same process again. The amount of particles obtained was around 15 to 20 mg.

2.4.5 X-Ray Diffraction (XRD) measurements

XRD patterns in Figure 2.5, Figure 2.6, Figure 2.7, and S8 were measured using the following procedure. Step scan X-ray powder diffraction data were collected over a 2θ range of 3 to 80^o on a Siemens D5000 Bragg-Brentano θ-2θ diffractometer equipped with a Fe monochromator foil, 0.6 mm (0.3°) divergence slit, incident- and diffracted-beam Soller slits, and a VÅNTEC-1 strip detector. Co X-ray tube was operated at 35 Kv and 40 mA using a takeoff angle of 6^o. The scanning step size is 0.04° 2θ with a counting time of 1 s per step. Rietveld refinements were done using the program Topas 3.1 (Bruker-AXS). Patterns in Fig. S6 and S9 were measured with Cr (30 kV, 15 mA) radiation on a Rigaku Miniflex diffractometer using a zero-background holder with variable divergence slit, 4.2° scattering slit, and 0.3 mm receiving slit. The scanning step size is 0.02° 2θ with a counting time of 6 s per step over the 2θ range of 20-140°. The amount of sample was 40 to 50 mg which was ground in an alumina mortar to break up the lumps.

2.4.6 Luminescence Spectroscopy

Upconversion luminescence measurements were carried out with an Edinburgh Instruments FLS920 fluorimeter with the sample being excited with a 980 nm JDS Uniphase laser diode (device- 63-0042) which was coupled to a 105 μm core fiber. To collimate the output of the 980 nm diode laser, an Newport F-91-C1-T Multimode Fiber Coupler was used and an 850 nm long band pass filter was used to block some spurious emissions from the diode laser. The emission was collected using a red-sensitive Peltier-cooled Hamamatsu R955 PMT. The scattered light from the diode laser was removed using an 800 nm short band pass filter. The samples were held in a quartz EPR tube. For low temperature measurements the samples were held in a liquid nitrogen-cooled EPR dewar. The samples were excited with a power density of 80 W/cm^2. There was no visible change in the upconversion spectra or any change in the ratio of red to green due to sample getting heated by the laser power. The ratio of red to green was calculated using the integrated intensity of the respective peaks. All the spectra were corrected for the instrument response.

2.4.7 Energy Dispersive X-Ray Spectroscopy (EDS)

EDS was done using a Hitachi S-3500N scanning electron microscope, operated at 20 kV and a resolution of 102 eV. Dry powdered samples were tagged on to the substrate using a double-sided carbon tape and mounted onto the sample holder. Three measurements were done for each sample to calculate standard deviations.

2.4.8 Infra-red (IR) Spectroscopy

IR spectrum was measured using an IR200 spectrometer from Thermo Instruments (Canada) Inc. Four scans were done for reference and the sample with a resolution of 2 cm^{-1}. Air was used as the reference for the measurement.

Chapter 3. Synthesis and surface modification of $NaYF_4$ nanocrystals doped with Yb^{3+}/Er^{3+} or Tm^{3+} ions

Part of this chapter has been published previously[138] and its being reproduced with permission from Copyright © 2011 American Chemical Society

Part of this chapter has been published previously[139] and its being reproduced with permission from Copyright © 2012 American Chemical Society

3.1 Introduction

As LaF_3 nanocrystals embedded in silica matrix did not disperse in water even with some HF etching, a different strategy had to be adopted. To achieve this, a new matrix, and a new synthetic were chosen. The matrix chosen was hexagonal (β-phase) $NaYF_4$. There are several reports which support the fact that hexagonal (β-phase) $NaYF_4$ is the best matrix for upconversion. There are three major methods to synthesize the $NaYF_4$ nanocrystals doped with the required lanthanides: 1) hydrothermal synthesis; 2) thermal decomposition; 3) coprecipitation. The hydrothermal synthesis requires an autoclave in which the reaction is carried out under high pressures for several hours at temperature between 140 to 200 ^oC.[58,61-62,140-141] The solvent could be water, ethylene glycol, glycol or glycerol. The nanocrystals obtained have good crystallinity; however the final product obtained has a mixture of cubic (α-phase) and hexagonal (β-phase) $NaYF_4$ nanocrystals. The cubic $NaYF_4$ (α-phase) is not as efficient as the hexagonal (β phase) for upconversion. The hexagonal phase $NaYF_4$ is the best known upconversion matrix for lanthanide doping.[71] Furthermore the synthesis yields a mixture of small and big

nanocrystals which also affect the upconversion efficiency. The second method of thermal decomposition process is performed as a two-step process and it involves heating the reaction mixture to temperature of 330 ^{o}C for a few hours.[63,65,68] The precursor salts decompose at such high temperatures to form the nanocrystals. In the thermal decomposition process, the oxide salts were reacted with trifluoroacetic acid to form the trifluoroacetate precursors. Following this, sodium trifluoroacetate, octadecene and oleic acid/oleylamine were mixed with the precursors and heated to 330 ^{o}C and maintained at that temperature for few hours depending on the size needed. Furthermore, during the synthesis, HF and trifluoroacetic acid are released as byproducts.[65,142] This synthesis yields uniform nanocrystals of hexagonal or cubic phase depending on the coordinating ligand. If oleates are used as the stabilizing ligands, hexagonal phase nanocrystals are formed, on the other hand if oleylamine is used cubic phase nanocrystals are obtained.[66-67] A major drawback with the thermal decomposition synthesis is that it is not easily reproducible. This conclusion is drawn from our group's past experience with the thermal decomposition synthesis.

The last method of coprecipitation involves the making the oleate complexes by reacting respective chloride or acetate salts of the lanthandies and yttrium with oleic acid with octadecene as the solvent.[69,143] This is followed by the addition of a fluoride and a sodium source after which the reaction mixture was heated to 300 ^{o}C. The reaction is continued at that temperature for 1 to 2 hours. This synthesis is easily repeatable and gives good control over the uniformity of the nanocrystals formed. In this thesis, the coprecipitation method is the one which has been followed to synthesize the $NaYF_4$

nanocrystals doped with Yb^{3+} and Er^{3+}/Tm^{3+} ions. The synthesis of core and core/shell nanocrystals will be discussed in detail in the results and discussion section. The dopant was changed from Ho^{3+} to Tm^{3+}/Er^{3+} for the following reasons. Thulium can emit at 800 nm through energy-transfer upconversion process by exciting Yb^{3+} at 980 nm. Both the excitation and emission lie in the region where the tissues and cells are the most transparent.[144] Due to this the emission and excitation wavelength will get scattered the least by tissues and cells and possibly one can image deeper inside the tissues than with fluorescent proteins and organic molecules. In case of Er^{3+} ions they are a little more efficient than the Ho^{3+} ions and coupled with the fact that the coprecipitation synthesis cannot be used to control the red to green ratio which was observed with the sol-gel technique.[145] The aim is to employ these nanocrystals as bioimaging agents.

In order to do so, the oleate stabilized nanocrystals dispersed in organic media has to be dispersed in water. There are several surface modification strategies to disperse nanocrystals in aqueous media. 1) encapsulation of nanocrystals with silica;[143,146] 2) ligand exchange;[128,144,146-147] 3) ligand oxidation;[148] 4) intercalation through amphiphilic polymers;[149-150] 5) a crosslinked polymer coating.[151-153] Coating the nanocrystals with silica through a reverse emulsion process has the advantage of not only modifying the nanocrystals to be dispersible in aqueous media but also less toxic. Even though the silica coated nanocrystals are stable in physiological buffers, the inability to remove completely the excess surfactants used for the microemulsion process results in poor colloidal stability over time. This makes the process rather unattractive.[146] In case of ligand exchange process the surface ligands on the nanocrystals are replaced by small

hydrophilic molecules or polymers. The process is rather easy; however the colloidal stability of the nanocrystals in physiological buffers is poor due to the dynamic nature of the small molecules or the polymer and the weak interactions between them and the surface ions of the nanocrystals.[154] The third surface modification method is the ligand oxidation process in which the oleate molecules stabilizing the nanocrystals are oxidized using the Lemieux – von Rudolff agent to convert them to azelaic acid. This makes the nanocrystals dispersible in water for sometime but the process is very long (24 hours) and gives a poor yield.[148] The fourth and fifth strategies will be explored in detail in this chapter. The fourth strategy involves the coating of an amphiphilic polymer on the nanocrystals using a technique called intercalation. The hydrophobic part of the polymer will intercalate (interdigitate) with the oleates on the surface of the nanocrystals while the hydrophilic part of the polymer solvates the water giving dispersibility to the nanocrystals in water. The last method is an extension of the intercalation process. An amphiphilic polymer is coated on the nanocrystals through intercalation followed by crosslinking the polymer using a crosslinking agent. Both the methods are quite successful depending on the amphiphilic polymer used.[155-158]

Colloidal stability is the first criterion to be taken into account if these nanocrystals are to be used as bioimaging agents. In this chapter poly(ethyelene glycol) monooleate (PEG-oleate), an amphiphilic polymer is used to coat the surface of the nanocrystals. PEG-oleate was chosen because it can dissolve in both organic and aqueous solvents and is highly biocompatible due to the presence of PEG moiety. The oleate moiety from the PEG-oleate intercalate with the oleates on the surface of the nanocrystals while the PEG

moiety gives the nanocrystals dispersibility in water. This coating results in colloidal stability of the nanocrystals in water for several days; however the stability in physiological buffers was just around 12 to 15 hours. The reason for such instability is that the polymer ligands are in general dynamic in nature. This leads to the permanent detachment of ligands from the surface of the nanocrystals leading to colloidal instability. This irreversible detachment is caused by the presence of salts in buffers which show high affinity towards lanthanide ions on the surface of the nanoparticle. To overcome this obstacle, there are several reports in which the authors employ intercalation to coat the nanocrystals with an amphiphilic polymer followed by crosslinking of the polymer. The crosslinking effectively reduces the dynamic nature of the coated polymer thereby providing colloidal stability not just in water, but also in physiological buffers and at different pH values. This is important if the coated nanocrystals are to be used *in-vivo*. The polymers most commonly employed for this are polyacrylates,[159] polyimidazoles,[152] polystyrene-block-poly(acrylic acid),[153] poly(*maleicanhydride-alt*-1-octadecene) (PMAO).[155,160] In some cases, amphiphilic dendrimer molecules are also employed to encapsulate the nanocrystals.[161]

This method has been reported for iron oxide and CdSe/ZnS quantum dots. This kind of coating has been reported for lanthanide doped nanocrystals, but not with much success. The reason could be due to the bigger size of the nanocrystals when compared to quantum dots and iron oxide nanocrystals. Moreover, for lanthanide-doped nanocrystals, colloidal stability in water dispersions is regularly reported, however colloidal stability in pH buffers is rarely reported. Stability in serum-supplemented growth media has not been

reported by any research group except ours. Serum-supplemented growth medium is arguably a better mimick of the actual environment in *in-vitro* and *in-vivo* studies (e.g. cell studies and after injection into tail vein of a small animal, respectively).

In this chapter the polymer poly(maleicanhydride-*alt*-1-octadecene) (PMAO) (modified with PEG) is coated over the $NaYF_4$ nanocrystals doped with lanthanide ions. This is done using the hydrophobic interaction between the octadecene chain of the polymer and the oleate ligand on the surface of the nanoparticles, followed by crosslinking the anhydride rings of the PMAO with bis(hexamethylene)triamine (BHMT). There are three major reasons for choosing the amphiphilic polymer PMAO: 1) the anhydride rings can be crosslinked; 2) functionalizing the polymer with e.g. PEG-amine makes it biocompatible; 3) the octadecene chains in PMAO can intercalate with the oleate chains present on the surface of the nanoparticles. These hydrophilic shell crosslinked coated nanocrystals exhibit high stability at different pH values, physiological buffers, and biological growth media.

3.2 Results and Discussion

3.2.1 Synthesis and upconversion luminescence of core, core/shell and core/shell/shell nanocrystals

The goal was to make core $NaYF_4$ nanocrystals doped with Yb/Er^{3+} or Yb^{3+}/Tm^{3+} of the size of 30 to 35 nm, after which an undoped shell of $NaYF_4$ was to be grown over the core nanocrystals. The luminescence efficiency of the nanocrystals scales with its size and the number of lanthanide ions doped in each particle. The emission from smaller particles tends to get quenched by solvents, ligands and surface defects. The size of 30 to

35 nm was chosen to make sure that the nanocrystals are efficient, coupled with high crystallinity and low surface defects. Furthermore, if the size is too big (> 45 nm), they do not disperse well in organic and aqueous solvents. An undoped shell over the core nanocrystals will improve the luminescence efficiency to a great extent because it will effectively shield the core from getting affected by ligands and solvents. The synthesis of $NaYF_4$ nanocrystals codoped with either Er^{3+}/ Yb^{3+} or Tm^{3+} / Yb^{3+} ions employed in this chapter were synthesized using a procedure reported by Zhang *et al.* with some slight modifications.[69] Nanocrystals with a particle size of ~35 nm were originally synthesized using a one pot synthesis with a low oleic acid to octadecene ratio. Unfortunately, these nanocrystals lacked sufficient colloidal stability in organic solvents to enable further functionalization.

In response, nanocrystals with a particle size of ~ 32 nm were synthesized using a core/shell approach that exhibited colloidal stability on par with ~ 18 nm core nanocrystals. The increase in colloidal stability can be attributed to a higher ratio of oleic acid to octadecene in the core/shell reaction mixtures. The average size of the core nanocrystals synthesized was 18 ± 1 nm with the core/shell being 23 ± 2 nm and the core/shell/shell synthesis forming 28 ± 2 by 30 ± 2 nm nanocrystals (Figure 3.1 A-C). Near-monodisperse core nanocrystals were obtained by carrying out the synthesis at 300 ^{o}C for 70 minutes. The core/shell and core/shell/shell nanocrystals with high monodispersity were synthesized by increasing the reaction time to 120 and 150 minutes, respectively. A shorter reaction time resulted in a bimodal distribution of small and large nanocrystals (Figure B.1). The XRD patterns (Figure 3.1E) confirm that the nanocrystals

were of the pure hexagonal phase with no cubic phase impurities. The size of the nanocrystals was further confirmed from XRD measurements using Scherrer's equation. EDS measurements (Figure B.2) confirmed that the doping level of Ln^{3+} ions were very close to the amounts added in the reaction pot. Furthermore, our group has shown strong evidence for the formation of core/shell lanthanide nanoparticles using the aforementioned synthesis procedure and it is concluded that the same is true for core/shell nanocrystals.[162-163]

The $NaYF_4$ core nanocrystals codoped with 2 mol% Tm^{3+} and 20 mol% Yb^{3+} (Figure 3.1D) ions emit a weak 475 nm blue emission which comes from the $^1G_4$ to $^3H_6$ transition and a strong near-infrared emission (800 nm) from the $^3H_4$ to $^3H_6$ transition. Doping of 2 mol % Tm^{3+} ions in the sample results in cross relaxation between the $^3F_2$ energy level of one Tm^{3+} ion to the $^3F_3$ energy level of a nearby Tm^{3+} ion. This quenches the blue emission and results in a relative enhancement of the 800 nm emission (Figure 3.1D).[63,65,74,121] The luminescence efficiency of the Ln^{3+}-doped nanocrystals depends on their size and the amount of Ln^{3+} doping inside the matrix. On average, an 18 nm NC with 2 mol % Tm^{3+} has about 950 Tm^{3+} ions. In order to increase the number of Tm^{3+} ions, a shell of the same composition as the core was grown over the 18 nm nanocrystals thereby augmenting the luminescence efficiency by a factor of 9. As several reports suggest quenching of the upconverted emission by ligands and solvent molecules, an undoped shell of $NaYF_4$ was grown over the core/shell nanocrystals which helped to further increase the intensity by a factor of 2.5 when compared to the core/shell nanocrystals and an overall increase of 24 when compared to core nanocrystals (Figure

3.1D).[69,143,147,164-165] The augmentation factors observed for the intensity of core/shell and core/shell/shell are lower estimates due to the fact that the same weight percent of nanocrystals has been taken into consideration in these experiments.

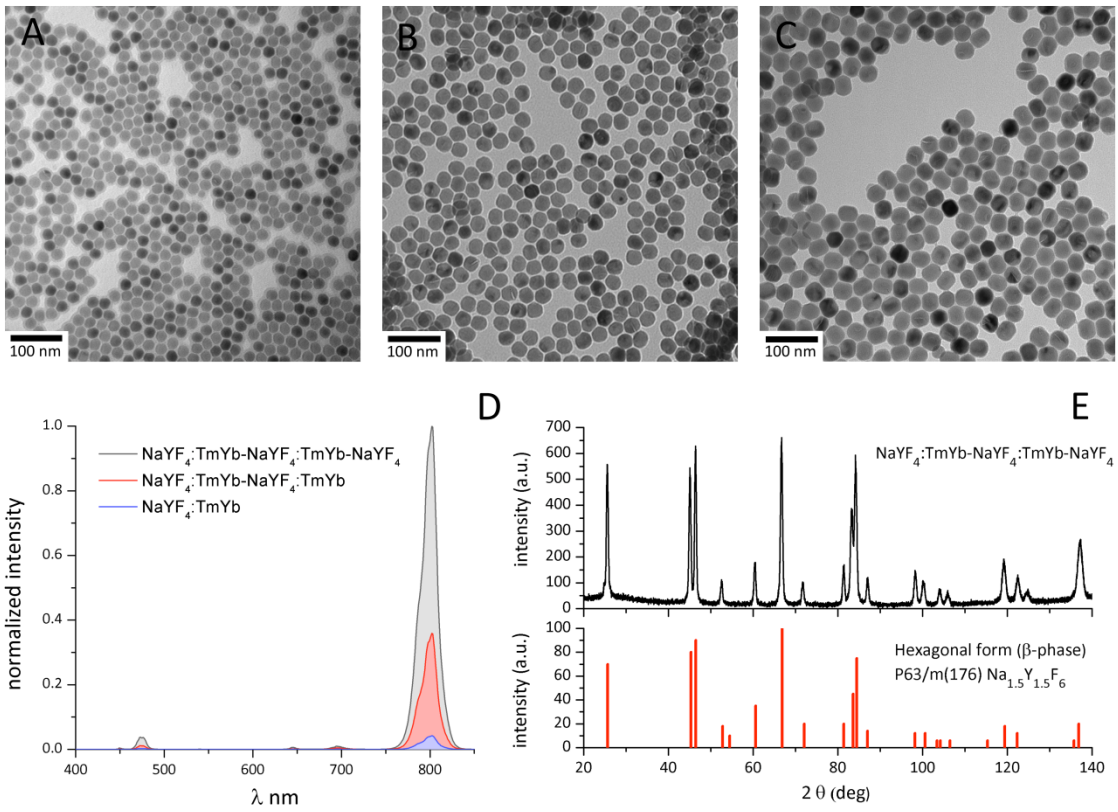

Figure 3.1. TEM of (A) Core;$NaYF_4$:Yb(20%):Tm(2%), The small shadow around the nanocrystals appears when the nanocrystals are not washed more than twice. (B) Core/shell; $NaYF_4$:Yb(20%) :Tm(2%)/$NaYF_4$:Yb(20%):Tm(2%); (C) Core/shell/shell; $NaYF_4$:Yb(20%):Tm (2%)/$NaYF_4$:Yb(20%):Tm(2%)/$NaYF_4$; (Mole% mentioned in the caption for Yb^{3+} and Tm^{3+} ions are the amounts present in the reaction mixture; (D) Upconversion spectra for core, core/shell, core/shell/shell upon 980 nm excitation. All the three samples ($CHCl_3$ dispersion) were of the same wt% for comparison; (E) XRD spectra of core/shell/shell nanocrystal.

3.2.2 Intercalation of PEG-oleate into oleate ligands present on the surface of the nanocrystals

PEG-oleate (Figure 3. **2**) was chosen to modify the surface of Ln^{3+}-doped $NaYF_4$ nanocrystals because of its biocompatibility, low toxicity, and ability to render the nanocrystals dispersible in water, as well as physiological buffers, making them viable as biolabeling agents. PEG-oleate is a polymer that disperses both in water and organic solvents due to the presence of a PEG moiety. Depending on the orientation, the oleate ligand occupies an average area of ~25 $Å^2$ on the NC when it is perpendicular and ~235 $Å^2$ when it is parallel to the surface of the NC.[166] The surface of a NC is highly curved which, assuming that there is a monolayer of oleate molecules on the surface, results in voids between adjacent ligands. Hence, it is hypothesized that the oleate moiety of the PEG-oleate polymer intercalates with the original oleate ligands on the surface of the NC as shown in the schematic representation (Figure 3.3A) leaving the PEG moiety orientated toward the exterior solvent imparting water dispersibility.[155,157,167-168] Excess PEG-oleate present during the surface modification was then removed via preparative centrifugation leaving only the polymer intercalated with the nanocrystals to stabilize them. The oleate moieties of the polymer and the surface oleate ligands of the nanocrystals interact with each other through the hydrophobic effect, thereby minimizing their exposure to water. This effect, in principle, should reduce quenching of the excited states of the Tm^{3+} ions by shielding them from water molecules making the nanocrystals more efficient than ones dispersed in water via ligand exchange. The intercalation process is straightforward, results in no observable aggregation of the nanocrystals, and has no effect on their size and shape as evident from TEM imaging (Figure 3.3 B & C).

In addition, the presence of a hydroxyl group on the end of the PEG chain in the polymer will further facilitate its functionalization and conjugation with antibodies enabling the nanocrystals to be employed in targeted biolabling and tumor cell imaging.

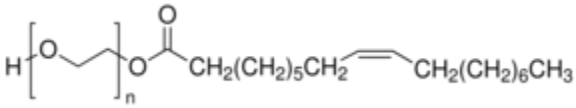

Figure 3. 2. Structure of Polyethyleneglycol-monooleate (PEG-oleate)

After intercalation the core nanocrystals dispersed in water were stable for months at ambient temperature while the core/shell/shell nanocrystals were stable for 6 weeks before settling started to occur. The core/shell/shell nanocrystals could be dispersed back into water by sonicating for 15 to 20 minutes after which the dispersion remained stable for 3 to 4 days. The decrease in stability could be attributed to the larger size of the nanocrystals (30 nm) coupled with the absence of excess polymer ligands to stabilize it in water. A clear dispersion of core/shell/shell nanocrystals was obtained for solutions with concentrations as high as 0.5 wt% while increased light scattering by the core/shell/shell nanocrystals coupled with their increased number resulted in a slight haziness for a 1 wt% dispersion (Figure B.3).

When intercalated core/shell/shell nanocrystals doped with Tm^{3+} and Yb^{3+} were dispersed in water a reduction in the intensity of 800 nm emission was observed when compared to the dispersion in chloroform for the same weight percent (Figure 3.3 D). The reduction in intensity after intercalation is due to the absorption of the 980 nm excitation light by water. The emission intensity observed has decreased by a factor of 2 for core/shell/shell nanocrystals dispersed in water when compared to chloroform. The

observed intensity is still higher than that of core/shell and core nanocrystals in chloroform by a factor of 1.25 and 12, respectively. A comparison between the dispersion of core/shell nanocrystals in water and D_2O (Figure 3.3 E) was also done where a 3 times decrease in the intensity for the dispersion in water was observed. This decrease in intensity is attributed to the absence of an undoped shell to protect the dopant ions, coupled with the absorption of the 980 nm excitation wavelength by water. In the case of Er^{3+} and Yb^{3+}codoped $NaYF_4$ nanocrystals, upon excitation at 980 nm a dominant green emission ($^4S_{3/2}$ and $^2H_{11/2}$ to $^4I_{15/2}$ transitions) accompanied with a red emission ($^4F_{9/2}$ to $^4I_{15/2}$ transition) was obtained (Figure B.4A). Both are two-photon processes which can be concluded from the power dependence curves in Figure B.5. It has been reported that Er^{3+}, Yb^{3+} codoped systems show quenching of emission due to water after a ligand exchange process which substantially decreases the overall intensity accompanied by a significant increase in the red to green emission ratio (Figure B.4B).[128,146-147,169]

In case of intercalation process, water is unable to reach the surface of the nanocrystals thereby causing a reduction in quenching and aid in maintaining a similar ratio of the red to green emissions as present before intercalation. The quenching of emission in water after the intercalation process is much lower than those reported in the literature which involves ligand exchange. It is thus concluded that the core/shell/shell approach for synthesizing the nanocrystals in combination with the intercalation of PEG-oleate into the oleates ligands on the surface of the nanocrystals restricts the access of water molecules to the emitting lanthanide ions resulting in significantly less quenching when compared to nanocrystals modified by ligand exchange.

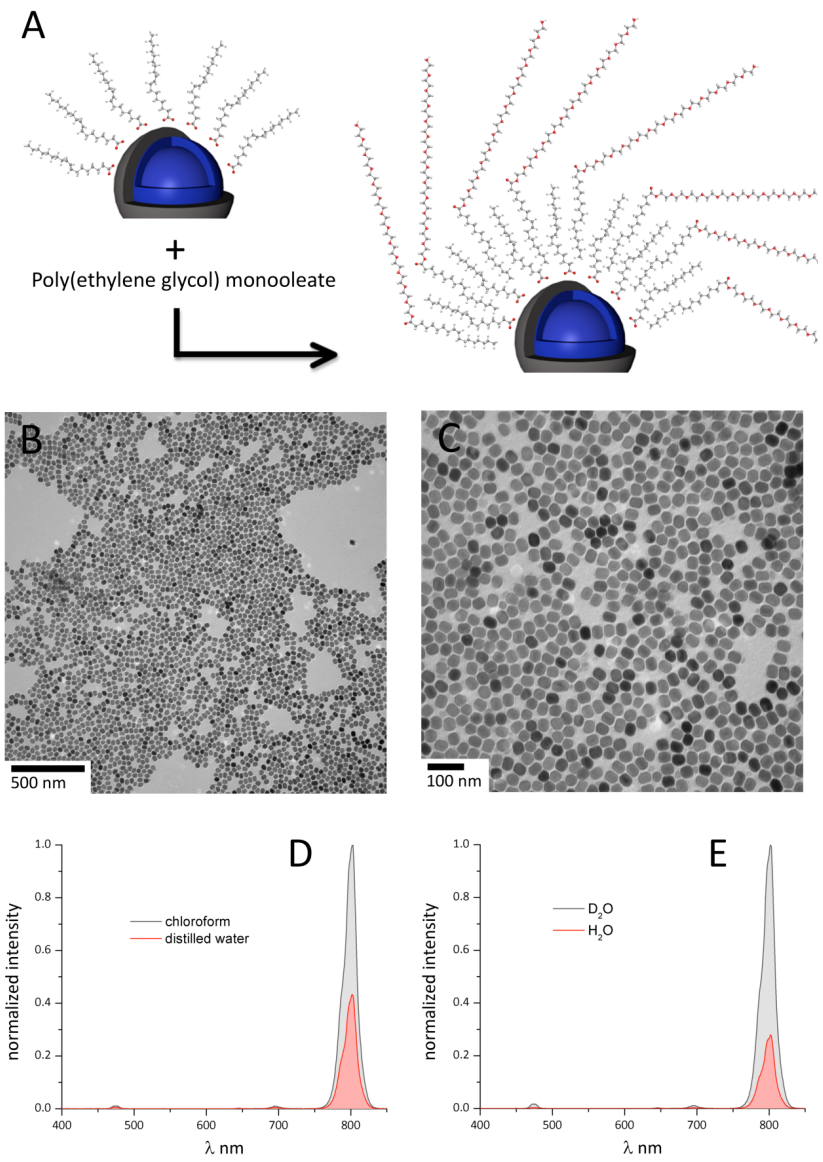

Figure 3.3. (A) Schematic representation of the nanocrystal before and after intercalation; (B-C) TEM of core/shell/shell; $NaYF_4$:Yb(20%):Tm(2%)/$NaYF_4$:Yb(20%):Tm(2%)/$NaYF_4$ after PEG-oleate intercalation into the oleate ligands on the surface of the nanocrystal (dispersion in water); (D) Upconversion spectra of core/shell/shell;$NaYF_4$:Yb(20%):Tm(2%)/$NaYF_4$:Yb(20%):Tm(2%)/ $NaYF_4$ intercalated sample in chloroform and water upon 980 nm excitation. Same wt% of nanocrystals was used for comparison; (E) Comparison of PEG-oleate coated core/shell;$NaYF_4$:Yb(20%):Tm(2%) /$NaYF_4$:Yb(20%):Tm(2%) nanocrystals in water and D_2O.

3.2.3 Stability of PEG-oleate coated water dispersible nanocrystals in various buffers

The stability of the intercalated nanocrystals dispersed in (pH ~7.4, 150 milli-osmomolar) physiological TRIS or phosphate saline buffers was investigated so that it can be predicted whether the nanocrystals will be stable, when injected into the blood stream of an animal. If the nanocrystals aggregate as soon as they are injected they may block the blood stream resulting in rupture of blood vessels and will hence not circulate through the whole body. This would not allow us to image different parts of the animal body or a specific target inside the body. In addition to this, aggregation of nanocrystals will result in the death of the animal, obviously impeding the imaging of live animals.

A NC dispersion (0.07 wt%) in TRIS-buffered saline (pH ~ 7.4) was stable for a period of 1 week, after which they started to settle down slowly. The nanocrystals could be redispersed by sonicating for 15 to 20 minutes after which they remained stable for 2 to 3 days. Stability of the nanocrystals in phosphate-buffered saline (pH ~ 7.4) was around 12 hours after which the nanocrystals started to settle down slowly. When the dispersion was sonicated for 15 minutes the nanocrystals could be dispersed back into the solution and the dispersion remained stable for another 4 to 5 hours. Nanocrystals (1 wt%) dispersed in iso-osmotic TRIS-buffered mannitol (220 milli-osmomolar) were stable for more than a month with little or almost no precipitation. When injected into a mouse, the TRIS-buffered mannitol NC dispersion reached the lungs, liver, and brain without coagulating the blood via aggregation. Even though mannitol can be used to mimic the osmomolarity provided by sodium chloride, it is imperative to come up with a surface modification

process that will exhibit stability in physiological saline buffers, serum-supplemented growth media, and at different pH values. All the aforementioned media are good mimics of biological system. The next section will employ the same intercalation process to coat the nanocrystals with a large amphiphilic polymer which is further crosslinked to make the nanocrystals stable in aforementioned media.

3.2.4 Intercalation of PEG-amine functionalized PMAO into the oleates of the $NaYF_4$ nanocrystals followed by crosslinking of the polymer

The $NaYF_4$ nanocrystals doped with Yb^{3+} and Er^{3+} ions are generally dispersed in chloroform before transfer to the hydrophilic phase. The nanocrystals were transferred to water by coating them with poly(maleicanhydride-*alt*-1-octadecene) (PMAO) (Figure 3.4) modified with amine-functionalized poly(ethyleneglycol) (PEG-amine). Following this the polymer was crosslinked with bis(hexamethylene)triamine (BHMT). A schematic representation is shown in Figure 3.5. The hydrophobic octadecene chains of the PMAO intercalates with the oleates on the surface of the nanocrystals while the PEG chain renders the nanocrystals dispersible in water. The PMAO-PEG coated nanocrystals dispersed in water were subsequently crosslinked with BHMT. The polymer PMAO was functionalized with PEG-amine to make it biocompatible. There are around 110 anhydride rings out of which 30 are functionalized with PEG-amine. This is the best ratio to make polymer biocompatible. The coated polymer before crosslinking generally is dynamic and results in the loss of dispersion stability in water and buffers. However, the crosslinking of the polymer restricts its mobility thereby increasing the colloidal stability of the polymer-coated nanocrystals in water. The ratio of BHMT to PMAO is 20:1 which

will crosslink about 60 anhydride rings per polymer chain. The functionalization of PMAO with PEG-amine and the crosslinking of the polymer with BHMT result in the opening of the anhydride rings to form carboxylic acid and amide groups. The presence of carboxylic acid groups makes the coated nanocrystals viable for further functionalization with bio-molecules. Furthermore the presence of carboxylic acid groups also improves the water dispersibility of the nanocrystals. The intercalation between oleates and octadecene was confirmed by ^{1}H NMR data (Figure B.6). The -CH=CH- from the oleate ligands can be identified from the peaks at 5.2 to 5.4 ppm.[142,170] The presence of amide groups after the reaction was further confirmed the peak at 1635 and 1560 cm^{-1}, respectively from the FTIR spectrum. The presence of carboxylic acid groups can be confirmed from the 1723 cm^{-1} peak. The PEG chain can be confirmed from the peak we observe around 1110 cm^{-1} (Figure B.7).

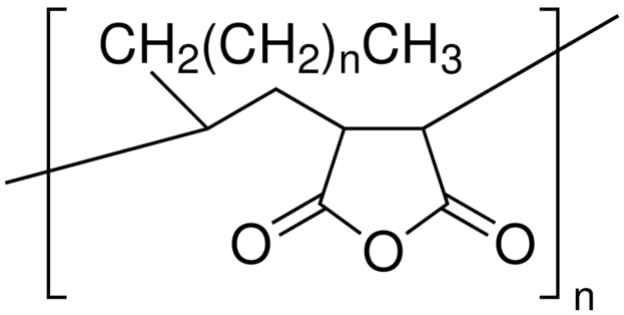

Figure 3.4. Structure of Poly(maleicanhydride-*alt-1*-octadecene)

Furthermore when TGA was performed on the crosslinked polymer it decomposed at a higher temperature than the uncrosslinked one. This increase in the decomposition temperature can be attributed to the crosslinking of the polymer (Figure B.8). The TEM of the polymer-coated nanocrystals clearly indicates that there is no aggregation between

the nanocrystals (Figure 3.6). The polymer-coated nanocrystals showed excellent stability in water for more than two months. The luminescence was retained after the polymer-coated nanocrystals were dispersed in water (Figure 3.7). The luminescence graph show that the red to green ratio did not change from organic solvent to the water (Figure B.4A). This suggests that the emission does not get quenched after being dispersed in water; however the intensity decreases due to the absorption of 980 nm by water. This can be seen from the absorption spectra of the water.

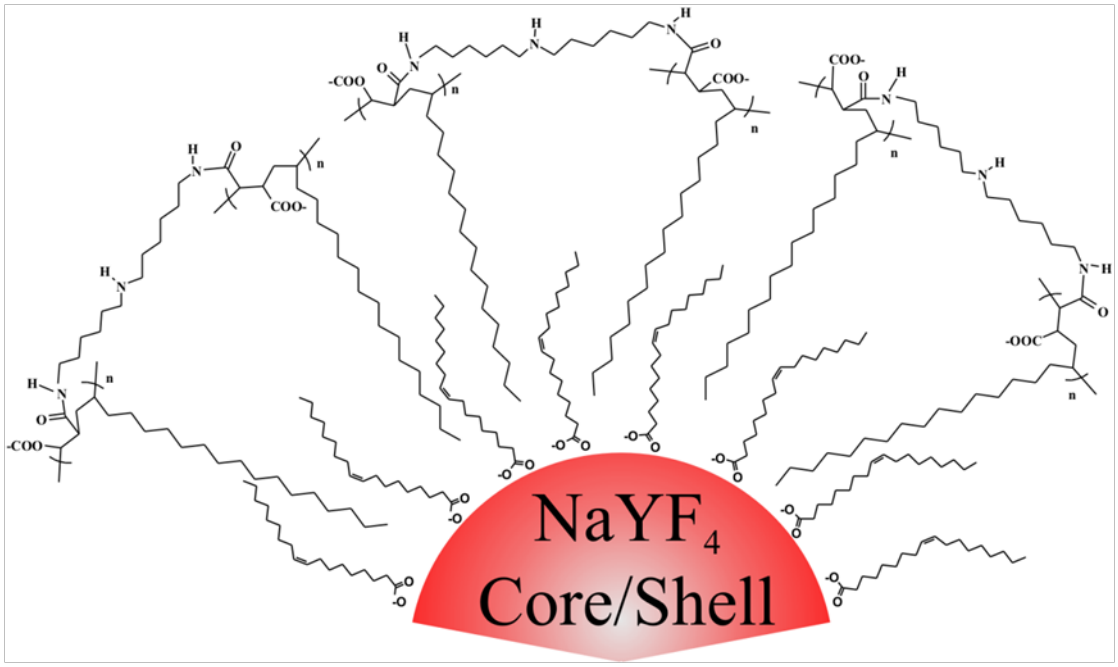

Figure 3.5. Schematic representation of the crosslinked PMAO Coated nanocrystals.

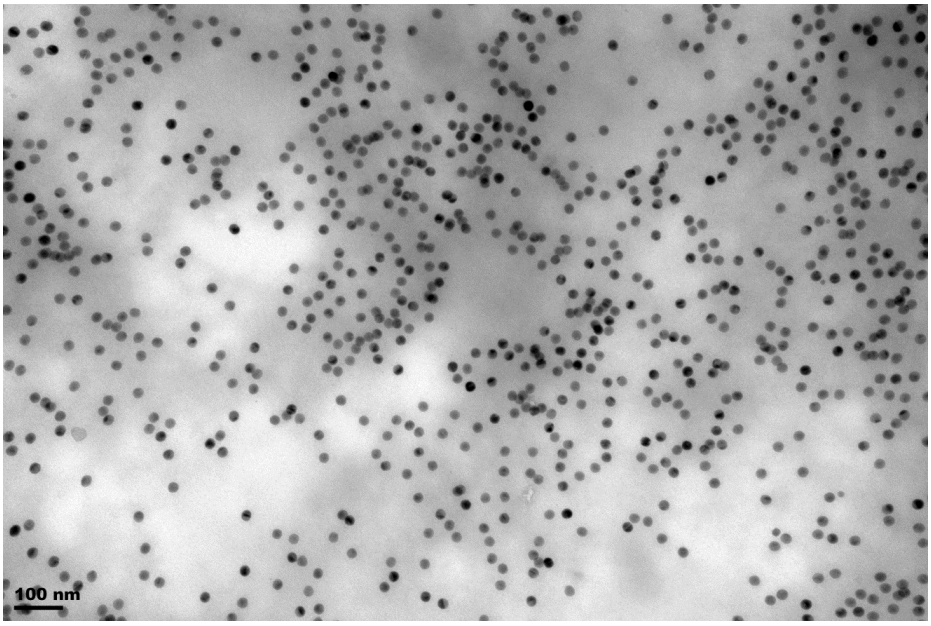

Figure 3.6. TEM image of PMAO-PEG-BHMT coated $NaYF_4$:Yb(20%):Er(2%).

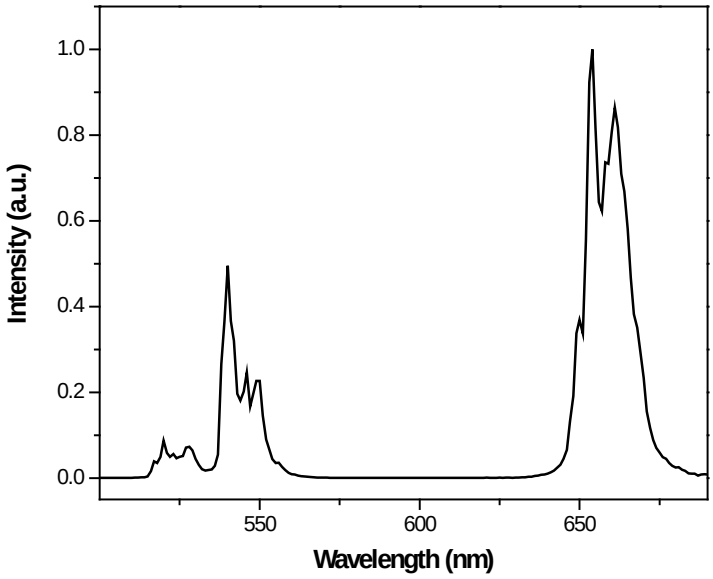

Figure 3.7. Upconversion emission spectrum of core/shell nanoparticles ($NaYF_4$:Yb(20%):Er(2 %)/$NaYF_4$-PMAO-BHMT) in water (~1 mg/ml).

3.2.5 Stability of the crosslinked PMAO-PEG-BHMT polymer-coated nanocrystals in various aqueous media

The crosslinked PMAO-PEG-BHMT coated nanocrystals show excellent stability in water, however it is imperative that they are stable in physiological saline buffers, different pH values and serum-supplemented growth media. The nanocrystals were dispersed in saline phosphate buffer (PBS ~ 7.4 pH) or saline TRIS buffer (TBS ~ 7.6 pH) or saline borate buffer (SBB ~ 8.6 pH). When the nanocrystals were dispersed in the aforementioned buffers (0.3 mg/ml) they were colloidally stable for more than 10 days with no precipitation observed. The Figure 3.8 shows the luminescence of nanocrystals in water on day 1 and the luminescence of nanocrystals in different buffers on day 10. Aggregation of the nanocrystals was not observed which can be confirmed from the fact that the excitation and emission light observed in Figure 3.8 do not get scattered. A TEM of the nanocrystals will confirm this fact; however due to the high salt concentrations in the buffer they will also crystallize in the TEM grid along with the nanocrystals making it very difficult to image.

This improved colloidal stability in buffers can be attributed to the fact that the polymer's restricted mobility due to crosslinking. This was further confirmed from the fact that the uncrosslinked polymer-coated nanocrystals exhibited poor colloidal stability in buffers. In addition to this, from the luminescence graph, it can be found that the red to green ratio has not changed at all when dispersed either in buffer or in water. The PMAO-PEG-BHMT coated nanocrystals show colloidal stability in pH values ranging from 3 to 13 (Figure 3.9). When these nanocrystals were dispersed in serum-supplemented growth

media at 37. 4 ^{o}C they were stable for 2 days (Figure 3.9) after which they started to precipitate slowly. When the nanocrystals were dispersed in the same media at 4 ^{o}C the dispersion was stable for more than 1 week (Figure 3.9). The stability shows that the proteins and the salts in the serum-supplemented growth media do not affect the colloidal stability of the nanocrystals. However, the nanocrystals dispersed in a saline PBS buffer containing calcium and magnesium salts precipitated. This is attributed to the interaction between the divalent cations present in the buffer and the large number of carboxylic acid groups in the polymer. This is a major problem if these nanocrystals are to be injected inside an animal where there are calcium and magnesium ions present.

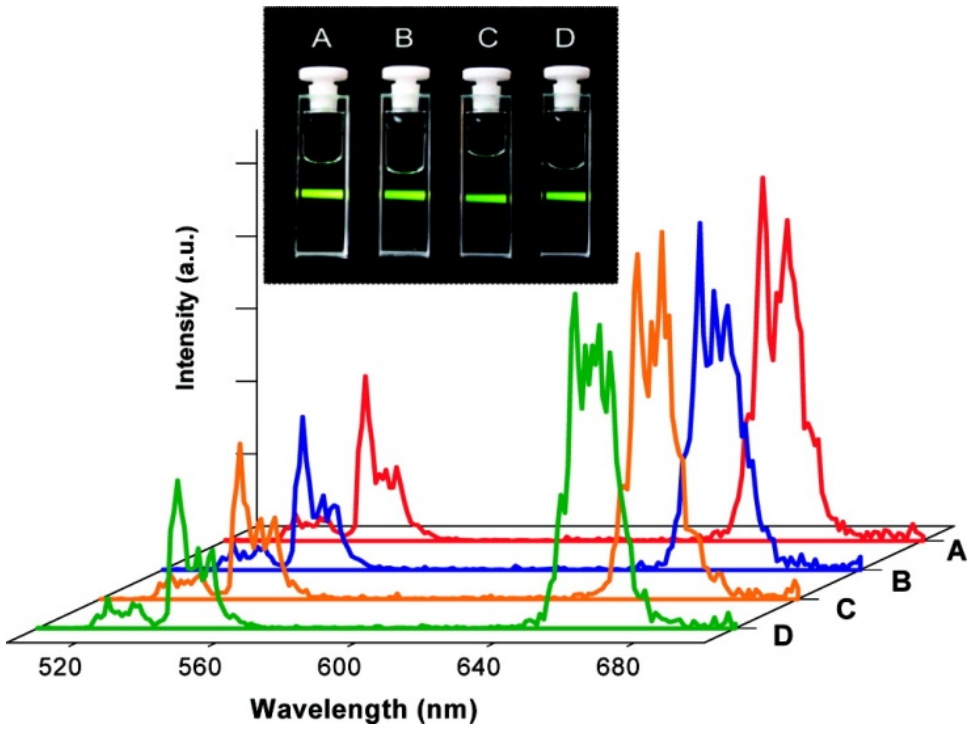

Figure 3.8. Upconversion emission spectra of core/shell nanoparticles ($NaYF_4$:Yb(20%):Er(2%) /$NaYF_4$-PMAO-BHMT) upon 980 nm excitation in (A) water (1 day old sample), (B) tris-buffered saline (TBS), (C) sodium borate buffer (SBB), and (D) phosphate buffered saline (PBS). The buffer dispersions were 10 days old by the time the spectra were measured. (Inset: UCNPs-PMAO-BHMT dispersions under 980 nm excitation).

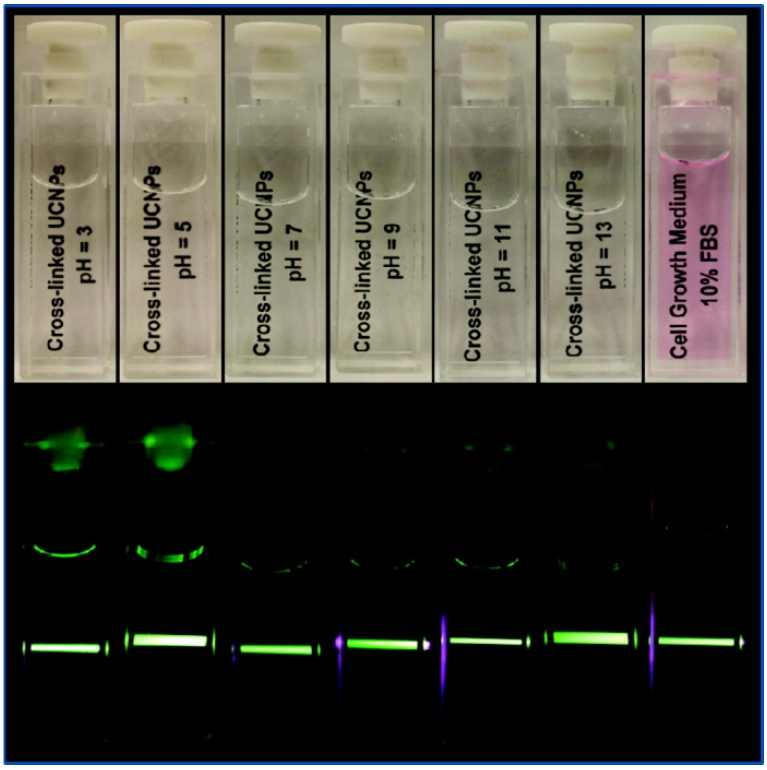

Figure 3.9. Core/shell nanoparticles ($NaYF_4$:Yb(20%):Er(2%)/$NaYF_4$-PMAO-PEG-BHMT) dispersed in water at different pH from 3-13 and serum-supplemented cell growth medium, and respective images under 980 nm excitation (bottom).

3.3 Conclusions

This chapter explains in detail, the synthesis and surface modification of the lanthanide doped nanocrystals. Growing an undoped shell over the doped lanthanide nanocrystals increase the luminescence by a factor of 23 times when compared to the doped core nanocrystals. The undoped shell protects the emission of core nanocrystals from being quenched by solvents and ligands. The surface modification with PEG-oleate resulted in

a stable dispersion in water, however their stability in buffers were poor. The poor stability is due to the detachment of the polymer ligands from the surface of the nanocrystals due to their inherent dynamic nature in solvents. This problem was solved by the second surface modification method by coating the nanocrystals with the polymer PMAO-PEG and then crosslinked with BHMT. This resulted in a stable dispersion in water, physiological buffers and at various pH values. The much improved colloidal stability is due to the fact that the crosslinking restricts the mobility of the polymer coated on to the nanocrystals. This crosslinked polymer coating also made the nanocrystal dispersion stable (> 2-7 days depending on the temperature) in serum-supplemented growth media. Having dispersed the nanocrystals in water and pH buffers the next step is to test their viability as bioimaging agents. The next chapter explains the applicability of these nanocrystals as bioimaging agents.

3.4 Experimental Section

Chemicals

All chemicals were obtained from Sigma-Aldrich and were used as such without any further purification. Lanthanide acetate salts used were of the highest possible purity of 99.9%.

3.4.1 Synthesis of core, core/shell and core/shell/shell $NaYF_4$ nanocrystals

Synthesis of core; $NaYF_4$:Yb(20%):Tm(2%) nanocrystals

A three-necked flask containing 2 millimoles of lanthanide (Y^{3+}, Yb^{3+}, Tm^{3+}) acetate salts along with 12 ml of oleic acid and 34 ml of octadecene was heated to 120 ^{o}C under

vacuum and kept at that temperature for 1 hour and 30 minutes to form lanthanide oleates. After cooling the mixture to room temperature, a solution of methanol (~ 20 ml) containing 10 millimoles of NaOH and 8 millimoles of NH_4F was slowly added and stirred for 1 hour and 30 minutes. Methanol was then slowly evaporated and the mixture was heated at 15 ^oC/min to 300 ± 2 ^oC under an argon atmosphere and maintained at that temperature for 1 hour and 10 minutes. Subsequently the reaction mixture was cooled down to room temperature and the nanocrystals were precipitated using 90 ml of anhydrous ethanol. The nanocrystals were then washed twice with ethanol (120 ml each time) and then dispersed in 22 ml of chloroform. The same procedure was followed when erbium ions instead of thulium ions were used as the codopant with ytterbium ions.

Synthesis of core/shell; $NaYF_4$:Yb(20%):Tm(2%)/$NaYF_4$:Yb(20%):Tm(2%) and core/shell/shell; $NaYF_4$:Yb(20%):Tm(2%)/ $NaYF_4$:Yb(20%):Tm(2%)/$NaYF_4$ nanocrystals

Lanthanide acetate salts (2 millimoles) were added to a three-necked flask along with 12 ml of oleic acid and 34 ml of octadecene and the mixture was heated to 120 ^oC under vacuum and left at that temperature for 1 hour 30 minutes. After cooling the mixture to 80 ^oC, the core nanocrystals dispersed in chloroform were added slowly, followed by slow evaporation of chloroform. Once all chloroform had been evaporated, the mixture was cooled down to room temperature. Methanol (~20 ml) containing 10 millimoles of NaOH and 8 millimoles of NH_4F was added slowly and stirred for 1 hour and 30 minutes. The methanol was slowly evaporated and followed by the rapid heating of the mixture at 15 ^oC/min to 300 ± 2 ^oC under an argon atmosphere and maintained at that temperature for 2 hours. The solution was cooled down and the nanocrystals were precipitated and

washed the same way as the core nanocrystal synthesis. For core/shell/shell nanocrystals the procedure was the same as core/shell with two differences. The shell formed in this case is undoped $NaYF_4$, so 2 millimoles of yttrium acetate salt were taken. The reaction time at 300 ± 2 ^{o}C was 2 hours and 30 min.

3.4.2 Intercalation of PEG-oleate into the oleates present on the surface of nanocrystals

A nanocrystal dispersion (1 wt%) amounting to ~1 g was taken in a vial and mixed with 2 g of poly(ethyleneglycol) monooleate (PEG-oleate - Average molecular weight ~ 860 mol/g) along with 2 ml of chloroform. The mixture was stirred slowly to evaporate the chloroform at ambient temperature. Once the solvent was completely evaporated the mixture was heated to 80 ^{o}C in a water bath after which 10 ml of distilled water was slowly added to disperse the mixture. The mixture was then sonicated for 10 minutes to get a clear and stable dispersion. The nanocrystals were separated from the excess polymer using a prep centrifuge at 25,000 g and the nanocrystals were dispersed in distilled water. The procedure can be done for bigger batches of 7 to 8 g (5 wt% nanocrystals) of dispersion. In that case the polymer (15 g), nanocrystal mixture was allowed to stir for 48 hours after which the chloroform was slowly evaporated. This helps in the intercalation of PEG-oleate in to the oleate ligands present on the surface of the nanocrystal there by improving the stability of the dispersion in water.

3.4.3 Intercalation of PMAO-PEG into the oleates present on the surface of nanocrystals and crosslinking of PMAO using BHMT

nanocrystals (~10 mg) were mixed with 128 mg of PMAO (M_n ~ 30,000 – 50,000) in 10 ml of chloroform. The ratio of polymer to number of nanocrystals is 200 to 1. This ratio is for 15 to 20 nm nanocrystals. The ratio for 5 to 10 nm sized nanocrystals is 30 to 1. The number of anhydride rings per polymer is around 110, out of which 30 are opened with PEG-amine (M_n ~ 2,000). The solvent chloroform was evaporated under a rotary evaporator followed by the addition of water. The mixture was sonicated to disperse the nanocrystals in water. Following this, BHMT (~10 mg ratio of PMAO to BHMT 1 to 20)) was added to crosslink the anhydride rings. The nanocrystals-PMAO-PEG-BHMT mixture was sonicated for 15 minutes followed by 30 minutes of stirring. This was followed by successive filtration through a 0.45 and 0.25 micron filter. The excess polymer was removed from the nanocrystals by centrifuging out the coated nanocrystals with a preparative centrifuge at 25,000 g.

3.4.4 XRD Measurements

XRD patterns were measured with Cr (30 kV, 15 mA) radiation on a Rigaku Miniflex diffractometer using a zero-background holder with variable divergence slit, 4.2° scattering slit, and 0.3 mm receiving slit. The scanning step size is 0.5°, 2θ with a counting time of 2 s per step over the range of 20-140°. The dispersion was added drop wise to form a film on the substrate which was then used for the measurements. The peaks at 45 ^{o} and 48 ^{o} (Fig. S2) were used to confirm the size of the nanocrystals using Scherrer's equation.

3.4.5 Fluorescence measurements

Upconversion experiments were carried out with an Edinburgh Instruments (FLS920 fluorimeter) with the sample being excited with a 980 nm JDS Uniphase laser diode (device- 63-0042) which was coupled to a 105 μm core fibre. Newport F-91-C1-T Multimode Fiber Coupler was used to collimate the beam and a 780 nm long band pass filter was used to block other wavelengths emitted by the diode laser. The emission was collected using a red-sensitive Peltier-cooled Hamamatsu R955 PMT. The scattered light from the diode laser was removed using a 900 nm short band pass filter. A quartz cuvette filled with the dispersion was used for measurement purposes.

3.4.6 Energy Dispersive X-Ray Spectroscopy (EDS)

EDS was done using a Hitachi S-3500N scanning electron microscope, operated at 20 kV and a resolution of 102 eV. The dispersion was dried to get a white powder which was tagged on to the substrate using a double-sided carbon tape and mounted onto the sample holder. Three measurements were done for each sample to calculate the average and the standard deviation.

3.4.7 Transmission Electron Microscope (TEM)

TEM images for nanocrystals were obtained using a Hitachi H-7000 microscope operating at 75 kV which is coupled to a charge coupled device (CCD). Nanocrystal ~ 0.1 wt% dispersion in hexanes were drop casted on to a Formvar/carbon film supported on a 300 mesh copper grid (3 mm in diameter) and allowed to dry in air. The intercalated samples dispersed in water were also imaged in the same way as the previous sample.

The average size and the standard deviation of the nanocrystals were determined by taking an average over 50 nanocrystals.

Chapter 4. Two-photon upconversion laser (scanning and wide field) microscopy using Ln^{3+}-doped $NaYF_4$ upconverting nanocrystals – A critical evaluation of their performance and potential in bioimaging

Part of this chapter has been published previously[138] and its being reproduced with permission from (Copyright © 2011) American Chemical Society

Part of this chapter has been published previously and[139] its being reproduced with permission from (Copyright © 2012) American Chemical Society

The LNCaP cell culture was prepared by Noah Johnson at the Deeley Research Centre. The animal studies were done by Prof. Kerry Delaney (Department of Biology).

4.1 Introduction

In-vivo imaging with fluorescent probes faces several challenges, because of autofluorescence, absorption of light by cells, and tissues, and scatter due to refractive mismatches primarily at the lipid water interfaces of cells. Traditional microscopy techniques (confocal and one-photon) give excellent lateral resolution but photobleaching of the whole sample and poor depth penetration (less than 100 μm) of the excitation (generally UV light) and emission (visible light) wavelengths coupled with lack of optical sectioning (z-axis, *i.e.* axial resolution) confine their usage in imaging applications. However, through the use of two-photon microscopy techniques penetration up to a depth

of ~ 500 μm with an axial resolution up to 2 μm has been achieved.[22,100] Wilfred Denk and his colleagues were the first to employ two-photon laser scanning microscopy (TPLSM) to demonstrate that lateral and axial resolution up to a few micrometers could be obtained by imaging live, cultured pig kidney cells.[23] Many other researchers have since applied this technique to studies in thick scattering biological tissues.[21] TPLSM has the unique advantage of generating photons only at the focal volume of the incident laser light due to the non-linear nature of the two-photon process. Furthermore, the scanning process involved utilizes all the scattered emission light coming from the specimen to construct the three dimensional image of the object by virtue of knowing where the fluorescence originated.

The distinct advantage of this technique to use scattered emission light to reconstruct an image of an object at depths of 400 to 500 μm underneath the tissue is not feasible with conventional one-photon and confocal microscopy.[23] TPLSM is usually accomplished using organic molecules, which have a high molar extinction coefficient and high quantum yield.[17-18,171-173] In the last decade, quantum dots have been studied extensively because of their large two-photon absorption cross section area and increased resistance towards photobleaching compared to that of organic molecules.[16,174-179] Fluorescent proteins have also extensively been used as imaging agents for biological studies and have the unique advantage of being able to be genetically expressed in specific cells.[19-20,180-182] The major obstacle is that expensive pulsed lasers are required to excite organic molecules, quantum dots, and fluorescent proteins through a two-photon excitation process. Excitation of fluorophores can cause photobleaching that is associated with

phototoxicity, which is a major problem in using them as imaging agents for long term cellular imaging. Furthermore organic molecules that emit efficiently in the biological window (where the absorption and scattering of light is the lowest, 800-1100 nm) upon two-photon excitation are not available.

In this chapter, upconverting lanthanide-doped nanocrystals, which convert two lower-energy photons to one higher-energy photon, generally in a step-wise process, is examined as an alternative to the aforementioned materials for imaging. They have some unique advantages such as: [5,51]

1. A stable photocycle resulting in no photobleaching.

2. Emission peaks originate from intra 4f electronic transitions of the lanthanide ions and thus not affected by solvents or ligands bound on the surface.

3. Excitation (980 nm) and emission (800 nm) both fall in the biological window resulting in reduced scattering and hence the possibility of imaging deeper into the tissue increases compared to organic fluorophores, fluorescent proteins, and quantum dots.

4. Cheap excitation source (980 nm CW diode laser)

5. Low power densities are required (in the order of ~ 10 W/cm^2) which would safeguard the tissue from getting scarred and cell death.

6. Step-wise two-photon process with a low power density (~ 5 to 10 W/cm^2) could be employed in TPLSM and wide field microscopy to acquire excellent optical sectioning, *i.e.* depth resolution.

7. Low toxicity from the Ln^{3+}-doped nanocrystals.

The primary reason for selecting hexagonal phase $NaYF_4$ nanocrystals co-doped with either Er^{3+}/Yb^{3+} or Tm^{3+}/Yb^{3+} is their superior upconversion luminescence efficiency versus other matrices.[71] Under 980 nm excitation nanocrystals codoped with Er^{3+}/ Yb^{3+} ions emit in the green and red region of the electromagnetic spectrum while Tm^{3+}/Yb^{3+} codoped samples emit in the blue and near infra-red region (800 nm). The most efficient nanocrystals are generally synthesized in an organic medium[65,69,113,143,183-184] stabilized with an organic ligand, followed by surface modification of the nanocrystals through ligand exchange or silica coating to render them water dispersible. There are several reports, which employ green and red light from upconversion using Yb^{3+} and Er^{3+} codoped nanocrystals to image isolated cells and binding of antibody complexes to tumors in mice. Li and coworkers were the first to show that two-photon upconversion laser scanning microscopy (TPUSLM) can be performed with upconverting $NaYF_4$ nanocrystals doped with Yb^{3+} and Er^{3+} ions.[185] The scanning speed of 2 μs/pixel employed by the authors resulted in smearing of images in the direction of scanning due to the long lifetimes of the excited Er^{3+} ions doped in the nanocrystals. The smearing occurs due to the fact that the detector still receives signal from the pixel it has previously scanned due to the long lifetimes even though the scanner has moved onto the next pixel. The authors have solved the problem by descanning the emitted light with a pinhole

which collected the light only from the pixel which is being scanned by the detector. The major drawback is that, to obtain enough photon/sec at a scanning speed of 2 μs/pixel, the sample has to be excited at a power density ~ 10^5 W/cm^2 where the two-photon process is completely saturated throughout the excitation cone, resulting in the loss of optical sectioning intrinsic to a two-photon process. The same group mentioned elsewhere that they observed a good signal to noise at depths of 600 μm using red emission from Yb^{3+} and Er^{3+}codoped nanocrystals.[186] However, the problem of poor resolution obtained due to high scatter of light by tissues at such depths and the saturation of the two-photon process at a power density of ~ 10^5 W/cm^2 was not taken into consideration by the authors.

A viable approach to reduce the scattering problem is to use the 800 nm emission from Tm^{3+} ions through upconversion when codoped with Yb^{3+} ions in $NaYF_4$ nanocrystal. However, there are only a few reports which employ 800 nm emission for imaging purposes compared to that of green and red emission obtained from Yb^{3+}, Er^{3+} codoping.[144,186-188] Prasad and coworkers were the first to utilize 800 nm emission from Tm^{3+} ions to image fixed cell lines and perform whole body imaging of a mouse showing that imaging is viable with 800 nm emission from Tm^{3+} ions.[189] Kobayashi and coworkers reported the observation of a good signal to noise ratio at a power density of 250 mW/cm^2 when imaging the lymph nodes of a hairless mouse through the skin using 800 nm emission.[187] They added that due to poor recovery of the green fluorescence from Er^{3+} ions affected by scattering, peeling the skin off the mouse alone resulted in a good signal to noise ratio for the lymph node images. Xiong *et al.* reported the use of 800 nm

emission in locating tumors in a mouse using antibody-conjugated nanocrystals.[186] Our group has also shown that images of cell lines could be obtained using 800 nm emission and have given evidence that the nanocrystals were indeed taken up by the cells using TEM.[147]

The major limitation with all these reports, including ours, is that the lateral and axial resolutions necessary to identify a small object inside a cell or a mouse were not explored or demonstrated. Moreover, there are no reports in literature that show the extent to which one can image below the surface of the skin without the loss of lateral and axial resolution using 800 nm emission when compared to the predominantly used green fluorescence from organic molecules, quantum dots, and fluorescent proteins. In this chapter the axial and lateral resolution obtained for images at different depths inside the tissue by using lanthanide-doped $NaYF_4$ nanocrystals as the imaging agent will be explored with the help of two-photon upconversion laser scanning microscopy (TPULSM) and two-photon upconversion wide field microscopy (TPUWFM).

4.2 Results and Discussion

4.2.1 Two-photon upconversion laser scanning microscopy (TPULSM)

Scanning a glass slide coated with Er^{3+}, Yb^{3+} doped $NaYF_4$ nanocrystals at a speed of 2 µs/pixel resulted in no signal (green emission). However an image (Figure 4.1 A) with a poor lateral resolution, *i.e.* the x-y plane, caused by smearing in the scanning direction was obtained at a speed of 25 µs/pixel with which the shape and the size of the aggregated nanocrystals could not be determined. As the scanning speed was decreased

from 25 to 500 µs/pixel, images (Figure 4.1 B-D) with enhanced lateral resolution were observed due to the decrease in smearing. The shape and the size of the aggregate nanocrystals were clearly observed with the scanning speed of 500 µs/pixel. The decrease in scanning speed was necessary to counteract the poor quantum yield of the upconversion process[145] and the smearing of light onto the adjacent pixels due to the slow photocycle (450 µs)[190] of the nanocrystals. Fast scan speeds (2 µs/pixel) can be achieved by introducing a pinhole which necessitate the increase in power density (10^5 W/cm^2) resulting in the saturation of the two-photon process throughout the excitation cone, triggering the loss of axial resolution (optical sectioning, z axis). The drawback of slow scan speeds is that it requires several minutes to scan the whole slide in the lateral direction while not scanning in the axial direction. Scanning in the axial direction over a depth of 250 µm with a 5 µm step size coupled with a slow scan speed (500 µs/pixel) in the x-y plane will require a few hours for a stack of images which is not practical for experimental purposes.

One of the issues with two-photon imaging using the green fluorescence from organic molecules and quantum dots is the loss of lateral resolution beyond depths of 500 µm in tissue due to poor recovery of light induced by scatter.[191-192] In order to observe the lateral resolution obtainable at different depths using 800 nm light, Tm^{3+}, Yb^{3+} codoped $NaYF_4$ nanocrystals were employed as an imaging agent with agar-milk gel as an artificial tissue phantom. Three-fourths of a 50 µm cuvette filled with a NC dispersion (core/shell/shell;$NaYF_4$:Yb(20%):Tm(2%)/$NaYF_4$:Yb(20%):Tm(2%)/Na YF_4) was

covered with an agar-milk gel shaped as a wedge. Agar-milk gel was chosen because of its ability to mimic the scattering characteristics of the brain of a mouse.[193]

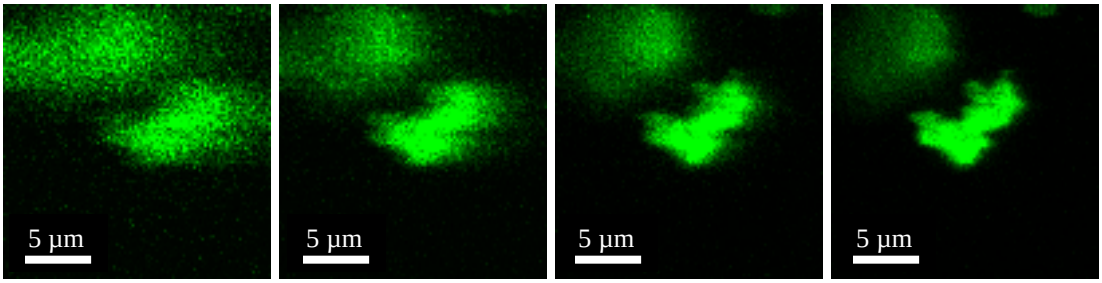

A) 25 µs/pixel B) 100 µs/pixel C) 250 µs/pixel D) 500 µs/pixel

Figure 4.1. $NaYF_4$:Yb(20%):Er(2%) nanocrystals coated on a slide depict the decrease in the smearing of light from one pixel to another pixel and the increase in resolution of the image as the scanning speed is reduced from 25 µs/pixel to 500 µs/pixel. The area of each image is 100 by 100 pixels with each image being an average of 3 frames. Scanning was done from left to right. The power density employed was 100 W/cm2. An Olympus 40X 0.8 NA water dipping lens was used for imaging. These images are false colored.

When imaging was performed the lateral resolution necessary to observe the edges of the cuvette diminish as the thickness of the agar-milk gel increases (Figure 4.2 A-F). The edge of the cuvette could not be identified clearly after a depth of 600 µm. This could be seen from the intensity profile graph which shows the decrease in the sharpness of the profile coupled with the diminishing intensity. The lower emission intensity is attributed to increased scatter and absorption of the incident laser light which results in a lower excitation density as we go deeper inside the gel. The intensity profile curve (Figure 4.2 G) obtained for the edge of the cuvette in the absence of agar-milk gel shows a sharp increase in intensity at the edges of the cuvette and the number of pixels necessary to

define it is around 150. As the agar-milk gel thickness increases the intensity profile curve becomes a Gaussian (Figure 4.2 H) and keeps broadening at greater depths. This is observed from the augmentation in the number of pixels necessary to define the edge of the cuvette (Figure 4.2 H) from the initial 150. For instance, as we reach 600 µm deep inside the agar-milk gel the number of pixels increase to ~ 275 (Figure 4.2 H) hence showing the 20 µm size cuvette as a 35 µm one. At a depth of 1100 µm the number of pixels increases to ~ 425 (Figure 4.2 H) which makes the 20 µm size cuvette resemble a 48 µm cuvette, a resolution decrease of 275 %. Consequently, imaging beneath the surface at depths greater than 600 µm could only become an option with tissues that do not scatter as much as brain tissues.

To test the viability of imaging in live tissues, images of mouse lungs were obtained with core/shell/shell $NaYF_4$ nanocrystals using the TPULSM technique (Figure 4.3). The alveolar capillaries inside the lungs could easily be visualized with a scanning speed of 200 µs/pixel with an axial resolution of 25 µm. The poor axial resolution is an implication of the saturation of the stepwise two-photon process at a power density of 2000 W/cm^2. Axial resolution close to 5 or 10 µm could possibly be obtained by employing a power density of 30 to 50 W/cm^2 with the help of a more sensitive PMT at 800 nm coupled with a slower scanning.

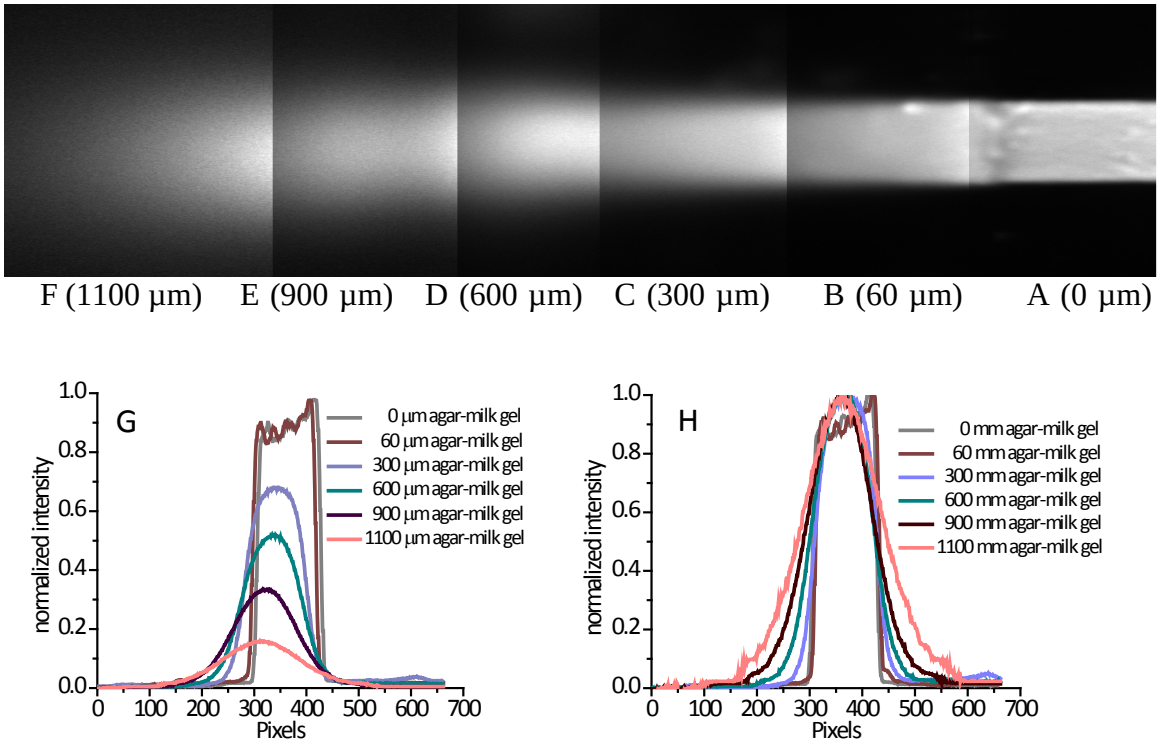

Figure 4.2. Images showing the decrease in spatial resolution with increase in thickness of the agar-milk gel. Thickness of agar-milk gel (A) 0 µm, (B) 60 µm, (C) 300 µm (D) 600 µm (E) 900 µm (F) 1100 µm. (G) Intensity profile showing the decrease in lateral resolution and intensity with increase in agar-milk gel thickness. The profiles were drawn by taking the intensity across the cuvette as indicated in panel A. (H) Intensity profiles broadened with increased agar-milk gel thickness leading to decreased resolution as seen in images (A- F). An Olympus 10X 0.4 NA air lens was used to image with a power density of 2000 W/cm^2. Core/shell/shell;$NaYF_4$:Yb(20%):Tm(2%)/$NaYF_4$:Yb(20%):Tm(2%)/$NaYF_4$ nanocrystals dispersed in water were used for this purpose.

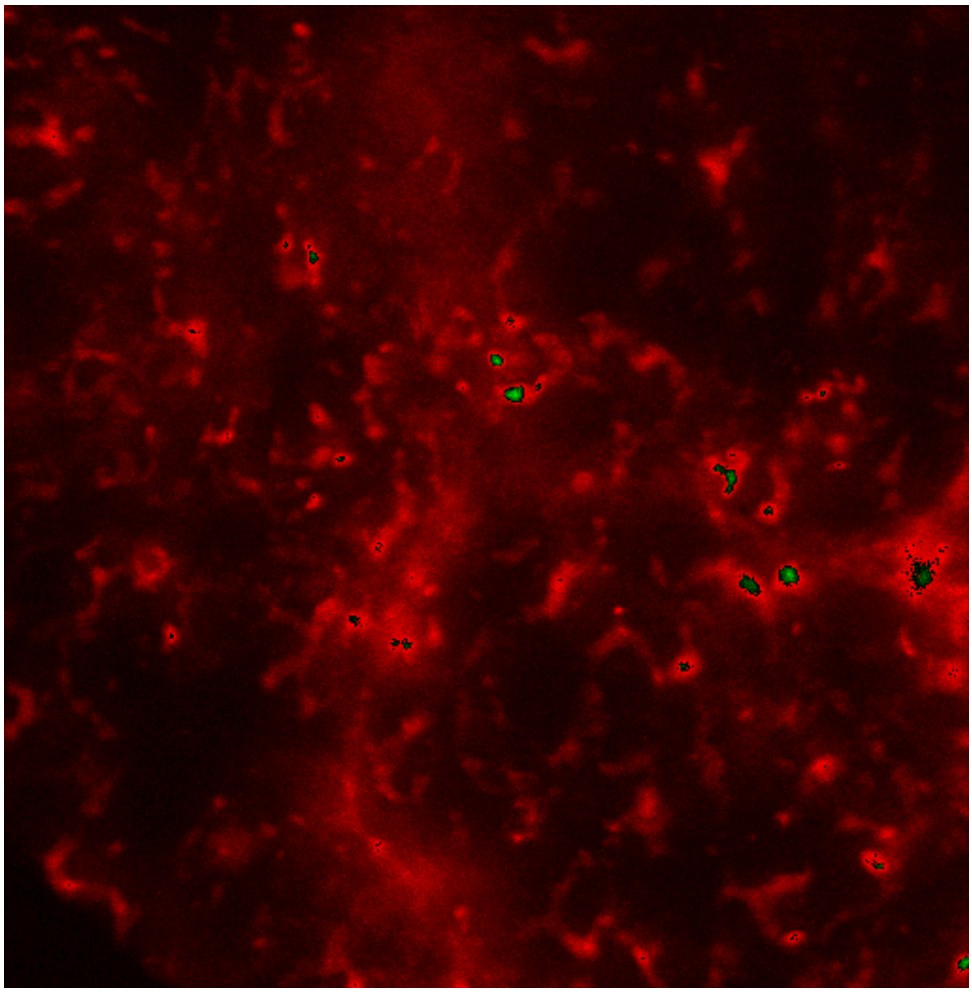

Figure 4.3. Image showing the capillaries surrounding alveoli in the lung tissue of a mouse using TPULSM. A scanning speed of 200 µs/pixel with a laser power density of 2000 W/cm^2 was used. The image shown here is a maximum intensity projection of 5 successive images taken at 25 µm intervals along the z-axis. 800 nm emission upon 980 nm excitation from Core/shell/shell;$NaYF_4$: Yb(20%):Tm(2%)/$NaYF_4$:Yb(20%):Tm(2%)/Na YF_4 nanocrystals were employed for imaging the lungs. The image has a resolution of 512x512 pixel with an area of 250 µm^2. An olympus 40 X 0.8 NA water dipping lens was used for imaging. The image is false colored.

4.2.2 Two-photon upconversion wide field microscopy (TPUWFM)

Two-photon upconversion wide field microscopy (TPUWFM) could be a viable option to the long scan times required for imaging while using TPULSM. To determine the maximum lateral and axial resolution obtainable with this technique, the blood vessels inside the brain of a mouse was chosen to be imaged. Blood vessels were clearly observed over a depth of 100 µm (Figure 4.4) with an axial resolution with which we could differentiate the blood vessels present at various depths. The skull bone was thinned by 100 µm to reduce the scatter of light by bone tissue which otherwise would reduce the resolution obtained for an image. The axial resolution obtained enables us to differentiate blood vessels present at different depths (Figure 4.4 A-I) and lateral resolution shows the clear structure of the blood vessels separated by just a few micrometers. This helps us in observing intertwined blood vessels separately from each other as seen in Figure 4.4 E-F. The image showing the projection of all the blood vessels images over 100 µm in the axial direction can be seen in Figure C.1. This is first demonstration of optical sectioning over a depth of 100 µm in *in-vivo* studies using Ln^{3+}-doped nanocrystals.

When imaging deeper than 150 µm in the axial direction, the images obtained were blurred and a poor signal to noise ratio (data not shown) was obtained. This is due to absorption and scatter of the excited light that results in the effective reduction of excitation power density ultimately bringing down the number of photons released per NC. A CCD camera with 50 to 60% QE at 800 nm coupled with an increase in power density might help in at least improving the poor signal to noise ratio beyond 150 µm.

The resolution obtained is rather poor when compared to TPULSM, but the time taken to image these blood vessels are just over a minute. With tissues that do not scatter as much as the brain the axial and lateral resolution obtained would clearly be better.

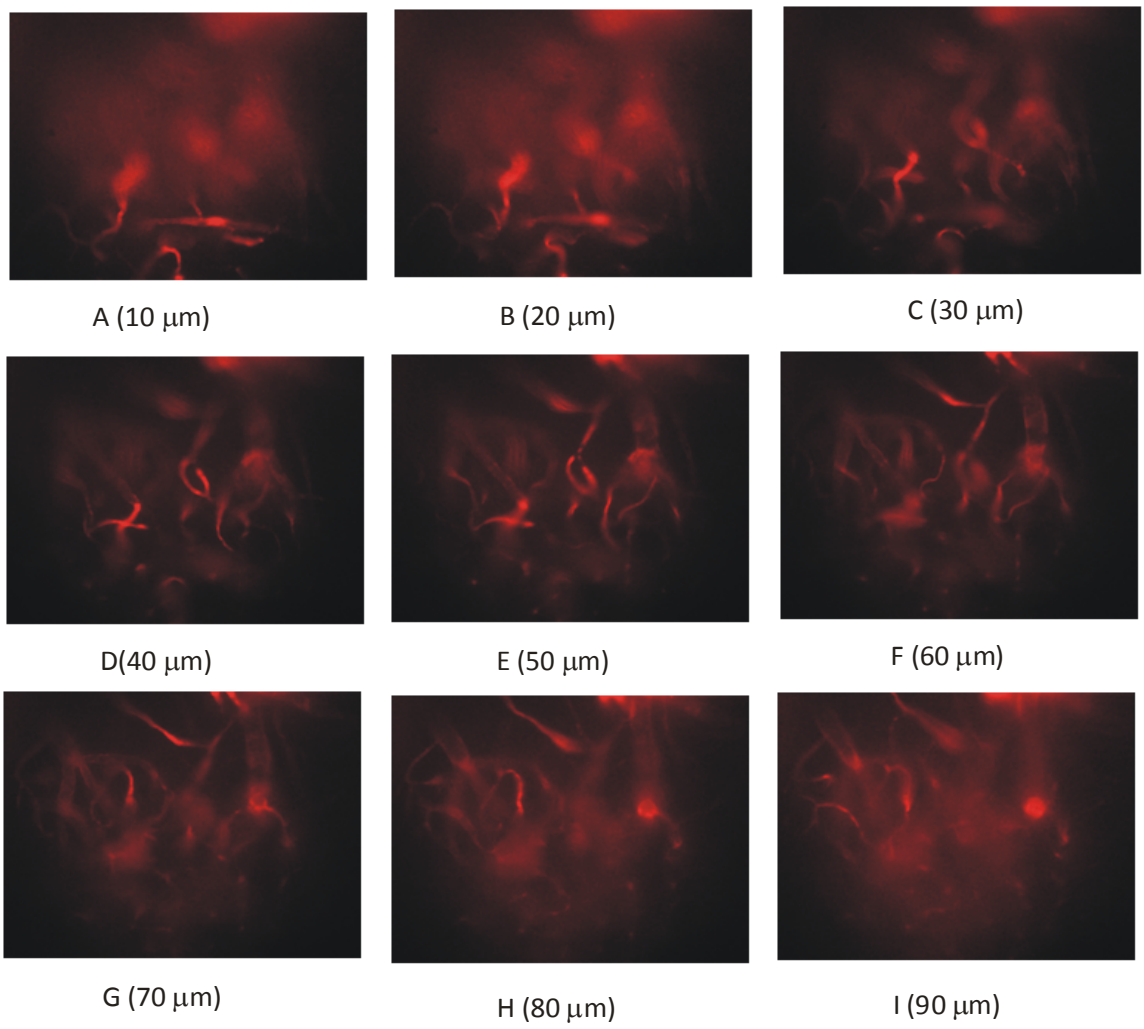

Figure 4.4. (A-I) *In-vivo* images of blood capillaries obtained at different depths inside the brain of a mouse after skull thinning using TPUWFM. The images were taken at 5 W/cm^2 with an exposure of 10 s at a gain of 34.7. The area of the image is 696x520 pixels. A 2x2 on-chip binning was performed. An Olympus 40 X 0.8 NA water lens was used for imaging the capillaries. 800 nm emission upon 980 nm excitation from core/shell/shell;$NaYF_4$:Yb(20%) :Tm(2%)/$NaYF_4$:Yb(20%):Tm(2%)/$NaYF_4$ nanocrystals were used for imaging. These images are false colored.

The relative improvement in the lateral resolution for 800 nm versus 540 nm emission in a scattering media was evaluated by overlaying a 300 or 600 μm thick agar-milk gel upon a cuvette filled with nanocrystals emitting either 800 or 540 nm light. The lateral resolution with no agar-milk gel clearly shows the edge of the cuvette for both 540 and 800 nm emissions (Figure 4.5 A-B). At 300 μm depth the lateral resolution of image obtained using 800 nm clearly shows the edge of the cuvette whereas the image for 540 nm is significantly blurred (Figure 4.5 C-D). This is attributed to the fact that 800 nm scatters less than 540 nm in the agar-milk phantom. For the 800 nm emission, the lateral resolution for the image obtained at a depth of 600 μm did not clearly show the edge of the cuvette (Figure 4.5 E-F). The blurred image appears similar to the one we observed using the 540 nm emission at a depth of 300 μm. The intensity profile for the cuvettes with no agar-milk gel shows a sharp decrease for both the 800 and 540 nm emission (Figure 4.5 G).

For the 300 and 600 μm agar-milk thickness the intensity profile for the 800 nm emission indicates a much sharper decrease in intensity than the 540 nm emission (Figure 4.6 A-C). This substantiates the observation from the images (Figure 4.5 A-F) that the background and cuvette's edge can easily be differentiated for the 800 nm emission in comparison with the green emission. Even though the time taken to image is short, the drawback is that the lateral resolution from TPUWFM is lower than that obtainable with TPULSM. When upconverting $NaYF_4$ nanocrystals are used as the imaging agents in TPUWFM whole body and tumor imaging are feasible. This technique could also help us reach a depth of ~ 300 to 400 μm to determine the size of a tumor. The distinct advantage

of using a wide field microscopy is that a low power density (5 W/cm^2) still provides an excellent signal to noise ratio which aids in imaging the animal continuously for a few minutes without being phototoxic to the tissue.

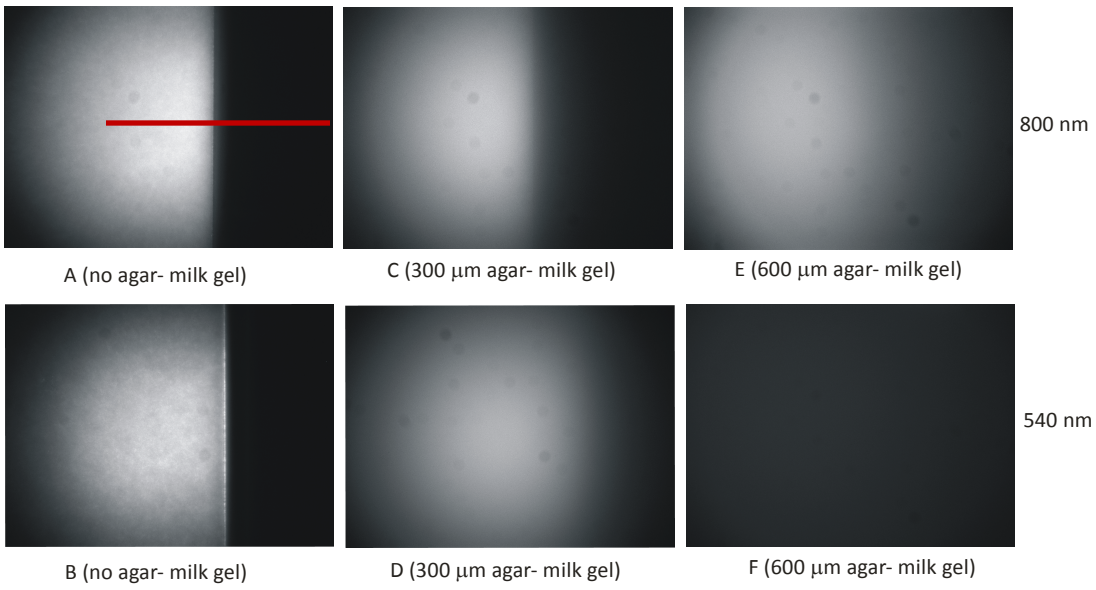

Figure 4.5. Resolution of the edge of a cuvette (A-F) imaged under agar-milk mixtures of different thickness. Duration of exposures; (A) 500 ms (B) 2 sec (C) 900 ms (D) 5 sec, (E) 8 sec (F) 20 sec. The area of each image is 1392/1040 pixels. A 1x1 on-chip binning was performed. Excitation was done at a power density of 30 W/cm^2 from a 980 nm CW laser, with 10% gain of the CCD camera. An Olympus 40X 0.8 NA water dipping lens was used for imaging.

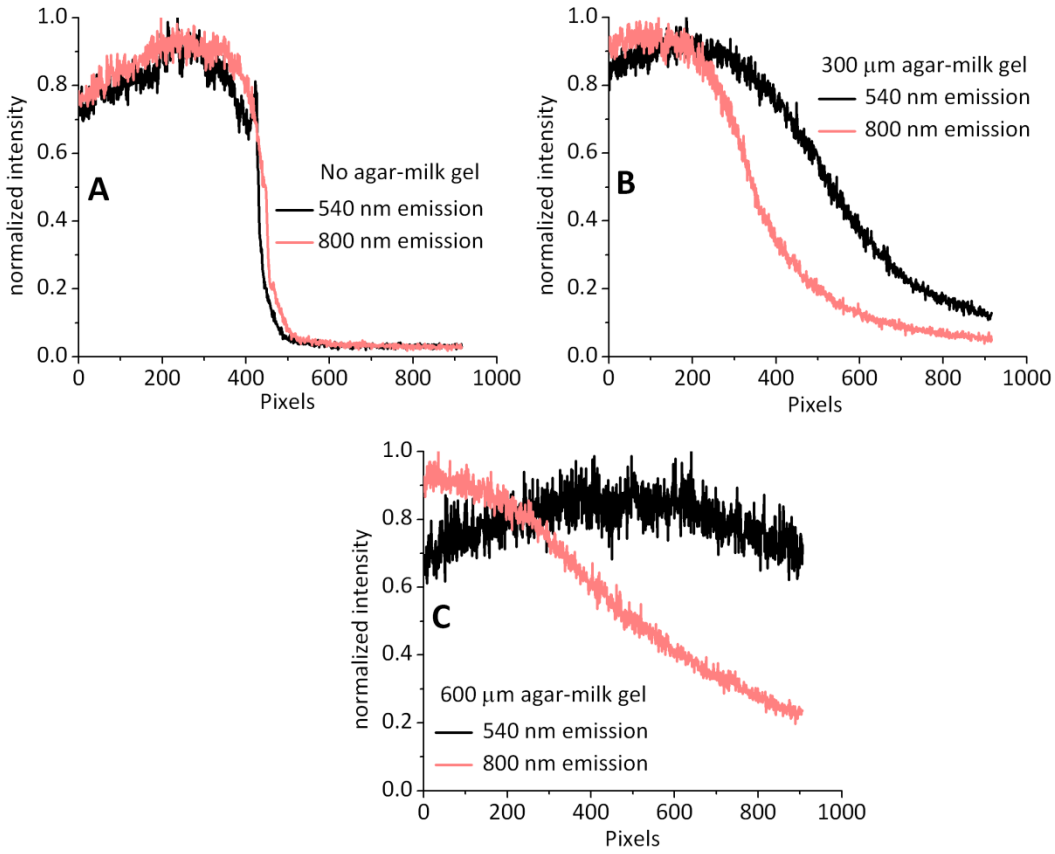

Figure 4.6. (G-I) Intensity profiles of 800 and 540 nm emissions depict the decrease in the sharpness of the edge of the cuvette with increasing agar-milk gel thickness. The intensity profiles were drawn by taking the intensity across the cuvette as indicated in panel A.

4.2.3 Imaging of LN-CaP cells using two-photon upconversion wide field microscopy (TPUWFM)

To demonstrate the utility of TPUWFM in imaging cells, the UCNPs were incubated with human prostate cancer cells (LNCaP). The uptake of the UCNPs by the cancer cells was examined with a Leica compound epi-fluorescence microscope after multiple PBS

washes to remove UCNPs that had not been internalized. Cells were incubated in DAPI, a nuclear fluorescent probe, and the cover slip with the live cells was transferred to a glass slide before mounting on the microscope (Figure 4.7 A). Clearly visible, upconverted green emission was observed from the cells with 980 nm excitation. In Figure 4.7 B we can easily identify four cells. The upconverted emission was observed predominantly as granules in the cytoplasm, which is most clear in overlayed images of DAPI emission (blue nucleus stain, Figure 4.7 C) and the UCNPs (green, Figure 4.7 D). A lower magnification image shows a large proportion of the LNCaP cells labeled with UCNPs (Figure C.2) indicating the effectiveness of the cellular uptake of these particles. The inhomogeneous green intensity observed in cells can be attributed to the uneven uptake of the nanoparticles by the cells. It should be possible to attach tumor specific antibodies to the crosslinked PMAO-PEG-BHMT coated UNCPs, as they have multiple carboxylic acid moieties on their surface, which will be explored for targeted delivery.

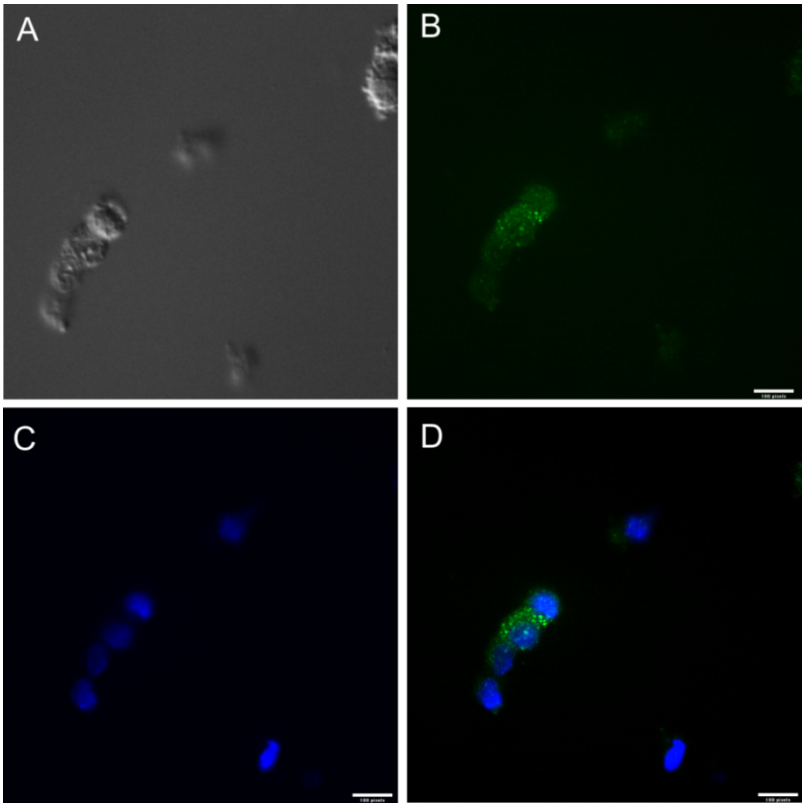

Figure 4.7. LNCaP cell imaging (A) bright field Differential Interference Contrast image; (B) the same field with 980 nm excitation; (C) DAPI excitation (nucleus stain); and (D) overlay of upconverted emission and DAPI. Core/shell;$NaYF_4$:Yb(20%):Er(2%)/$NaYF_4$ coated with PMAO-PEG-BHMT was used for imaging the cells.

4.3 Conclusions

The advantages and disadvantages of using Ln^{3+}-doped $NaYF_4$ nanocrystals as imaging agents with *two-photon upconversion laser scanning microscopy* (TPULSM) and *two-photon upconversion wide field microscopy* (TPUWFM) techniques have been described in this chapter in detail. It was determined that imaging is possible up to a depth of 600 μm in an artificial phantom to discern the edge of the cuvette using the 800 nm emission

from Tm^{3+}. However, using Ln^{3+}-doped nanocrystals as imaging agent in TPULSM becomes impractical for scanning applications like live cell imaging, Ca^{2+} detection, measuring blood flow rates due to the very slow scan speeds (250 to 500 µs/pixel) required because of the long lifetimes and poor quantum yield of the upconverting nanocrystals. The scan speed could possibly be improved by using a multifocal two-photon microscopy technique, but the resolution will strictly depend on the ability of the camera to resolve it in the spatial direction. To overcome this problem we employed TPUWFM and found that we could image up to a depth of ~ 400 µm using the 800 nm emission with the ability to differentiate the edge of the cuvette. As a result of the good penetration of the 980 nm light through the scattering phantom and the reduced scattering of the emitted 800 nm, these upconverting nanocrystals can be used to image small biological structures *twice as deep* as the fluorophores that emit in the visible spectrum. Optical sectioning was also demonstrated for the first time with Tm^{3+}, Yb^{3+} codoped $NaYF_4$ nanocrystals while imaging blood vessels inside the brain of a mouse over a depth of 100 µm.

In addition, the power density required to image is at such a low level (~ 5 W/cm^2) that we can image for an extended time period because of the absence of phototoxicity and photobleaching. When these upconverting nanocrystals are incubated with cells they get internalized easily, which they can easily be imaged using TPUWFM. From the above results it can be concluded that these lanthanide doped nanocrystals are not suitable for deep tissue imaging due to their poor penetration depth in tissues like brain. Chapter 5 will explain the characterization of the lanthanide doped nanocrystals using energy-

dependent X-ray photoelectron spectroscopy to understand their fundamental structure and aid in improving their current optical properties. To overcome the obstacles faced while using lanthanides, an attractive alternative is to use lead-based quantum dots as a bioimaging agent. This is dealt in chapter 6.

4.4 Experimental Details

The synthesis and surface modification of the lanthanide doped $NaYF_4$ nanocrystals has been explained in detail in chapter 3.

4.4.1 Imaging of a mouse

The mouse was partially anaesthetized with isofluorine, then fully anaesthetized with urethane (1.5g/Kg) injected intraperitoneally. For TWUWFM nanocrystals dispersed in distilled water were injected through the tail vein. In case of TPULSM, the blood was purged from the body by perfusing TRIS buffered saline via the left ventricle. Then 2 ml of 1 wt% nanocrystal dispersion in phosphate buffered saline was injected into the ventricle to fill the vasculature of the lungs, liver (data not shown), and the brain.

4.4.2 Two-photon upconversion laser scanning microscopy (TPULSM)

A 980 nm JDS Uniphase laser diode (device- 63-0042) coupled to a 105 μm core fibre was used as the laser source for imaging. Imaging was performed on a custom home built two-photon laser scanning microscope with an Olympus 40X 0.8 NA water lens being used to focus the light onto the mouse. Scanning was performed with an x-y galvanometer pair (Cambridge Technology, model 6010) controlled by home-built electronics and custom software written in Igor™ by J.Boyd. nanocrystals were coated

onto a glass slide and scanned at various speeds ranging from 2 to 500 µs/pixel in the lateral plane (x-y axis). The measurements for scanning the glass slides were carried out at 100 W/cm^2 power density. To image mouse lung tissue, the scan speed was 200 µs/pixel in the lateral plane (x-y axis) with 25 µm step size in the axial direction (z axis). A 40X 0.8 NA Olympus water dipping lens was used for imaging the nanocrystals and solutions. The emitted light was collected using a H5783-01 Hamamatsu detector. The power density was calculated by measuring the power at the front of the objective lens assuming a focused spot of 1 µm radius.

4.4.3 Two-photon upconversion wide field microscopy (TPUWFM)

Imaging was done using the Olympus BX51W1 microscope with the excitation source being 980 nm JDS Uniphase laser diode (device- 63-0042) coupled to a 105 µm core fibre. An Olympus 40X 0.8 NA water lens was used to focus the excitation light onto the brain of a mouse and cuvette. The fluorescence light was collected using EXi Blue Fluorescence Microscopy Camera (EXI-BLU-R-F-M-14-C). The emitted NIR (800 nm) and green light were collected using 800/50 nm and 540/80 nm band pass filters (Chroma Technologies), respectively. The power density was calculated by measuring the power at the front of the objective lens and the focal area.

4.4.4 Imaging with agar-milk gel as an artificial phantom to mimic a rodent's brain

Agar solution was prepared by mixing 1.5 g of agar with distilled water (45 ml) and cooked in a microwave until a clear solution is obtained. Care should be taken that so the

solution does not boil. Skimmed milk powder weighing ~ 6.5 g was mixed with distilled water (47 ml) and stirred well to get homogenized solution. The milk was then mixed with the agar solution and poured into petridish. The solution was cooled to room temperature by which the solution solidified into a gel. For imaging with TPULSM, a cuvette ~ 50 µm size was filled with nanocrystal dispersion (core/shell/shell;$NaYF_4$:Yb(20%):Tm(2%)/$NaYF_4$:Yb(20%):Tm(2%)/$NaYF_4$). An agar-milk gel shaped as a wedge was kept over the cuvette in such a way that three fourths of the cuvette was covered. All images were scanned at a speed of 25 µs/pixel and an average of 3 frames was done to obtain each image. Scanning was done in the x axis (horizontal plane) along the increasing thickness of the wedge shaped agar-milk gel starting from the part of the cuvette which was not covered with agar-milk gel. Due to scattering of agar-milk gel the intensity profiles show a shift in the peak position of the luminescence curve (Fig 4G). For comparison purposes we shifted all the curves to the right in Fig 4H with all the peak intensities were normalized for comparison purposes. Images of the cuvette with the wedge shaped agar-milk gel over it were obtained to determine the depth which can be reached without the loss of the resolution of the image of the cuvette's edge.

In case of TPUWFM, two 50 µm cuvettes were taken and one was filled with Yb^{3+}/Er^{3+} doped $NaYF_4$ nanocrystals and other one filled with Yb^{3+}/Tm^{3+} doped $NaYF_4$ nanocrystals. Images of the cuvette were obtained with no agar on it followed by increasing thickness of agar-milk gel from 300 µm to 600 µm over the cuvette. Slices of agar- milk gel with 300 and 600 µm thickness were obtained by slicing a 4 mm thick agar-milk gel slab.

4.4.5 Cell culture and biolabeling using $NaYF_4$/$NaYF_4$:Yb(20%):Er(2%) core/shell nanocrystals

Human Prostate cancer cells (LNCaP) were grown in tissue culture treated dish (100 mm x 20 mm) with 10 % fetal bovine serum-supplemented RPMI-1640 growth medium. The cells were detached at 60-70 % confluency and seeded on a 22 x 22 mm^2 glass cover slip placed in a six-well culture plate. The cells were grown for 3 days and then carefully washed with PBS multiple times to remove any unbound cells and debris. To the washed cells, growth medium (2 ml) with crosslinked nanoparticles (core/shell $NaYF_4$: 20% Yb^{3+}, 2% Er^{3+}/$NaYF_4$- PMAO-PEG-BHMT, ~ 200 µl, sterile filtered from TBS) was added and incubated at 37 °C for 2 h. The cells were carefully washed with PBS multiple times to remove UCNPs that had not been internalized and the cover slip inverted and mounted onto a glass slide for imaging.

4.4.6 Cell imaging by two-photon upconversion wide field microscopy

Imaging of the nanoparticle uptake by LNCaP cells was done using a Leica DM 6000B microscope with the excitation at 980 nm using a JDS Uniphase laser diode (device type 63-00342) coupled to a 105 µm core fiber. A Leica 50X 0.5 NA long working distance lens as objective was used to image the cells. The power density was ~ 5 W/cm^2 in front of the lens. The green fluorescence from the UCNPs was collected using a Hamamatu digital camera C47420-80-12AG. A band pass filter (527/30 nm) from Leica was employed to filter the scattered excitation light. The nucleus of the live cells were stained with 4',6-diamidino-2-phenylindole (DAPI) before imaging. Images of cells using DAPI were obtained with a 40X 0.75 NA Leica lens, with excitation (360/40 nm) and emission

band (470/40 nm) pass filters (Leica). The DAPI images were obtained with 358 nm (UV light) excitation and the emission was collected at 460 nm (blue light).

Chapter 5. Are all Yttriums Ions Present in the Lanthanide Nanocrystals the Same? Probing the Nanocrystals Using Energy- Dependent and Resonant XPS

The core/shell nanocrystals used for the experiments in this chapter were synthesized by Noah Johnson.

5.1 Introduction

Nanocrystals in general have attracted wide attention in a large number of applications ranging from electronics to contrast agents in medicine due to their unique properties at the molecular level.[3,89] A fundamental understanding of their structure and chemical speciation will enable researchers to tune the synthesis of nanocrystals with respect to their physical properties depending on the required application. This will also further the understanding of the materials at the nanoscopic level. A large number of studies have been done on quantum dots in particular to understand their fundamental properties. For instance, scientists have been able to synthesize core/shell CdSe/ZnS quantum dots with a near-unity quantum yield of photoluminescence.[77] The growth, structure, and chemical speciation of the quantum dot nanocrystals have extensively been studied using various techniques such as XRD, TEM, SEM, X-ray photoelectron spectroscopy (XPS), and EDS.[162,194-195] Of all the aforementioned techniques, XPS is the technique that can provide detailed structural *and* chemical information on the nanocrystals.[196-198] This has been employed to identify elements, calculate the composition of elements and their different oxidation states.[199] The advantage and at the same time limitation of this

technique is that it can probe only the surface of the sample.[200] In such cases, angle-resolved XPS is a versatile tool to study samples with a depth profiling up to 6 to 7 nanometers. By increasing the angle with reference to the normal of the sample, the distance necessary to travel for an electron from a certain depth will be reduced. By changing the angle, the structure and the chemical composition of the sample at different depths can be studied. This technique utilizes the inelastic mean-free path (IMFP) of the electron to study the sample at different depths.[200] However, this technique cannot be used for spherical nanocrystals as the angle dependence will not change.

To circumvent this problem and analyze spherical nanocrystals, Borchert *et al.* employed energy-dependent XPS to provide concrete evidence for a core/shell structure of CdSe/ZnS quantum dot.[196] The advantage of using energy-dependent XPS is that the IMFP depends on the kinetic energy of the photoelectrons. The IMFP of the electron always remains the same as it is an inherent property of the interaction of the electron with the material it has to escape from.[200] When a tunable energy source like synchrotron energy is employed, the kinetic energy of the electrons can be changed. As the excitation photon energy is increased the kinetic energy of the emitted photoelectrons is also increased. To susbtantiate a core/shell structure the ratio of the core and the shell elements at different excitation energies are calculated. When a graph is drawn between the kinetic energies and the ratio of the elements it should look like S-shaped curve.[99,201-203] When the kinetic energy is low, the electrons from the surface will escape easily and the intensity will be higher when compared to the electrons escaping from the core. As the excitation energy is increased, the kinetic energy of the electrons from the core will

increase and the ratio between the shell and core will decrease eventually remaining the same beyond the IMFP limit. Hence, it is a powerful tool to analyze the core/shell structure. Our group recently analyzed the core/shell structure of PbSe/CdSe quantum dots made through a cation exchange process.[99] As mentioned in the introduction this process is different from the traditional growth process of a shell over the core quantum dots. Therefore it was imperative to understand whether the cation exchange process really leads to a core/shell structure. When these quantum dots were analyzed using energy-dependent XPS with high resolution scans, the results show that there is a sharp interface between core and the shell. In addition to this, when the core Pbse QDs were analyzed, the chemical speciation of Pb^{2+} on the surface of the PbSe quantum dot is different from the Pb^{2+} inside the QD. These surface Pb^{2+} ions are different because they are bound to oleates or trioctylphosphine (TOP) present on the surface as coordinating ligands.

Although there have been extensive studies on quantum dots, there are very few reports on the lanthanide nanocrystals which have attracted attention due to their non-bleaching, non-blinking, and optical properties which could be exploited for various applications. Our group was first to use energy-dependent XPS to provide evidence that the core/shell structure of $NaYF_4/NaGdF_4$ lanthanide nanocrystals made through an organic route is indeed true.[202] This study was necessary because the core/shell GdF_3/LaF_3 and LaF_3/GdF_3 nanocrystals made through an aqueous route did not result in a core/shell structure. Instead a gradient structure was observed and in some cases, like NdF_3/LaF_3, an alloy structure was observed.[201]

As seen in the previous chapters lanthanide elements are generally doped in a low-phonon energy matrix for various applications. The general assumption in the field of lanthanides is that the lanthanide dopant elements in a matrix are isotropically distributed throughout the matrix. This is because of the fact that the lanthanide ions have similar properties. This notion was not actually correct due the fact that with, $NaGdF_4$:Nd(20%), $NaGdF_4$:Tb(20%), and $NaGdF_4$:Y(20%):Tb(5%) nanocrystals, the dopant ions are not evenly distributed inside the matrix. With Nd^{3+} as a dopant, the nanocrystals had a core/shell structure with Gd^{3+} ions inside and the Nd^{3+} ions on the surface. A similar core/shell structure was observed for $NaGdF_4$:Tb(20%) nanocrystals with Tb^{3+} ions in the core and Gd^{3+} ions in the shell. In case of $NaGdF_4$ nanocrystals doped with Y^{3+} and Tb^{3+} ions, a gradient structure was observed which is different from an expected alloy structure. All three nanocrystals exhibit a different structure indicating that the lanthanide distribution need not be isotropic.[203]

Hence, it would be interesting to know the structure and chemical speciation of $NaYF_4$ doped with Yb^{3+} and Tm^{3+} ions which has shown potential as a bioimaging agent. Understanding the structure and chemical speciation of these nanocrystals will hopefully pave the way for synthesizing nanocrystals which are more efficient than the current ones. As observed in the previous chapter the optical properties of the lanthanides have to be improved to make them viable for imaging deeper inside tissue. This is the one of the few materials for which the excitation and the emission lie in the region where the biological tissue is most transparent to light. Therefore, the primary goal was to understand the dopant distribution of Yb^{3+} and Tm^{3+} ions in the $NaYF_4$ matrix. The goal

could not be achieved with the standard energy-dependent XPS due to the fact that no signal was observed for the lanthanide ions. However, some interesting observations on the chemical speciation of Y^{3+} ions were made. The yttrium ions generally show a single 3d doublet for the 3d electrons at a binding energy of 160 eV. In this chapter a second doublet is observed. This new doublet is attributed to the different chemical speciation of the yttruims on the surface of the nanocrystals when compared to the ones inside the nanocrystals. This phenomenon is observed for nanocrystals of size greater than 10 nm. It seems like the surface properties of the nanocrystals for sizes greater than 10 nm are different from the overall nanocrystal.

At this point it is not completely clear why this differentiation is observed. In addition to the above, photoelectrons were observed from the 4d electrons of Tm^{3+} and Yb^{3+} ions when they were grown as a separate shell over the $NaYF_4$ nanocrystals. However, as mentioned above, no signal was observed when these elements were doped in the $NaYF_4$ nanocrystals. In order to solve the problem, *resonant* XPS was employed to obtain signals for the 4d electrons of Yb^{3+} and Tm^{3+} ions. The primary reason to employ this technique is because of the fact that it enhances the photoelectron signal from the 4d electrons of the lanthanides. Preliminary investigation has revealed that the lanthanides exhibit multiplet features for the photoelectron from the 4d electrons (excitation in the 3d absorption range) under resonance conditions for Yb^{3+} and Tm^{3+} ions.

5.2 Results and Discussion

5.2.1 Energy-dependent X-ray photoelectron spectroscopy on doped and undoped $NaYF_4$ nanocrystals

The XPS spectra of $NaYF_4$, $NaYF_4$:Yb(20%):Tm(5%), $NaYF_4$:Tm(20%), $NaYF_4$:Yb(20%) are shown below. The 3d peaks from Y^{3+}, the 4d peaks of Yb^{3+}, and Tm^{3+} ions are monitored (Figure 5.1). All four samples were drop-casted on a thin gold foil. The photoelectron peaks from the 4f electrons of gold are used as the reference peaks (Figure 5.2). Using gold as the reference the peak positions for yttrium, thulium and ytterbium were calculated. Yttrium exhibits its typical doublet for the 3d electrons. The ratio between the peak is 2:3 and the peak lies around the binding energy of 165 to 168 eV depending on the reference gold peaks. The peaks around a binding energy 180 eV is also attributed to Y^{3+} ions (Figure 5.1). However the two broad peaks look very similar to the peaks from the 4d electrons of Yb^{3+} ions. Capobianco and coworkers assign this peak to the 4d electrons of the Yb^{3+} ions. These two peaks cannot be from Yb^{3+} ions due to the fact that these are observed not only in $NaYF_4$ nanocrystals doped with Yb^{3+} ions, but also in undoped $NaYF_4$ nanocrystals. This validates that the peaks are not from Yb^{3+} ions but from Y^{3+} ions. Furthermore the two peaks do not match exactly with the peaks reported for ytterbium metal and Yb_2O_3. The reason the 3d peaks from the yttrium ions are investigated because it provides a good signal to noise ratio and the splitting of the 3d orbitals can clearly be observed.

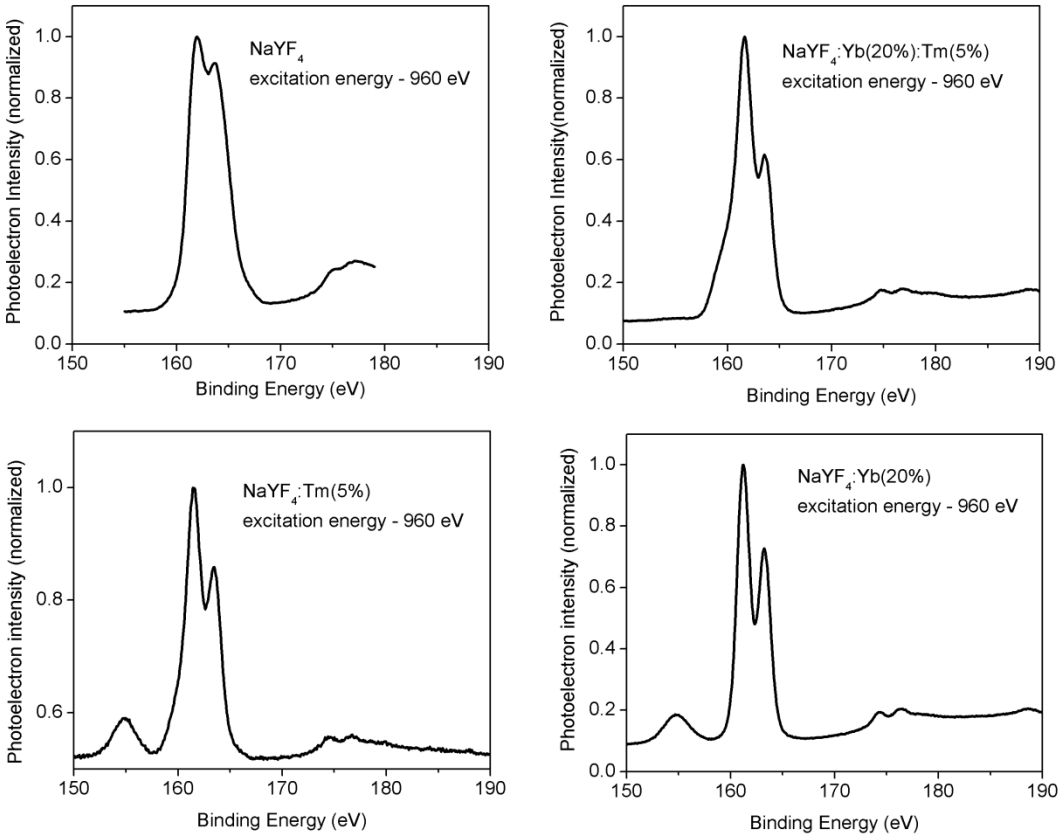

Figure 5.1. XPS spectra of doped and undoped $NaYF_4$ at an excitation energy of 960 eV. The peak around 161 and 163 eV belong to $3d_{5/2}$ and $3d_{3/2}$ of Y^{3+}. The peaks around 155 in the two bottom spectra belong to 2s of silicon. A small shoulder around 159 eV is also observed in the top two spectra and in the bottom left one as well. This is the new doublet peak observed for Y^{3+} ions which is convoluted with the main doublet (161 and 163 eV) observed for Y^{3+} ions.

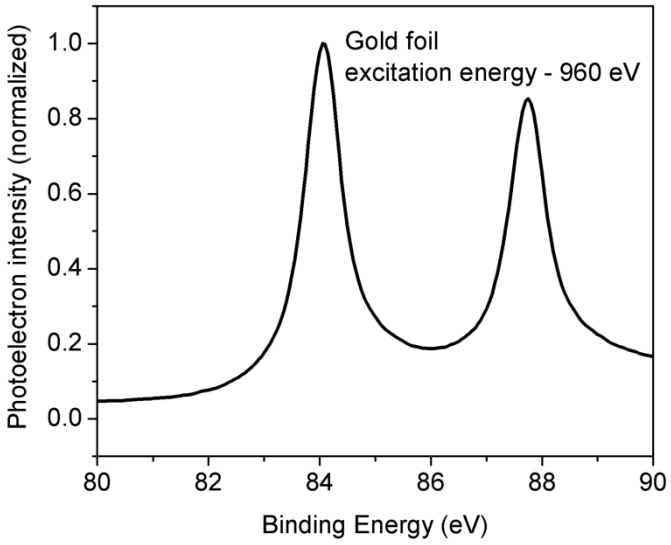

Figure 5.2. XPS spectrum showing the 4f photoelectron peaks of gold. The peaks at 84 and 88 eV belong to $4f_{7/2}$ and $4f_{5/2}$.

In addition to the doublet of the 3d electrons a new peak around 159 eV (lower binding energy when compared to photoelectron peaks of 3d electrons from Y^{3+} ions) was also observed. This new peak is convoluted with the doublet observed for the 3d electrons. The peak width for the doublet is generally around 6 eV. In presence of the new peak the width of the doublet along with the new peak increases to 10 eV. This suggests that the new peak is also a doublet (will be mentioned as new doublet from now on) which is convoluted with the 3d doublet. The interesting thing to note here is that the intensity of this doublet changes with the excitation energy. As the excitation energy is decreased from 960 eV by steps of 60 eV the intensity of the new doublet increases (Figure 5.3). When the intensity of the new doublet increases, the relative peak intensity of the 3d doublet with respect to the new doublet starts decreasing. This strongly suggests that

there is a direct correlation between the intensity of the new doublet and the doublet observed for the 3d electrons. The interesting factor to note here is that the new doublet becomes prominent as the excitation energy is decreased (Figure 5.3). The increase in the intensity at lower excitation energy is fully consistent with the fact that this is due to the surface ions rather than ion inside the nanocrystals. The new doublet is observed with both doped and undoped $NaYF_4$ nanocrystals. All the above reasons point to the fact that the new doublet observed definitely belongs to 3d electrons of the yttrium ions. The new doublet is due to the different chemical speciation of yttrium ions which are present on the surface when compared to the ones inside the nanocrystal. The different chemical speciation could be due to few possibilities: 1) yttriums ions could be surrounded by oleates; 2) presence of surface defects. The new doublet observed is definitely not due to the influence of dopants which is confirmed from the fact that it is observed with undoped $NaYF_4$ nanocrystals as well. Furthermore there are two other possibilities which can be discounted: 1) different sizes of nanocrystals (mixture of big and small due to poor size dispersion); 2) presence of cubic phase nanocrystals along with hexagonal phase. Theoretically both these could provide an extra doublet from the Y^{3+} ions, however the new doublet's ratio with the main 3d doublet would not change with excitation energies.

The new doublet seems to be dependent on the size of the nanocrystals. If the size of the nanocrystal is greater than 10 nm the new doublet is observed. However, it is not completely clear why this differentiation is observed. The other primary evidence to confirm that the new doublet is from the surface ions is by measuring the XPS spectrum for core/shell nanocrystals. When the XPS spectra was measured for the core/shell

$NaYF_4/NaYbF_4$ or $NaYF_4/NaTmF_4$ nanocrystals the new doublet was not observed. A single doublet for Y^{3+} ions was observed in both cases. The general assumption that the chemical speciation of the surface and the bulk ions in the nanocrystals is the same is not true anymore. These results will definitely help in improving the optical properties of the lanthanides when doped in a matrix.

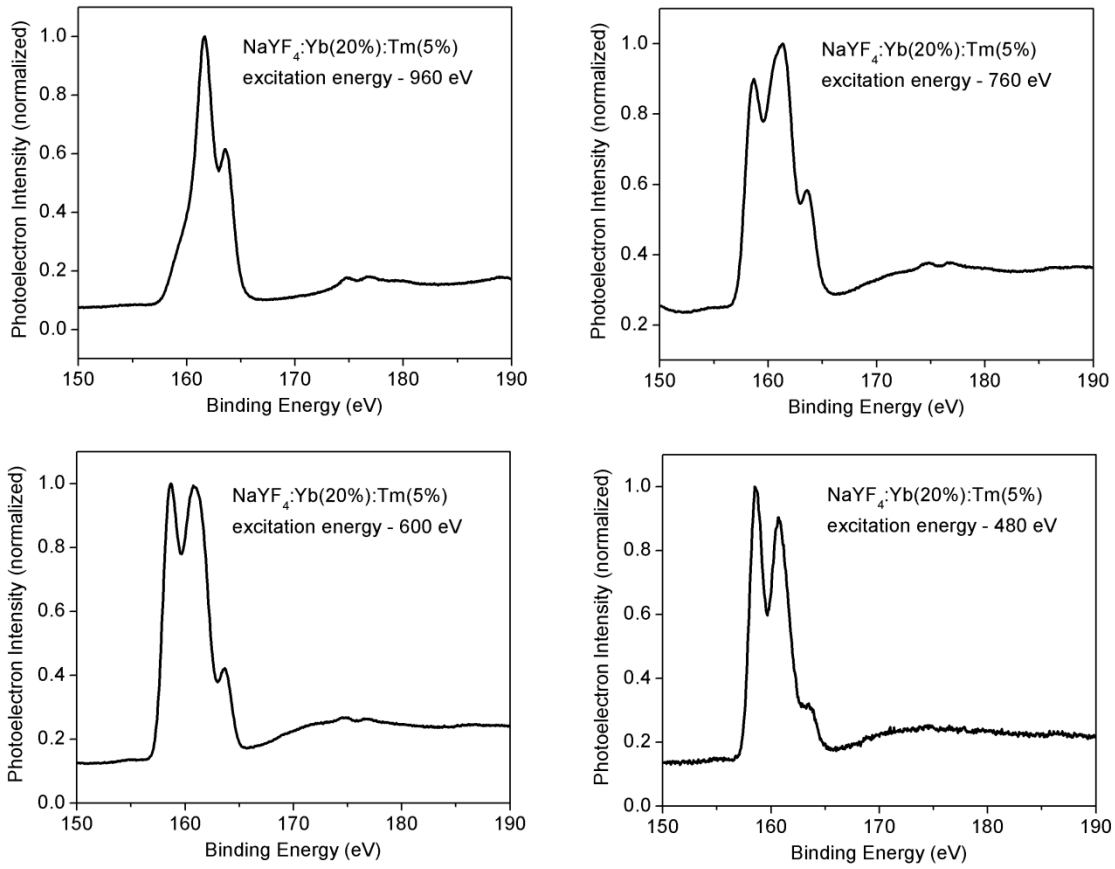

Figure 5.3. Appearance of a new doublet for Y^{3+} ions at lower excitation energies.

One important thing to note is that this study was started with the goal of studying the dopant distribution of lanthanides in the $NaYF_4$ matrix. Surprisingly, no photoelectrons from the 4d orbitals of either Tm^{3+} or Yb^{3+} ions were observed when they were doped in

the $NaYF_4$ matrix (Figure 5.4). This suggests that the lanthanides could be deep inside the nanocrystals making it harder for the photoelectrons to escape from the nanocrystals. The doping level of these lanthanides is not high which could lead to the fact that the number of 4d photoelectrons escaping from the nanocrystals is not high. These could have lead to a poor signal to noise ratio for the photoelectrons escaping from the lanthanides. This is something surprising as our group has recently published two papers on LaF_3 doped with Gd^{3+} or Nd^{3+} ions and $NaGdF_4$ doped with Y^{3+} or Tb^{3+} or Nd^{3+} ions.[201,203] However, a signal for Yb^{3+} and Tm^{3+} was observed when they were grown as a shell over $NaYF_4$ instead of being doped. The peaks observed for Yb^{3+} and Tm^{3+} ions were different from the ones reported before for Yb_2O_3 and Tm_2O_3, respectively. This was confirmed by comparing an undoped $NaYF_4$ with $NaYF_4/NaTmF_4$ core/shell (Figure 5.4). Furthermore the peaks observed for the lanthanide ions were shifted at least by 4 to 5 eV when compared to the reported literature. The Yb^{3+} ions are more electropositive when compared to the ytterbium metal and the Yb^{3+} ions in Yb_2O_3.[199] The reason for Yb^{3+} for being highly electropositive is due to the presence of fluoride ions which are highly electronegative when compared to oxides and just the ytterbium metal. In order to study the dopants inside the $NaYF_4$ matrix a different technique, called resonant XPS, was employed. This will be discussed in the next section.

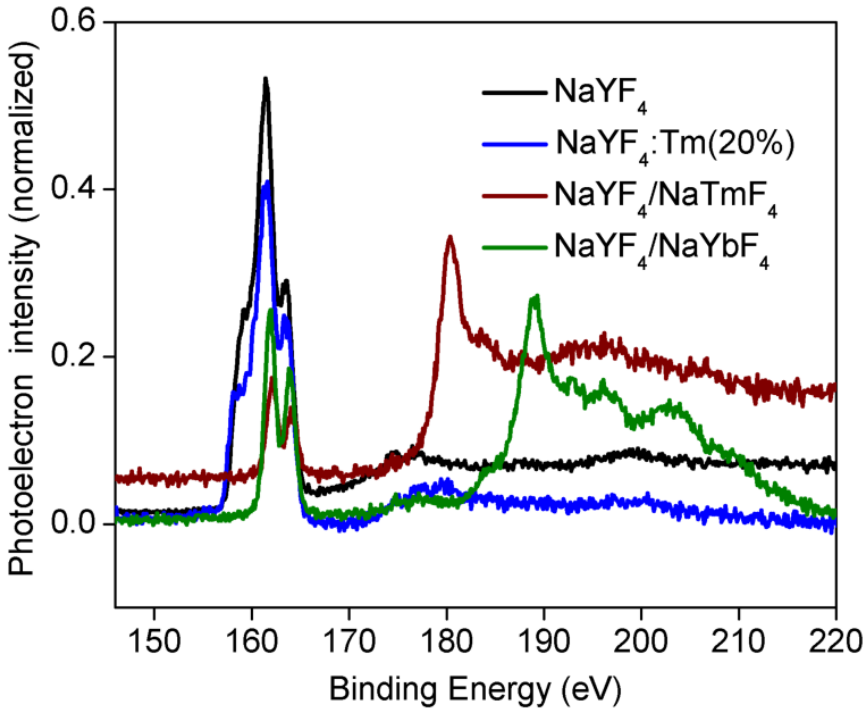

Figure 5.4. XPS spectra of core/shell samples showing signals for Yb^{3+} and Tm^{3+}. The peaks from 181 to 195 eV present in $NaYF_4/NaTmF_4$ belong to Tm^{3+} ions. The peaks from 190 to 204 eV in $NaYF_4/NaYbF_4$ belong to Yb^{3+} ions.

5.2.2 Resonant X-ray photoelectron spectroscopy

As mentioned in the previous section, when the lanthanide ions (Yb^{3+} and Tm^{3+}) were doped in $NaYF_4$ matrix the photoelectrons from the 4d orbitals of the lanthanides were not observed (Figure 5.4). To address this issue, the resonant XPS technique has been employed. Nath *et al.* have observed signals from the 4d electrons of the Tm^{3+} ions using resonant XPS. The authors also mention in the report that the signal to noise ratio is well enhanced from the resonant XPS. Resonant XPS works on the following principle. The inner core electron is excited to an outer shell resulting in the formation of an excited ion

and a core hole. This is followed by the relaxation of an outer shell electron to the core hole giving out its excess energy in the process. The excess energy ejects an electron out from one of the outer shells. The resonant enhancement occurs due to the superposition of a direct electron emission (for instance photoelectrons from 4d orbitals for Tm^{3+} or Yb^{3+}) followed by Auger-like emission (excess energy helping 4d electrons of Tm^{3+} or Yb^{3+} to escape) and Coster-Kronig (CK) decay or a super Coster-Kronig (sCK) decay. An example is illustrated below from thulium ions.

$$3d^{10}\ 4d^{10}\ 4f^{12} + h\nu \longrightarrow 3d^{9}\ 4d^{10}\ 4f^{13*} \longrightarrow 3d^{10}\ 4d^{9}\ 4f^{12} + e^{-1} \text{ Or } 3d^{10}\ 4d^{10}\ 4f^{11} + e^{-}$$

The 3d absorption peaks of Tm^{3+} and Yb^{3+} ions are employed to study their 4d resonant photoelectrons. The absorption spectra for the 3d electrons from Tm^{3+} and Yb^{3+} ions are shown below (Figure 5.5 & Figure 5.6). The thulium ions have three absorption peaks whereas the ytterbium ions have one absorption peak. The thulium ions have two vacancies in their 4d orbitals which could be filled in three possible ways. One of them seem to be the most probable way of filling the orbitals resulting in the strongest absorption at 1465.3 eV (electric-dipole allowed transitions, $\Delta l = \pm 1$) while the other two has low absorptions at 1463.6 & 1468.5 eV. On the other hand ytterbium ions have one vacancy which could be filled in one way resulting in one absorption peak (1524.0 eV). The resonant photoelectrons from the 4d electrons of Yb^{3+} ions were measured between 1520.0 eV to 1528.0 eV (Figure D.1) by increasing the excitation energy by 0.8 eV. The spectra at resonant and non-resonant photon energies are shown in Figure 5.7 to Figure 5.10. The thulium doped $NaYF_4$ was excited with excitation energy of 1455.0 eV followed by the increase in the excitation energy by 0.5 eV till 1472.0 eV (Figure D.2).

The measurements for Tm^{3+} (Figure 5.11 - Figure 5.15) and Yb^{3+} ions encompass both the non-resonant and resonant photoelectrons. The graphs below shows the photoelectron spectra obtained for the 4d electrons of Tm^{3+} ions and Yb^{3+} at different binding energies below and above the absorption energies of their 3d electrons. From the graph it can be observed that there are no photoelectrons coming out from the 4d electrons below and above the 3d absorption edge. Multiples features are observed within the absorption edge. The multiple features observed change with the binding energy suggesting various decay and relaxation processes occurring at the excited state.

The interesting observation is that the resonant photoelectron peaks are slightly different for the lanthanides depending on whether they are doped in a matrix or grown as a shell over the matrix. Before the Auger emission can occur there are several pathways for the core hole to decay. Following are two pathways with which the decay could occur: 1) 3d-4f4f; 2) 3d-4f4d. Following is an example of how to interpret the decay process. For 3d-4f4f decay process, a 3d electron is promoted to the 4f orbital followed by a relaxation (decay) of the electron from the 4f orbital to the fill the core hole in the 3d orbital. When the decay occurs an electron from the 4f orbital is ejected. In the present case with lanthanides the second decay pathway is monitored to look at the 4d resonant photoelectrons. Other than the above decay processes, the Coster-Kronig and super Coster-Kronig decays could as well play a role in the process. However both Coster-Kronig and super Coster-Kronig decays depends on the lifetime of the excited state of the 4f orbitals. From the above observations it is quite clear that the resonant X-ray

photoelectron spectroscopy is a better method than energy-dependent XPS to analyze the lanthanide elements doped in a matrix.

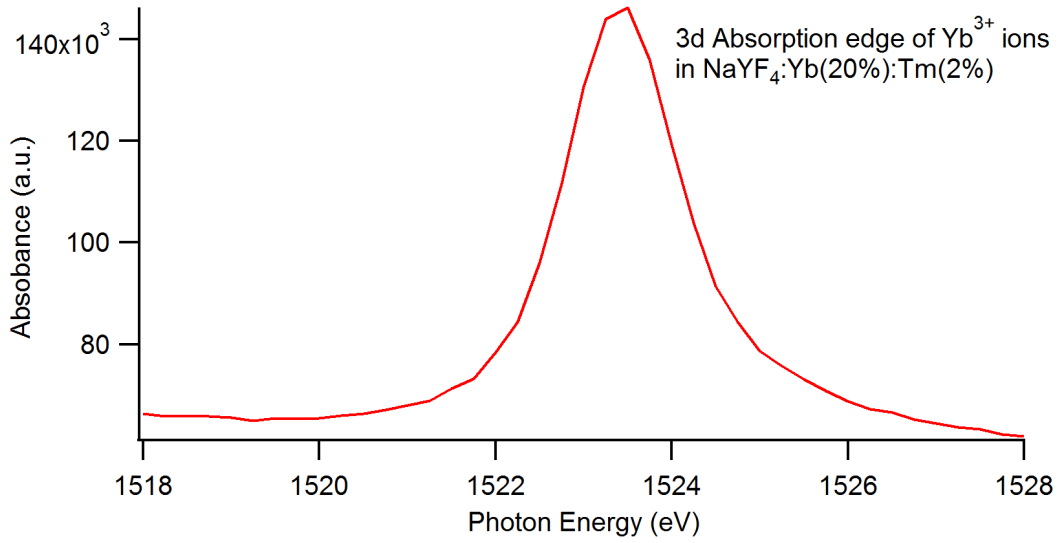

Figure 5.5. Absorption spectrum of Yb^{3+} ions.

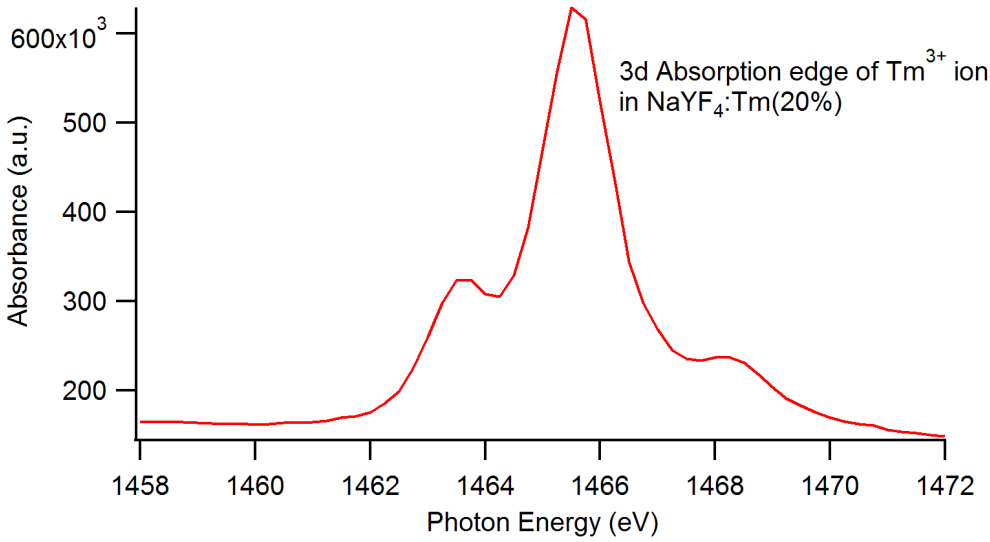

Figure 5.6. Absorption spectrum of Tm^{3+} ions.

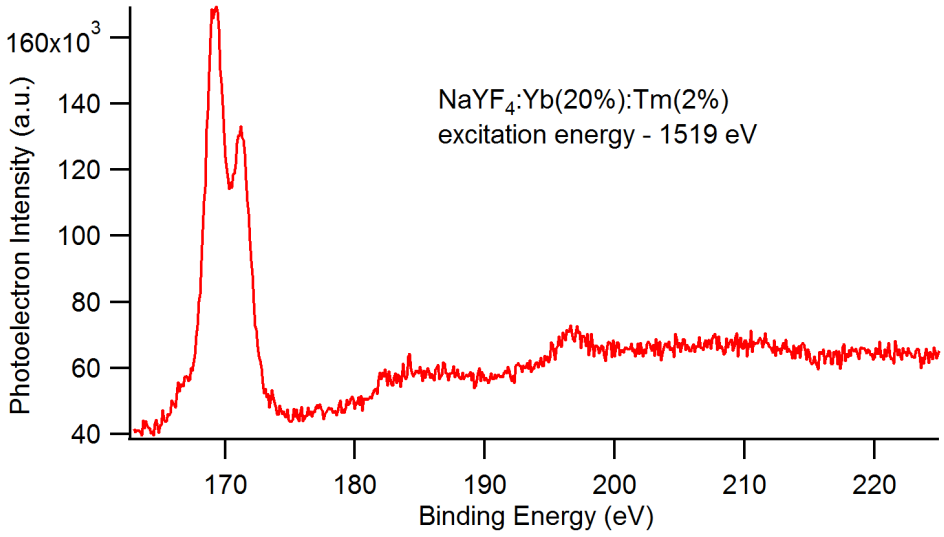

Figure 5.7. Non-resonant XPS spectrum of Yb^{3+} ions. No signal is observed for the 4d photoelectrons of the Yb^{3+} ions.

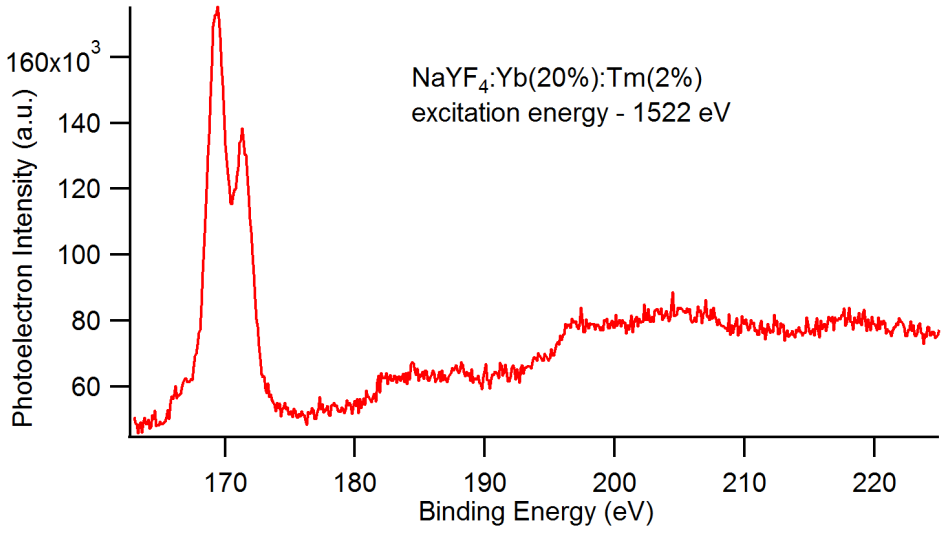

Figure 5.8. Non-resonant XPS spectrum of Yb^{3+} ions. A faint signal is observed around 204 and 218 eV due to the fact that the excitation wavelength lie at the start of the absorption peak of the 3d orbital. This results in the slight resonant enhancement of the photoelectron signal from the 4d electrons.

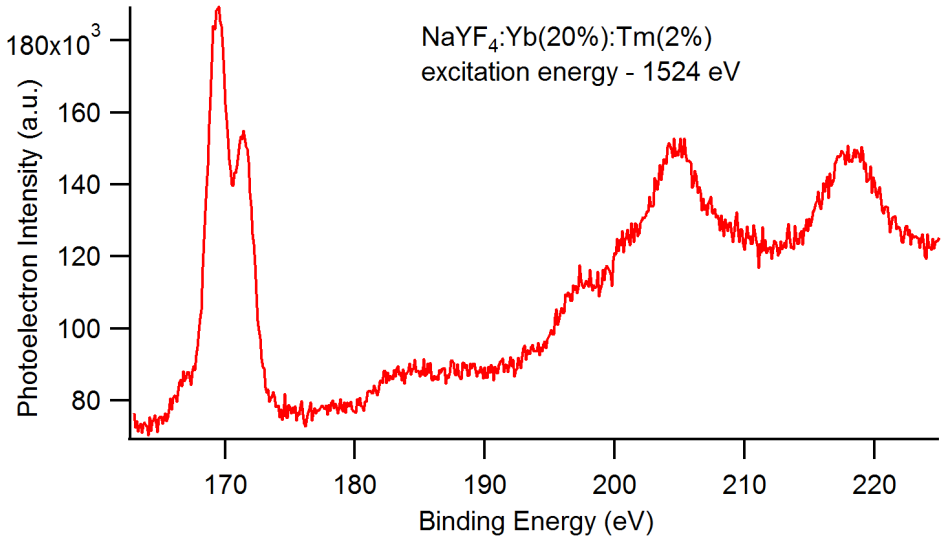

Figure 5.9. Resonant XPS spectrum of Yb^{3+} ions. The peaks around 204 and 218 eV belong to resonant photoelectrons of the 4d orbitals of Yb^{3+} ions.

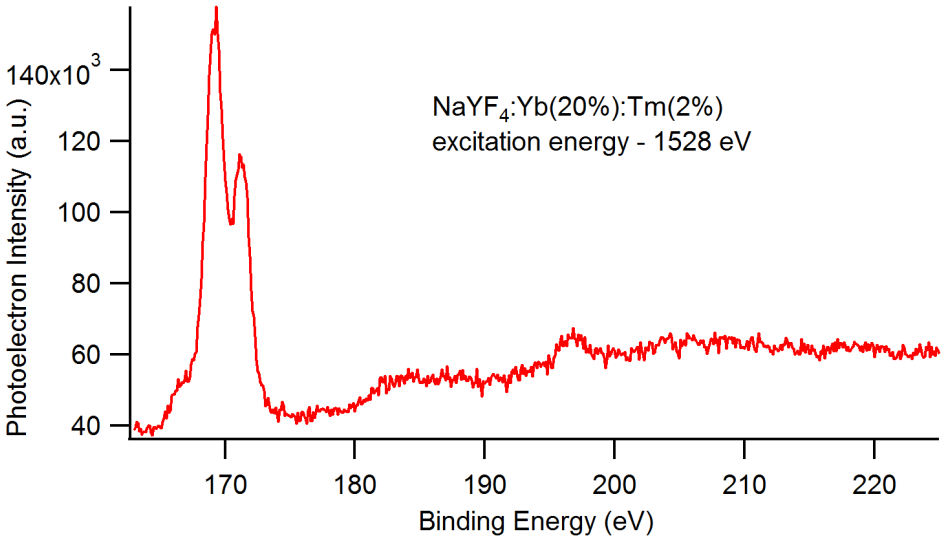

Figure 5.10. Non-resonant spectrum of Yb^{3+} ions. No signal is observed from the 4d photoelectrons of Yb^{3+} ions.

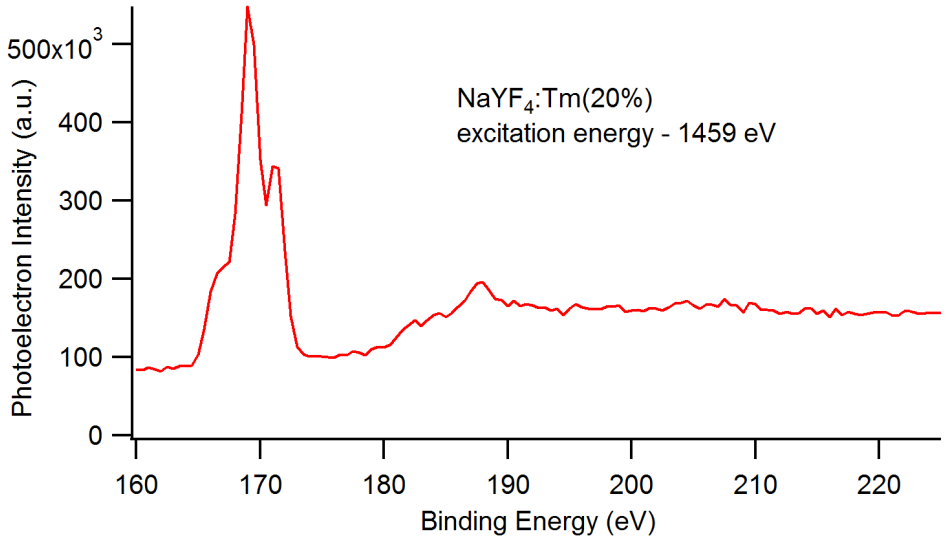

Figure 5.11. Non-resonant XPS spectrum of Tm^{3+} ions. Photoelectron from the 4d electrons were not observed at excitation energies just below the 3d absorption edge.

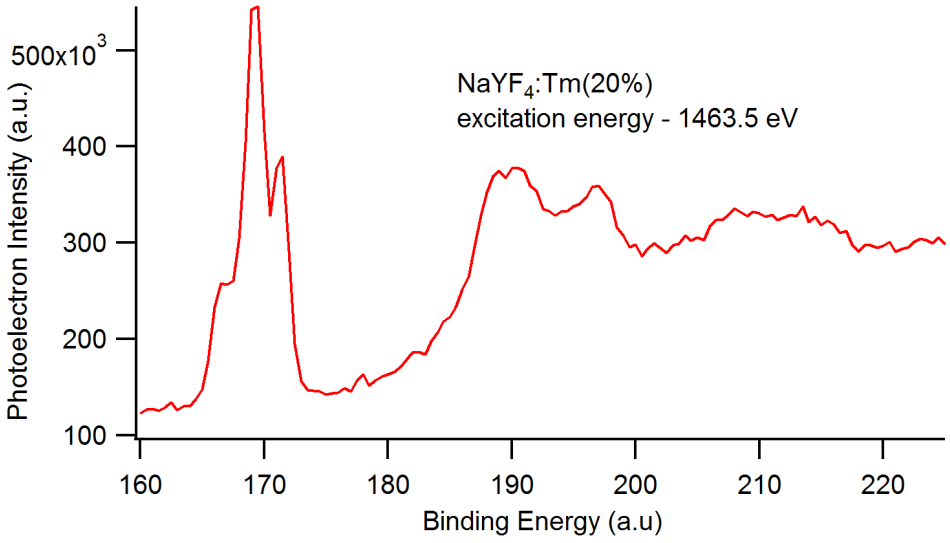

Figure 5.12. Resonant XPS of Tm^{3+} ions. The photoelectrons from the 4d orbitals were observed when the excitation energy matches with the 1st absorption peak of the 3d electrons of Tm^{3+} ions. The peaks around 188 eV, 196 eV and 206 eV belong to the 4d photoelectrons.

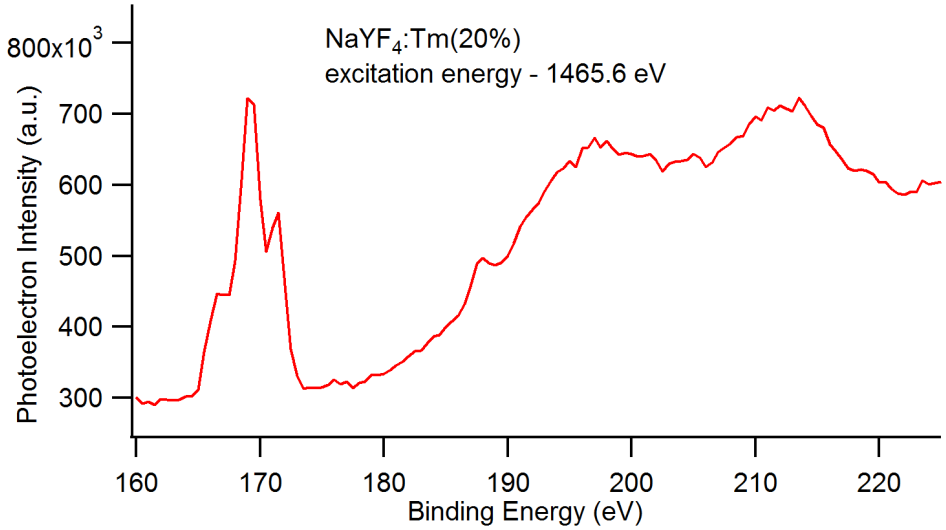

Figure 5.13. Resonant XPS of Tm^{3+} ions. The photoelectron from the 4d orbitals were observed when the excitation energy matches with the 2nd absorption peak of the 3d electrons of Tm^{3+} ions. The peaks around 188 eV, 196 eV and 206 eV belong to the 4d photoelectrons.

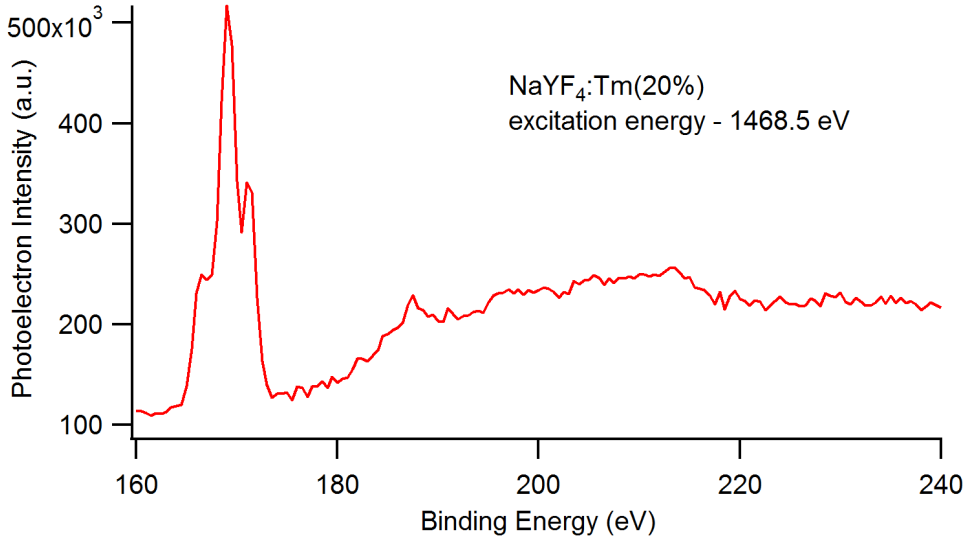

Figure 5.14. Resonant XPS of Tm^{3+} ions. The photoelectron from the 4d orbitals were observed when the excitation energy matches with the 3rd absorption peak of the 3d electrons of Tm^{3+} ions. The peaks around 188 eV, 196 eV and 206 eV belong to the 4d photoelectrons.

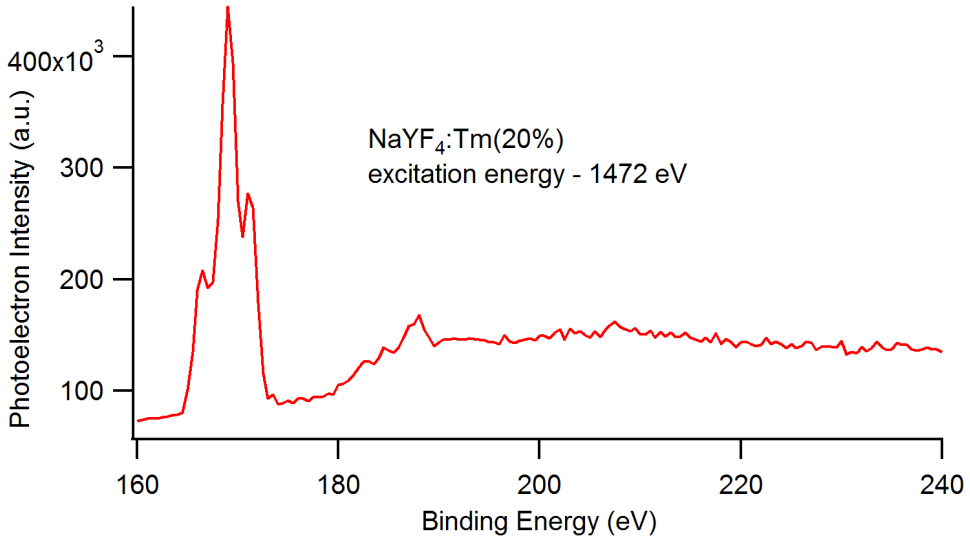

Figure 5.15. Non-resonant XPS spectrum of Tm^{3+} ions. Photoelectrons from the 4d orbitals were not observed at excitation energies just above the 3d absorption edge.

5.3 Conclusions

The energy-dependent XPS study shows that the chemical speciation of the yttrium ions on the surface of the nanocrystals is significantly different from the ones inside the nanocrystals. This was confirmed by the fact that the yttrium ions exhibited a new doublet other than the one usually observed for the photoelectrons from the 3d orbitals. Furthermore this new doublet is observed prominently observed at lower excitation energies and slowly disappeared at high excitation energies. This new feature was observed only with nanocrystals of size larger than 10 nm. With the current data it cannot be concluded why this size dependence behavior is observed. The energy-dependent XPS measurements were also tried to understand the dopant distribution of lanthanides in $NaYF_4$ nanocrystals. However, this could not be achieved because no signal was

observed from the 4d electrons of the lanthanides. This issue was resolved by performing resonant XPS on the 3d absorption edge and by monitoring the 4d photoelectrons. The results from this chapter have the potential to aid in synthesizing lanthanide doped $NaYF_4$ nanocrystals which could be more efficient than the current ones.

5.4 Experimental Details

5.4.1 Synthesis of hexagonal (β–phase) $NaYF_4$ and $NaYF_4$:Yb(20%):Tm(5%) nanocrystals

Yttrium chloride (0.75 millimole), ytterbium chloride (0.20 millimole), thulium chloride (0.05 millimole) were mixed with 6 ml of oleic acid and 15 ml of octadecene and heated to 110 ^{o}C under vacuum and maintained at that temperature for 2 hours to form the oleate complexes. The reaction was brought to room temperature followed by addition of NaOH (0.100 millimole) and NH_4F (0.148 millimole) in 10 ml of methanol. The reaction mixture was stirred for 30 minutes followed by the evaporation of methanol under a stream of argon at 55 - 60 ^{o}C. Once the methanol was completely evaporated, the reaction mixture was heated to 297 ± 2 ^{o}C and maintained at that temperature for 1 hour. Following this the reaction mixture was cooled to room temperature the nanocrystals were precipitated from the reaction mixture using ethanol (100%). The precipitated nanocrystals were dispersed in 3 ml of hexane followed by reprecipitation in ethanol (25 ml). This process was done once more to wash the nanocrystals. The washed nanocrystals were then dried under a stream of air for 20 to 30 sec and dispersed in hexane. For undoped $NaYF_4$ nanocrystals the same procedure was followed.

5.4.2 Synthesis of $NaYF_4/NaYbF_4$ and $NaYF_4/NaTmF_4$ nanocrystals

In order to make core/shell nanocrystals the shell material (cubic nanocrystals) was presynthesized. Ytterbium oxide (1 millimole) was mixed with 20 ml of 50% aqueous trifluoroacetic acid and refluxed at 85 ^{o}C overnight. Following this, the excess trifluoroacetic acid and water was removed by heating the mixture at 65 ^{o}C to obtain a white powder. The white precursor powder was taken in a three necked flask with sodium trifluoroacetate (2 millimoles), oleylamine (6 ml), oleic acid (6 ml), and octadecene (10 ml) and heated at 120 ^{o}C for 45 minutes under vacuum. This was done to remove any excess water, and trifluoroacetic acid. After 45 minutes at 120 ^{o}C under vacuum the reaction mixture was heated to 290 ^{o}C under a flowing stream of argon at 15 ^{o}C/min. The reaction mixture was stirred vigorously at 290 ^{o}C for 45 minutes and then cooled to room temperature. The nanocrystals are precipitated using 50 ml of ethanol (100%) and then washed twice more. The nanocrystals were finally dispersed in hexanes. These nanocrystals are used as the material for the shell growth. The core $NaYF_4$ nanocrystals synthesis was followed as in the previous section till heating to 297 ± 2 ^{o}C. The reaction was continued for 60 minutes at 297 ± 2 ^{o}C after which the cubic nanocrystals were injected into the core nanocrystals solution. The temperature drops between 285 - 290 ^{o}C when the cubic nanocrystals are injected. The reaction was allowed to continue for 10 minutes after the injection followed by cooling the reaction to room temperature. The washing procedure was the same the core nanocrystal synthesis. The samples were finally dispersed in hexane. The same procedure is followed for $NaYF_4/NaTmF_4$ nanocrystals.

5.4.3 Energy-dependent and resonant X-ray photoelectron spectroscopy

These experiments were carried out with the synchrotron light source at the Canadian Light Source Inc. The samples were prepared by drop-casting the nanocrystals hexane dispersions on to a thin gold foil. The gold foil was mounted on a sample holder using a double sided tape. The gold foil was used for two purposes: 1) reference material; 2) reduce the charging of the sample. The sample holder is mounted inside the sample chamber which is under 10^{-6} Torr vacuum. The measurements were carried out at the Spherical Grating Monochromator (SGM) beamline at the Canadian light Source. Different excitation photon energies were used for depth profiling of the samples. The photoelectron peaks from gold is used as the reference spectrum. The same procedure was followed for resonant XPS. The X-ray absorption spectra is measured by tuning the photon energy so that the 3d electrons of the lanthanides can be excited to the next unfilled orbital which in this case is the unfilled 4f orbitals. The total electron yield of the sample is measured as a function of incident photon energy. At each excitation energy, the current is integrated for 1 sec.

Chapter 6. Long-Term Colloidal Stability and Photoluminescence Retention of Lead- Based Quantum Dots in Saline Buffers and Biological media through Surface Modification

The silica coating of the QDs and the PVP exchange process was performed by Keith Abel. The PVP-COOH polymer was synthesized by Noah Johnson.

6.1 Introduction

In chapter 4 lanthanide-doped nanocrystals have been studied for their utility as potential optical bioimaging agents for deep-tissue imaging. However, there are several obstacles which are faced when one uses lanthanides as a bioimaging agent. In this chapter an lead-based quantum dots are explored as an alternative bioimaging agent. There are several key issues to be addressed before the lead-based quantum dots can be employed as a bioimaging agent. This chapter elucidate those key issues and the pathways to solve them, so that the lead-based quantum dots are compatible to be employed as bioimaging agents. The key issues which are to be solved are as follows.

One of the important aspects of colloidal stability of nanocrystals is the coordination strength between the surface ligands and the nanocrystals.[154] The colloidal stability of nanocrystals is vital for bio-applications like live-cell imaging, *in-vivo* imaging, and whole-body animal imaging.[16,204-206] When the nanocrystals are used in aforementioned applications, the presence of biomolecules, high salt concentrations, and buffers in the physiological environment might lead to interaction with the ligands resulting in their replacement from the surface of the nanocrystals. This induces instability in the colloidal

system often resulting in the precipitation of the nanocrystals from the solution and negatively affects the photoluminescence properties. The surface ligands in general are dynamic which leads to poor colloidal stability. This loss of stability often occurs after surface modification of the nanocrystals through a ligand exchange process or a polymer coating. A system where ligands are bound to the surface of the nanocrystals without getting detached in presence of bio-molecules and salts in the environment is thus of paramount importance for colloidal stability and aforementioned applications. A wide variety of nanocrystals has been employed for bioapplications, especially cadmium and non-cadmium based quantum dots (QDs) due to their high quantum yield and photostability. Interest has arisen in the last few years to exploit the near-infrared (NIR) emitting lead-based QDs towards biolabeling because of their emission wavelengths lying in the biological window (transparent region of the tissue, 700 to 1100 nm).[207-213] These quantum dots also have the potential to be employed in an array of applications like telecommunications, light-emitting diodes, solar light harvesting, quantum computing, and bio-labeling.

The requisite for bioimaging and all other applications is that the QDs exhibit excellent colloidal stability in various solvents, photostability, and resistance towards oxidation. In this sense our group has reported the beneficial effect of TOP in the synthesis of PbS QDs which makes them less susceptible to oxidation when exposed to air.[214] Furthermore, Hollingsworth and coworkers reported an efficient cation exchange process to obtain core/shell (PbSe/CdSe and PbS/CdS) QDs which were photostable and exhibited remarkable resistance towards oxidation under ambient atmopshere.[98] The

evidence for a core/shell structure has been convincingly given by our group with the help of synchrotron-based energy-dependent X-ray photoelectron spectroscopy (XPS), energy-filtered transmission electron microscopy (TEM), high angular annular dark-field imaging (HAADF), and photoluminescence spectra.[99]

The presence of oleates on the surface of these QDs limits their applicability in bioimaging because the hydrophobic oleate ligands cannot disperse the QDs in water. Obtaining a stable dispersion of the QDs in water and buffers is essential. There are only a handful of reports on the surface modification of lead chalcogenide quantum dots. The first group to show surface modification of lead-based QDs was Colvin and coworkers. They used 11-mercaptoundecanoic acid to replace the oleates on the surface of the PbSe QDs to transfer them from hydrophobic to hydrophilic phase.[215] They mentioned that the particles were stable in water, but not in physiological saline buffers. Wise and coworkers employed the same strategy to disperse PbSe and PbS QDs in water and buffer and imaged human colon cells employing the QDs.[213] The stability in buffers was improved to a little extent by Hinds *et al.* by modifying the surface of the PbS QDs by exchanging the oleates with 1-mercaptoundec-11-yl-tetra(ethylene glycol).[211] They reported a quantum yield of 26% in HEPES buffer with colloidal stability for 5 days. They did observe a shift of 60 to 70 nm towards the red after the ligand exchange. The authors attribute this shift to the change in electronic density and confinement due to the Pb-thiol bond, and the effective growth of the QDs upon exchange. The reason for loss of stability in buffer after 5 days is probably due to the dynamic nature of the ligands present on the surface of the QDs. The same group in conjunction with Winnik and coworkers has

reported another ligand exchange method with polyacrylic acid to disperse PbS QDs in water.[212] They observed a decrease in quantum yield which they attribute to the fact that the QDs oxidized over time due to exposure to oxygen present in water and air. They observed a good colloidal stability in water, however, no information was provided regarding the stability of the QDs in buffers.

Other than ligand exchange there are three reports by Ma and coworkers where they have used an amphiphilic polymer poly(maleicanhydride-1-*alt*-octadecene) (PMAO) to coat the PbS QDs using the hydrophobic effect between the surface ligands and the octadecene chain present in the polymer.[207,209,216] They reacted some of the anhydride rings with polyethylene glycol (OH terminated) to make them biocompatible as well. They observed that the particles were stable in water with luminescence retention for a few minutes after which it was lost. When they did the same process with PbS/CdS QDs the authors observed the QDs retained their luminescence with a 59 nm blue shift. The authors mentioned that the QDs were quite stable in buffers, but unfortunately they did not mention for how long. The authors attribute the blue shift to the reduction in the size of the core PbS. I speculate that the blue shift might be due to the fact that the shell CdS got completely etched and to an extent the core PbS as well during the phase transfer process. The other reason for the loss of luminescence may be that, when modifying PMAO the authors use a strong acid (H_2SO_4) to react the alcohol groups of PEG with the anhydride groups of PMAO, at 65 ^oC for 12 hours. This could have resulted in the opening of all the anhydride rings in PMAO due to the strong acid catalyst and the high temperature for refluxing. The large amount of carboxylic acid groups (~ 200) per

polymer chain in PMAO could have replaced the oleates on the surface of the QDs over time. The replacement of oleates by carboxylic acid groups would allow water to reach the surface of the QDs. The presence of water on the surface of the QDs seems to be dentrimental to the photoluminescence of the QDs which has been observed by Winnik *et al.*, and Colvin *et al.*[212,215] The presence of even trace amounts of acid after the modification could as well have caused the loss of luminescence for PbS QDs and the etching of the PbS/CdS QDs.

There is a thus a necessity for a surface modification method that fulfills the following three criteria: 1) colloidal stability in water, saline buffers, and serum-supplemented growth media; 2) retention of luminescence of the QDs in water, saline buffers, and growth media; and 3) resistance towards oxidation when exposed to ambient atmosphere and dissolved oxygen in water. To achieve these criteria, four different surface modification methods were tried. The first approach was to coat the QDs with silica. The main reason to employ silica coating approach is that it could potentially lead to the formation of less toxic materials due to the bio-compatible layer of silica coated on the surface of the QDs. Silica coating on the QDs made the QDs stable in water, but they were not photoluminescent. The second method was to exchange the oleate ligands coated on the QDs with polyvinylpyrrolidone (PVP). PVP is a biocompatible, amphiphilic polymer which can coordinate towards inorganic nanocrystals and offers the highest protective values for stabilizing nanoparticles among all water-soluble polymers.[146] Exchanging the oleates with PVP resulted in a stable colloidal dispersion of QDs in water and apolar solvents; however the photoluminescence was lost after a few

days. The third method was to employ intercalation because it offers an advantage over the aforementioned methods because of the fact that the oleate monolayer remains intact on the surface of the QDs and thus hopefully any solvent effects are minimized (i.e. water cannot easily absorb on to the surface of the QD). Intercalation was done between the oleate groups of the polyethyleneglycol-monooleate (PEG-oleate) polymer and the oleate ligands on the QDs using hydrophobic interactions while the PEG chain provided water dispersibility. The emission stayed even after two months in contrast to the other two methods, but the QDs had poor dispersion stability once the excess PEG-oleate polymer had been removed.

The last method elucidated in this chapter is to use the intercalation method to coat the QDs followed by the crosslinking of the polymer. The amphiphilic polymer poly(maleicanhydride-*alt*-1-octadecene) (PMAO) functionalized with PEG-amine molecules was used to coat the surface of the QDs through intercalation due to hydrophobic interactions and then crosslink the polymer using bis(hexamethylene)triamine (BHMT) in water. This strategy resulted in stable dispersions in water, saline buffers, biological growth media, and various pH conditions. The luminescence was retained even after 7 months in water and buffers and in different pH conditions. The QDs show excellent photostability and good susceptibility towards oxidation when exposed to ambient atmosphere over 7 months.

6.2 Results and Discussion

6.2.1 Synthesis of QDs

The synthesis of the QDs was done by following a procedure reported by our group with some slight modifications.[99,214] The QDs were synthesized through the hot injection method at different temperatures to obtain QDs emitting at different wavelengths (Table 6.1). All the QDs were synthesized in an organic medium with hydrophobic oleate ligands on the surface. The cation exchange reaction resulted in a PbS/CdS and PbSe/CdSe core/shell structures which shifted the emission wavelength towards the blue when compared to the core PbS and PbSe QDs, respectively.[99] The Figure 6.1 A shows the luminescence spectra of PbS core QDs and the blue shifted PbS/CdS core/shell QDs and the luminescence spectra of PbSe core and PbSe/CdSe core/shell QDs are shown in Figure 6.1 B. The TEM in Figure 6.1 C&D show that the QDs are uniform in size and shape. The long range ordering of the PbSe QDs (Figure 6.1 D) show that they are highly monodisperse (< 5% standard deviation). The as-synthesized monodisperse hydrophobic QDs cannot be used as bio-label for optical imaging as they cannot be dispersed in aqueous media. So the QD surface had to be modified to employ them as bio-labels. The next section deals with the surface modification of the dots to disperse them in water, saline buffers, and biological media.

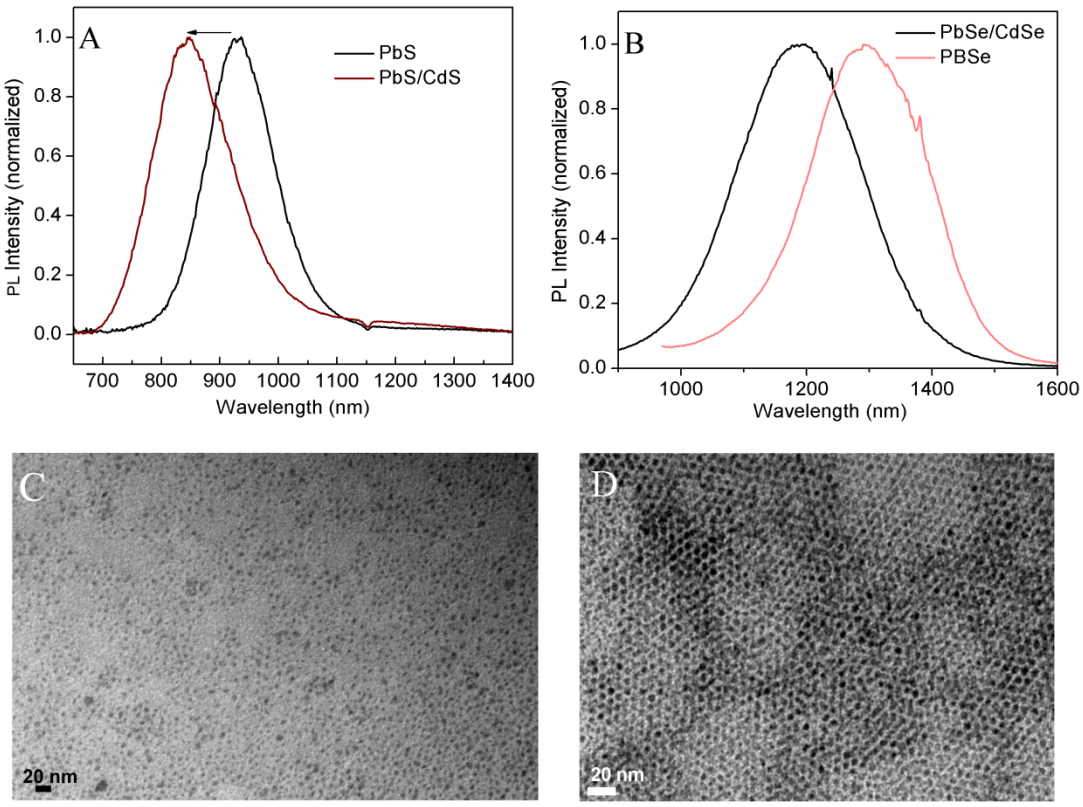

Figure 6.1. (A) Luminescence spectrum of PbS and PbS/CdS QDs in TCE; (B) Luminescence spectrum of PbSe and PbSe/CdSe QDs in TCE; (C) Representative TEM image of PbS/CdS QDs; (D) TEM image of PbSe QDs.

Table 6.1. Reaction times, temperatures, and emission wavelengths for the synthesis of PbS and PbSe QDs. The PL measurements were done in TCE.

QDs	Reaction Temperature	Reaction Time	Approximate Emission Wavelength (nm)
PbS	90 ^{o}C	30 min	910 nm
PbS	100 ^{o}C	1 min	1000 nm
PbSe	120 ^{o}C	3 min	1250 nm
PbSe	130 ^{o}C	4 min	1390 nm

6.2.2 Phase transfer of QDs to water

Silica coating

Our first approach to phase-transfer of QDs to water was achieved by encapsulating the QDs with a shell of silica. Furthermore the presence of silanol groups on the surface of silica opens up the possibility for further surface modification required for targeted imaging. A generalized procedure developed by Stöber for the preparation of monodisperse silica particles has been modified to coat the hydrophobic QDs with silica.[54] A water-in-oil microemulsion system which is a modified form of the Stöber synthesis is an ideal methodology for coating a silica layer over hydrophobic QDs and has successfully been applied to a number of nanoparticle types.[120,217-218] Thomas Nann

and co-workers reported the first study on silica encapsulated PbSe QDs. Although they were able to encapsulate the PbSe QDs with silica to some extent, they did not furnish any results of the coated QDs photoluminescence studies.[219] The method herein is adapted from Koole *et al.* and it involves a microemulsion system with cyclohexane as the oil phase and Synperonic NP-5 as surfactant.[220] It is thought that exchange of the oleates with TEOS occurs spontaneously followed by transfer to the hydrophilic phase of the microemulsion where shell growth occurs. Incorporating on average, a single QD per silica bead is a considerable challenge and it requires careful control over reactant and nanoparticle concentrations.

Cyclohexane, NP-5, TEOS, and the PbSe QDs were mixed together in a single necked flask. Subsequently, ammonium hydroxide solution (aqueous, 33 wt %) was injected to initiate shell growth. The solution was stirred for 24 hrs, followed by washing and isolation. The silica-coated PbSe QDs were stable in ethanol and water solvents for several days. TEM images of silica-coated PbSe QDs are shown in Figure 6.2 A. For most of the particles, a single PbSe QD had been encapsulated per silica sphere and we could observe a fairly uniform coating of each QD. Qualitatively, it is noticed that the small QDs (~3-5 nm) had partially been dissolved by the ammonium hydroxide catalyst, consistent with the TEM results.[219] However, starting with larger PbSe QDs (~5-7 nm) resulted in significantly reduced etching of the QDs. Despite the excellent coating of the PbSe QDs, no PL signal was found after silica coating. This may explain the absence of PL spectra in previous reports.[219,221] The absence of PL could be attributed to the etching process which might have resulted in the large number of surface defects thereby

quenching the emission. The other reason could be due to the presence of large number of hydroxyl groups in the encapsulated silica which might have quenched the emission. The luminescence was still absent when the procedure was performed on PbSe/CdSe core/shell QDs. The loss of luminescence in the core/shell QDs is also attributed to the etching process of the QDs which results in the loss of the protective CdSe shell.

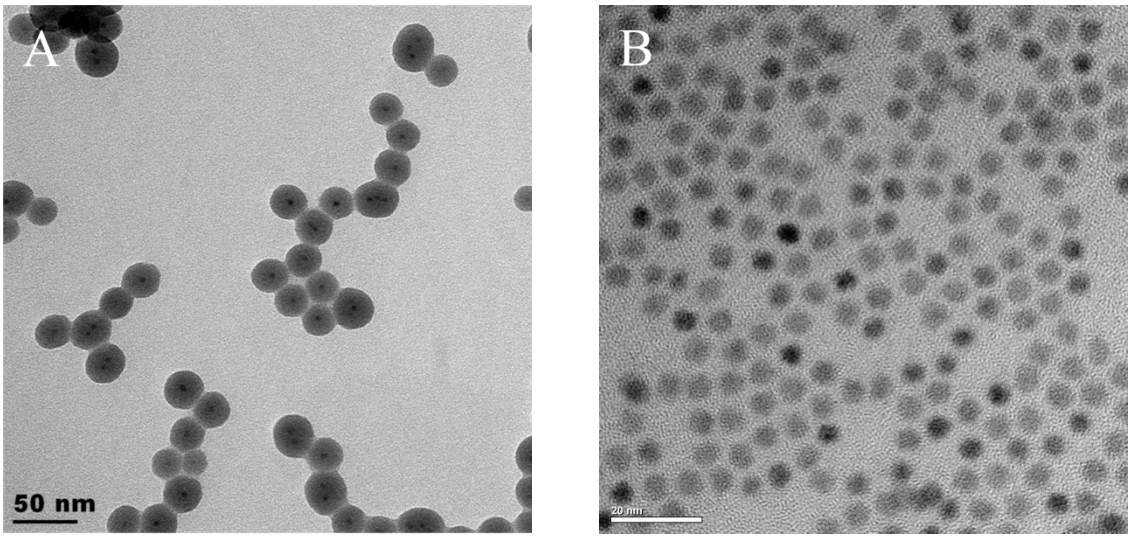

Figure 6.2. (A) Silica coated PbSe QDs; (B) PbSe QDs after PVP ligand exchange.

Ligand Exchange with Polyvinylpyrrolidone (PVP)

A versatile ligand exchange strategy could potentially provide further opportunity to make the QDs suitable for bioimaging purposes. Even though there has been tremendous development in the field of ligand exchange especially for CdSe-based QDs, it's not a straightforward process to implement the process in lead-based QDs. In this section, a ligand exchange method is reported by employing a polymer polyvinylpyrrolidone (PVP) for effective transfer of the QDs from apolar to polar solvents. The polymer was functionalized with carboxylic acid end group in order to obtain better coordination

between the PbSe surface and PVP. The coordination of carboxylic acid groups on to surface of the QDs will impart better stability for the quantum dots.

The ligand exchange was done in presence of large excess of PVP. The exchanged QDs dispersed (stable dispersion for 1 month) well in polar and apolar solvents with no aggregation or precipitation which was confirmed from the TEM images as seen in Figure 6.2 B. The TEM images show that the QDs are well separated even after the exchange. A decrease in the size of the QDs is observed which is consistent with the blue shift observed in the photoluminescence after the exchange.[212] The decrease in particle size is due to the etching when the Pb-oleates present on the surface of the QDs were replaced by PVP-COOH polymer. The ligand exchanged QDs in DMF (Figure E.1) and ethanol (Figure 6.3 A) retained their photoluminescence signal, however, they were blue shifted when compared to the original QDs in TCE. The blue shift observed depends on the size of the QDs, smaller the size bigger the shift and vice versa. It should be noted that the magnitude of the observed blue shift for the QDs depends on their size. When the ligand exchanged PbSe QDs were dispersed in water the photoluminescence significantly diminished and the peak became broader with respect to the unexchanged QDs in TCE (Figure 6.3 A). PVP provides excellent dispersion stability in a variety of solvents, however, the photoluminescence intensity decreased and dropped off completely in a matter of a few days (Figure E.2). This can be attributed to the fact that PVP, being hygroscopic, absorbs water efficiently and the contact between the PbSe surface and water seems to be detrimental to its photoluminescence properties. The photoluminescence properties of core/shell, PbSe/CdSe also did not show any

improvements when compared to PbSe QDs after the ligand exchange process. In order to solve this, an intercalation approach was employed to disperse the QDs in water and to observe whether the photoluminescence was retained.

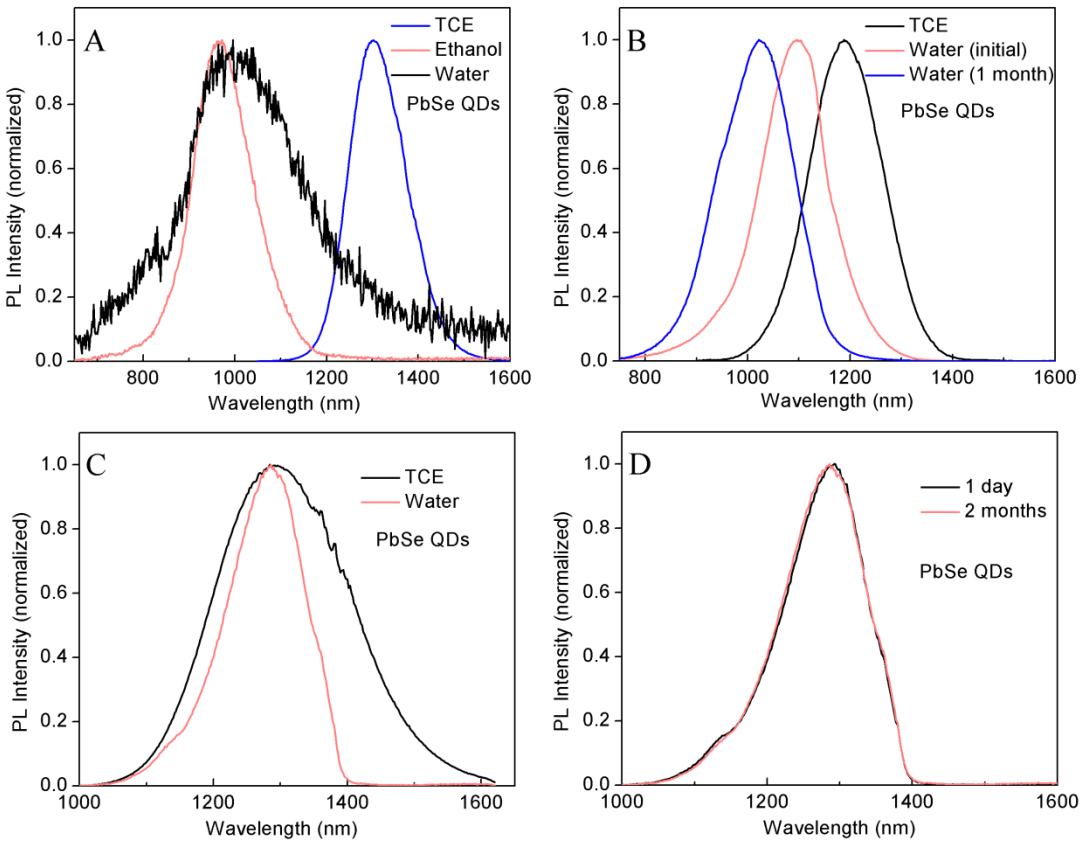

Figure 6.3. Luminescence spectra (A) PbSe after ligand exchange with PVP; (B) PbSe after intercalation with PEG-oleate; (C and D) PbSe/CdSe core/shell after surface modification with PEG-oleate.

Intercalation of polyethyleneglycol-monooleate (PEG-oleate) into the oleates on the surface of QDs

Ligand intercalation is the inclusion of a molecule between surface ligand molecules on the nanoparticle rather than replacing the initial capping ligands. When an amphiphilic molecule such as poly(ethylene glycol) monooleate (PEG-oleate) is used for the intercalation, the hydrophobic oleate part of the PEG-oleate intercalates with the hydrophobic oleate ligands on the surface of the QDs while the hydrophilic PEG tail chain is oriented outwards resulting in the dispersibility of the QDs in water. The schematic diagram for PEG-oleate intercalation is shown in Figure E.3. PEG-oleate is an inexpensive commercially available polymer, and the presence of PEG molecules makes the polymer biocompatible. The intercalation resulted in high-quality dispersions of PbSe QDs in water with the retention of photoluminescence signal (Figure 6.3 B). The photoluminescence spectral shape remains Gaussian similar to the precursor QDs, but a noticeable blue shift was observed (~100 nm). The blue shift in photoluminescence is likely caused by etching, but the exact mechanism is unclear. After 1 month storage in the dark in water, the PbSe QDs had blue shifted even further by ~80 nm. Please note here that the excess PEG-oleate had not yet been removed from this dispersion. To improve photostability over the original core QDs and minimize the amount of blue shifting (i.e. PbSe core etching), PbSe/CdSe core/shell QDs prepared by cation exchange were utilized for the intercalation. No shift in photoluminescence position was observed for the core/shell QDs, as shown in Figure 6.3 C. The change in the spectral shape

observed (Figure 6.3 C & D) can be attributed to an overtone absorbance of water in the NIR at 1400 nm (Figure E.4).

In presence of excess polymer the photoluminescence signal intensity had not reduced and the spectral shape and position had remained the same (Figure 6.3 D) in water even after two months storage. Furthermore, the newly formed colloidal QDs in presence of excess polymer displayed greater photoluminescence stability in water than either of the silica-coating or ligand exchange methods. The major disadvantage is that the QDs are not stable in water even for a few hours after removing the excess polymer through centrifugation. In presence of excess polymer, due to the labile nature of the ligands, if one polymer ligand detaches from the surface of the dots there are several others to replace it, which results in good dispersibility over long periods. On the other hand, in the absence of excess polymer, once the ligand gets detached from the surface, there are not enough polymer ligands in the solution to replace it. This suggests that the PEG-oleate coated QDs are able to retain their luminescence but not their dispersibility in water. Hence the logical strategy to impart water dispersibility and retain the photoluminescence is to use the same intercalation process, but make the ligands less dynamic in nature.

Intercalation of PEG-amine functionalized PMAO into the oleates of the QDs followed by crosslinking of the polymer

A similar intercalation process like above was employed with an amphiphilic polymer to coat the QDs and to disperse them in water. To increase the stability of the colloid the amphiphilic polymer was further crosslinked which reduced the labile nature of the coated polymer chains. To perform this coating a robust surface modification route when

compared to previous reports[207,216] was employed to obtain colloidal stability in water, saline buffers, and in serum-supplemented growth media. Utilizing the intercalation process the oleate-coated PbSe and PbS QDs were intercalated with the hydrophobic octadecene chain of the amphiphilic polymer PMAO while the anhydride rings coat the QDs. To provide biocompatibility and increase the water solubility of the polymer some of the anhydride rings were opened with PEG-amine. This makes the polymer-coated QDs water dispersible. This methodology ensured that the number of anhydride rings opened is limited to the number of PEG-amine molecules added. If too many numbers of carboxylic acid groups are opened they might replace the oleates on the surface of the QDs thereby allowing water access to the surface of the QDs which causes detrimental effect on the luminescent and colloidal properties of the QDs. To enhance the colloidal stability of the QDs the anhydride rings were crosslinked using bis(hexamethylene)triamine (BHMT). The ratio of 1:20 between PMAO and BHMT in principle could crosslink all the remaining anhydride chains left after the functionalization with PEG-amine in the polymer. When crosslinking occurs, the anhydride groups open to form amide bonds and carboxylic acid groups. The presence of carboxylic acid groups on the surface of the QDs will facilitate further conjugation to antibodies, proteins, and other bio-molecules.

The crosslinking results in an exceptional stability of the QDs in water and in biological media. Due to the crosslinking the PMAO becomes a crosslinked chain around the QDs which restricts its movement. This reduces the dynamic nature of the ligands and provides stability to the colloids. The crosslinking suppresses the dynamic nature of the

polymer coated on the surface of the QDs thereby protecting the surface of the dot from exposure to the external environment. An interesting fact to note here is that, if the crosslinking was done in the organic phase we found that we would lose more than 75 % of the QDs. The loss of QDs could probably be due to the inter-particle crosslinking which results in a big loss of the QDs during filtration. To avoid the loss of QDs, the crosslinking of the polymer was done after the PMAO-PEG coated QDs were dispersed in water. This approach led to a colloidal stability of the QDs in water for more than 7 months. The crosslinking of polymer in water had two beneficial effects: 1) the amount of QDs lost after the surface modification process was minimal (less than 10%). This was confirmed by the concentration of the QDs before and after the surface modification using absorption spectra; 2) there was virtually no inter-particle crosslinking. This could be due to the fact that the hydrophobic part of the polymer stays close to the surface of the QDs and the PEG chain is completely solvated by water. This reduces inter-particle crosslinking and enhances the amount of QDs obtained after surface modification.

The luminescence was retained in water with only a small blue shift (~ 5 nm) in water and the emission intensity did not decrease even after 7 months. The crosslinking seems to be an efficient process in terms of the retaining its luminescence, and colloidal stability in water. The water dispersible QDs do not dry the normal way like the QDs dispersed in organic solvents. The water dispersible QDs dry in patches on a formwar grid. The QDs observed in the patches seen in TEM from Figure 6.4 A show that they are well separated which suggests that there could be minimal interparticle crosslinking between the QDs.

The PbSe QDs show an appreciable blue shift in the emission peak (980 nm) when compared to its original peak at 1390 nm (Figure 6.4 B). This happens when we sonicated the reaction mixture, whereas we did not observe a big blue shift in the absence of sonication. Sonication and the presence of amine groups (BHMT) probably etch the QDs which result in the blue shift. Furthermore, the PbSe QDs are known to be a little less stable when compared to PbS QDs. When the samples were left exposed to air and ambient light for several months the luminescence did not shift by more than 30 nm to the blue (Figure 6.4 B) exhibiting the effectiveness of the coating procedure. In case of PbS QDs the sonication shifted the emission by 10 nm. The emission peak remains constant (Figure 6.4 C) even after being exposed to ambient atmosphere for 7 months. I speculate that this could be due to further etching and self-ripening process occurring after the surface modification. Sonication was necessary to hasten the reaction process between PEG-amine and PMAO and further facilitate the crosslinking process.

No blue shift in the emission was observed if the samples were not sonicated, however, this makes the surface modification process long and tedious. This observed blue shift after surface modification was resolved by employing core/shell PbS/CdS QDs (Figure 6.4 D). These QDs when subjected to sonication did not show any appreciable blue shift even after 7 months in water. The reason could be due to the fact the thin CdS shell on the surface make them more stable than PbS QDs and resistant to the etching process due to the sonication process and the presence of amine groups. Furthermore, the emission from PbS/CdS QDs did not shift after being exposed to water and ambient atmosphere for 7 months. The presence of emission and the absence of blue shift even after 7 months in

ambient conditions suggest that the oxidation of the QDs have effectively been suppressed by protecting their surface with the crosslinked PMAO-PEG-BHMT polymer. The absence of oxidation and the presence of emission after 7 months is a significant improvement over other surface modification methods previously reported. Most of the surface modification processes can only be performed only a small scale of ~ 10 mg of QDs. With this method ~ 100 mg of QDs can easily be transferred from hydrophobic to the hydrophilic phase.

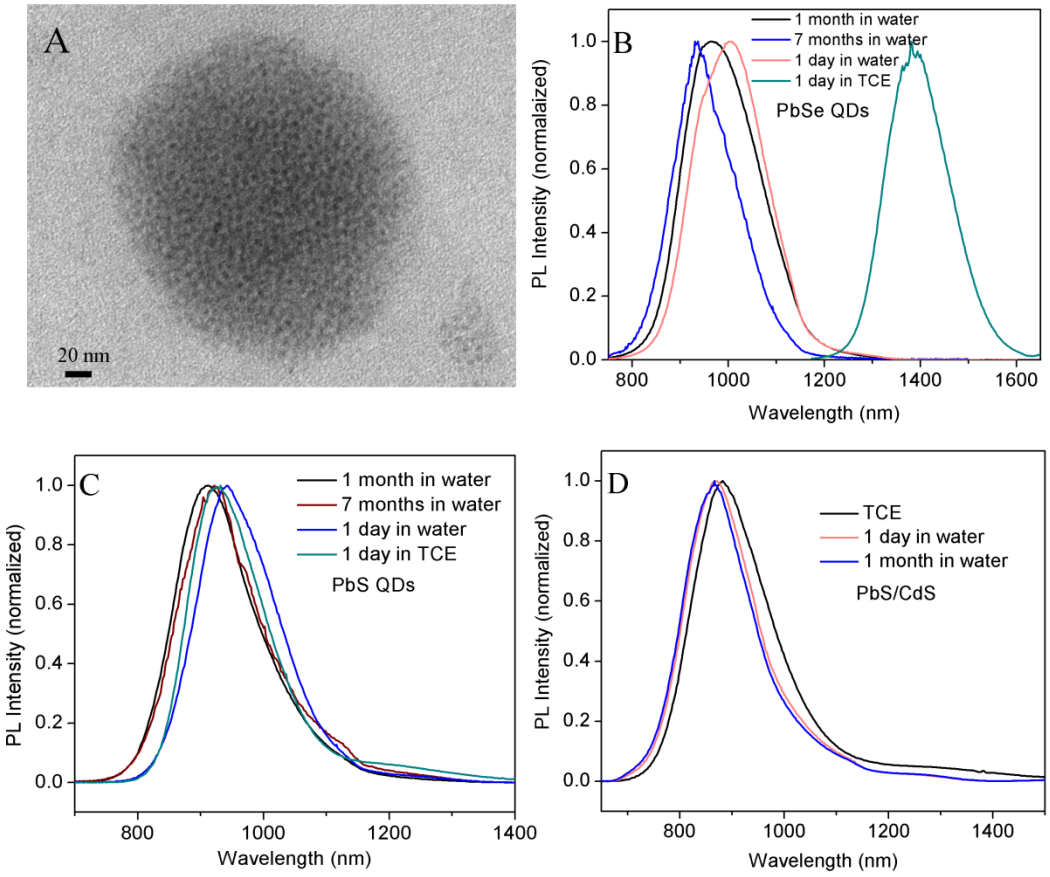

Figure 6.4. (A) TEM image of water dispersible PbS QDs after surface modification; (B) PbSe QDs before and after surface modification; (C) PbS QDs before and after surface modification;

(D) PbS/CdS QDs before and after surface modification. All the QDs were coated with PMAO-PEG-BHMT.

Stability of the crosslinked PMAO-PEG-BHMT coated QDs in various physiological media and at different pH values

Having tested the stability of the QDs in water it is imperative to test the colloidal stability of the QDs in saline buffers, different pH values, and serum-supplemented growth media. The colloidal stability of QDs in buffers, pH values, and serum-supplemented growth media is an important physical parameter for *in-vivo* and live cell imaging. When QDs (~400 nanomolar) were dispersed in 3 ml of phosphate (7.4 pH), TRIS (7.6 pH), or borate (8.6 pH) buffered saline (Figure 6.5 A), the QDs were stable for more than 7 months with no precipitation observed. The long-term QD stability in these conditions is a significant improvement over the 6 days of colloidal stability of PbS QDs in HEPES buffer reported by Hinds *et al.*[211] The crosslinked polymer-coated QDs retained their emission and did not show big shift in their peaks even after being dispersed in buffers for 7 months (Figure 6.5 B, Figure E.5, Figure E.6, Figure E.7). The buffers mimick the pH, osmomolarity, and saline conditions of blood.

However, there are also proteins and other biomolecules present in blood. The stability of the QDs in presence of serum-supplemented growth media was tested. When the conditions were kept at 37.4 ^{o}C and 4 ^{o}C the QDs were colloidally stable for more than 4 days. The QDs also retained their emission after being dispersed in such conditions after 4 days. The luminescence spectra of PbS/CdS and PbSe QDs dispersed in growth media did not change after being kept at 4 ^{o}C for 7 months (Figure 6.5 C&D, Figure E.8). If the

bio-molecules and salts can interact with the QDs then the colloidal stability goes down drastically. The main reason for this stability can be attributed to the fact the hydrophobic nature of the oleate on the QDs and the octadecene chains of crosslinked amphiphilic polymer minimizes the effect of water or salts or other biomolecules with the surface of the QDs. This result in the emission being retained and the exceptional stability observed for the QDs dispersed in the buffers and serum-supplemented growth media. This kind of stability and poor interaction with bio-molecules and salts is useful for applications like targeted tumor imaging. The QDs dispersed in various pH values ranging from 5 to 14 retained their emission (Figure 6.6 & Figure E.9) and colloidal stability for more than 7 months. The crosslinked polymer coating on the QDs make them robust at such varied pH ranges. However, there is a problem with this crosslinked polymer because it precipitates out from the solution in presence of divalent cations like calcium and magnesium.

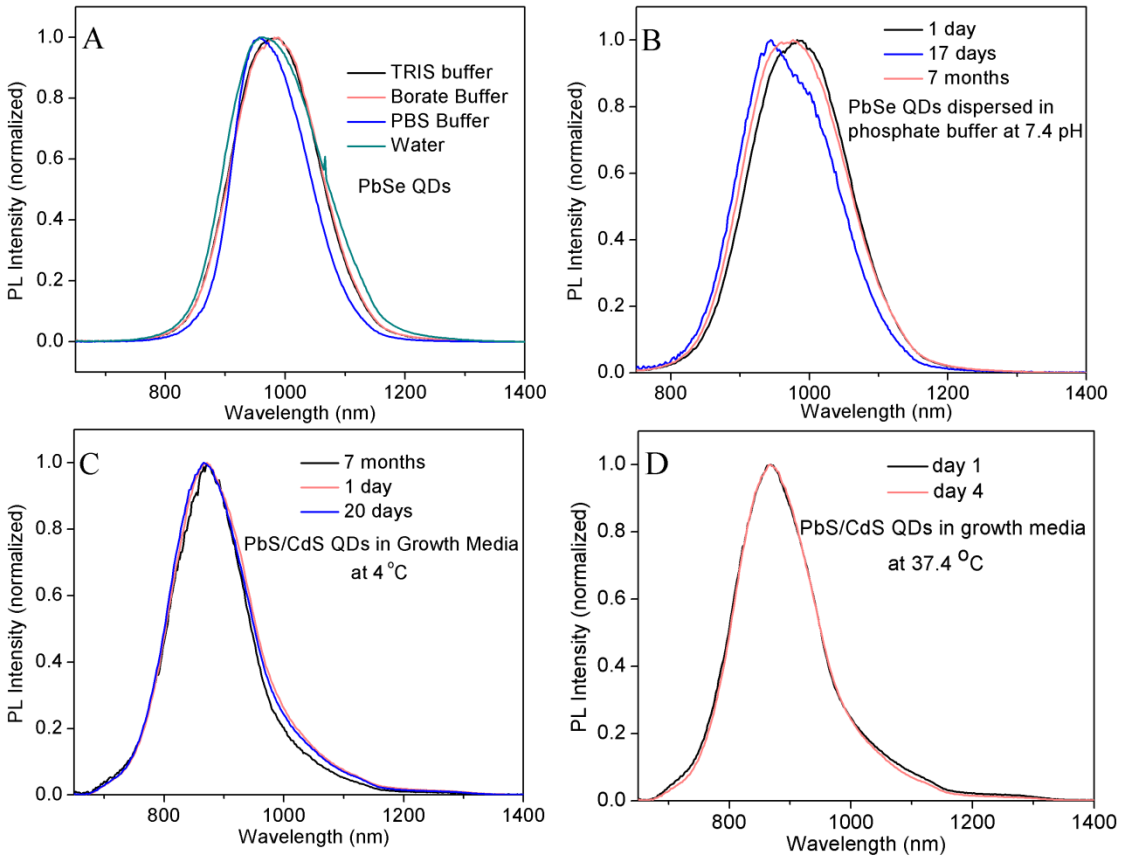

Figure 6.5. (A) PbSe QDs in various buffers after surface modification with PMAO-PEG-BHMT; (B) PbSe QDs in phosphate buffers at various days; (C&D) PbS/CdS in serum-supplemented growth media at 4, and 37.4 ^{o}C, respectively, after surface modification with PMAO-PEG-BHMT.

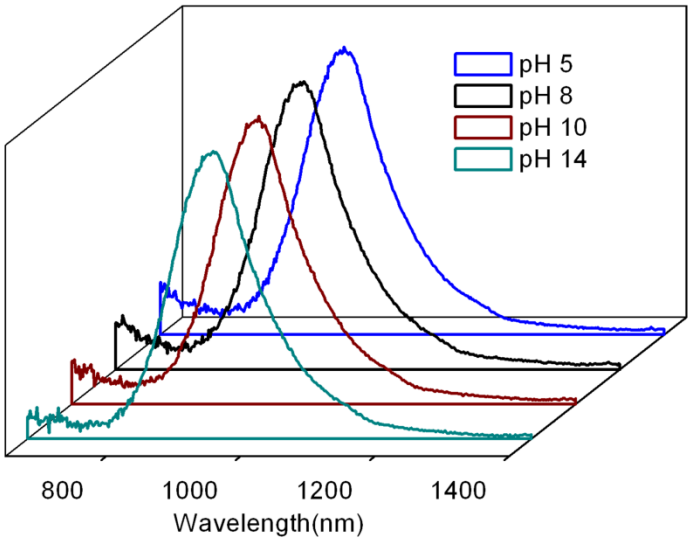

Figure 6.6. PMAO-PEG-BHMT coated PbS QDs at different pH values.

6.3 Conclusions:

It can be concluded that the first two surface modification methods, i.e silica coating and ligand exchange with PVP imparted excellent water dispersibility to the QDs but fail to retain the photoluminescence of the core and core/shell QDs. On the other hand, the PEG-oleate intercalated QDs exhibited poor water dispersibility in the absence of excess polymer, but retained their photoluminescence. The last strategy of intercalation and further crosslinking of the polymer (PMAO-PEG) coating on the QDs made them stable in water, buffers, and serum-supplemented growth media and at different pH values for several months. The QDs also retained their luminescence under ambient conditions for more than 7 months in different aqueous media. The stability in serum-supplemented

growth media at 4 ^{o}C was more than 7 months while the dispersion at 37.4 ^{o}C was stable for more than 4 days. This crosslinked amphiphilic polymer coating meets all the requirements mentioned for a general method to coat lead-based QDs and disperse them in various aqueous media. Furthermore this coating can be done on a relatively large scale of 75-100 mg of QDs. This intercalation and further crosslinking of the amphiphilic polymer makes the lead-based QDs robust and viable for bio-applications. This crosslinking method to perform surface modification on the lead based QDs could easily be adapted for other types of nanocrystals as well.

6.4 Experimental Section

Reagents and Materials. Lead(II) oxide (powder, 99+%), lead(II) acetate trihydrate (99.999%), selenium (powder, 99.5+%), cadmium acetate hydrate (99.99+%), bis(trimethylsilyl) sulfide [$(TMS)_2S$] (synthesis grade), octadecene (ODE) (tech. grade, 90%), oleic acid (OA) (tech. grade, 90%), trioctylphosphine (TOP) (tech. grade, 90%), tetrachloroethylene (TCE) (ACS reagent grade, 99+%), and Synperonic NP-5 were all purchased from Sigma-Aldrich. Chloroform (spectroscopic grade) and toluene (spectroscopic grade) were obtained from Caledon Laboratories LTD. Hexane (ACS reagent grade) was obtained from EMD Chemicals Inc. Poly(ethylene glycol) monooleate (PEG-oleate), M_n ~860, poly(maleicanhydride-alt-1-octadecene) (PMAO), M_n ~30,000-50,000, bis(hexamethylene)triamine (BHMT) was purchased from Sigma-Aldrich. polyethyleneglycol-amine M_n ~2,000 was purchased from Hunstman Chemicals. All the chemicals were used as received.

6.4.1 Synthesis of PbSe semiconductor QDs.

Selenium in TOP (TOP-Se) was prepared first by heating 0.79 g of Se in 25 ml of TOP with rapid stirring inside a nitrogen atmosphere glove box at 80 ^{o}C. Once the solution turned clear (~ 1 hr), the heating was removed and the solution was stored at room temperature inside the glove box. Lead(II) oxide (2 mmol), ODE (30 ml) and OA (1.3 ml) were then loaded into a 100 ml three-neck flask. The mixture was heated to 130 °C under vacuum for at least 2 hrs to ensure all of the PbO had dissolved. The solution was then bubbled with argon and the temperature and reaction time was tuned to obtain the required size and PL position. The temperature used was between 110 and 130 ^{o}C and the reaction time varied from 2 to 4 minutes. Subsequently, 5 ml of the prepared TOP-Se solution was quickly injected into the reaction flask while stirring vigorously. PbSe QD size was controlled by the reaction temperature and time. The final product was quickly quenched into absolute ethanol (~ 150 ml) while stirring. The product was washed and centrifuged at least four times with absolute ethanol (200 ml) until the QDs were completely precipitated. The QDs were dried with a stream of argon and dispersed in TCE for photophysical characterization and storage.

6.4.2 Synthesis of PbS semiconductor QDs

PbS QDs were synthesized by adding lead(II) acetate (1 mmol), ODE (20 ml), TOP (2 ml), and OA (1.28 ml, 4 mmol) to a three-neck flask. The mixtures were heated under vacuum at 120 °C until we obtain a clear colorless solution. The reaction mixture was kept at that temperature for 1 hour. The solution was then bubbled with argon for 15 min. Subsequently, $(TMS)_2S$ (10 μL) was quickly injected (typically between 90 ^{o}C and 110

^{o}C) into the reaction flask while stirring vigorously. The reaction time was tuned depending on the required emission wavelength. Typically the reaction time varied from 30 sec to 4 min. Reaction mixture was quenched by quick injection into cold (~3 °C) absolute ethanol (100 ml) while stirring. The products were centrifuged to form two layers. The colorless, upper ethanol phase was removed, and the lower brown layer was recombined with fresh room temperature absolute ethanol (200 ml) while stirring, and was centrifuged again. This was repeated at least three times with absolute ethanol. The QDs were dried with a stream of argon and dissolved in TCE for photophysical characterization.

6.4.3 Synthesis of PbS/CdS and PbSe/CdSe core/shell QDs

Cadmium acetate (2 mmol), ODE (6.6 ml) and OA (5.1 ml) were loaded into a 50 ml three-neck flask. The mixture was heated to 130 °C under vacuum for at least 2 hrs. The solution was then bubbled with argon and the temperature lowered to 70 °C. Subsequently, 70-80 mg of PbS QDs (dissolved in 1.2 ml of ODE) were injected into the reaction flask while vigorously stirring for 25 min. The final products were quickly quenched with methanol (~ 100 ml) while stirring. The products were washed and centrifuged twice with methanol (80 ml each), followed by at least two more times with absolute ethanol (80 ml each) until the QDs were completely precipitated. The QDs were dried with a stream of argon and dispersed in TCE for photophysical characterization and in chloroform for further surface modification.

6.4.4 Silica-coating synthetic procedure

10 ml of cyclohexane, 1.3 ml of NP-5, 400 µL of PbSe solution and 50 µL of TEOS were mixed and stirred for 30 minutes. The exact PbSe QD concentration was determined from the absorption spectrum on a batch to batch basis, as changes in particle weight (due to differences in ligand amounts) result in substantially different QD concentrations. Subsequently, 100 µL of an ammonium hydroxide aqueous solution (33 wt %) was then injected to initiate shell growth. The solution was stirred for 24 hrs. The particles were preciptitated using acetone and centrifuged/washed with ethanol (50 ml). Sonication was used to redisperse the particles in ethanol or water.

6.4.5 PVP-COOH ligand exchange procedure

PVP-COOH was prepared according to Ref.[222] The molecular weight (M_n) of the polymer was ~1,800 as determined by MALDI-MS. PbSe QDs (~5 mg) were mixed with PVP-COOH polymer (400 mg) in chloroform (~ 6 ml) overnight at 40 °C. The particles were then precipitated from solution using excess diethyl ether (~500 ml), dried under argon and redispersed in different solvents (e.g. ethanol, water, DMF). Excess polymer was removed by centrifugation at 15,000 g.

6.4.6 PEG-oleate intercalation procedure

PbSe QDs were transferred to water using the PEG-oleate molecules. The intercalation was performed by mixing PbSe QDs (~10 mg) in chloroform (~5 ml) with the PEG-oleate molecules (~500 mg) and then stirred overnight. The chloroform was evaporated using an argon flow and then in a rotary evaporator under vacuum. The QDs were heated

at 60 °C for 10 min before addition of water. Water was added drop wise, forcing interaction with the polar head groups of the PEG-oleate facing out towards the solvent. Excess PEG-oleate was removed by preparative centrifuge at 25,000 g.

6.4.7 Surface modification using PMAO-PEG and crosslinking using BHMT

In a general procedure PbSe/PbS QDs (40 mg) in 10 ml of chloroform were mixed with 500 mg (0.0125 millimoles) of PMAO (M_n ~ 30,000 – 50,000) and was stirred for 12 hours. PEG-amine (M_n ~2,000) amounting to 500 mg (0.25 millimoles) was added to the above mixture after 12 hours to convert some of the anhydride groups to amide. The ratio between anhydride rings to amines for the process was 1: 20. The reaction mixture was stirred overnight to complete the reaction between amines and anhydrides. Subsequently, the solvent chloroform was evaporated in a rotary evaporator followed by the addition of water. The mixture was then sonicated disperse the polymer-coated QDs. Bis(hexamethylene) triamine (54 mg, 0.25 millimoles) (BHMT) in 3 ml of water was added to the water dispersible QDs which was then sonicated for 5 minutes, followed by stirring for 30 minutes. The polymer-QDs mixture was then filtered successively through a 0.45 and 0.2 µm filter. The filtered solution was left for 2 weeks after which the excess polymer was removed using a preparative centrifuge at 25,000 g.

6.4.8 Solution photoluminescence measurements

The measurements were performed at room temperature under ambient conditions using an Edinburgh Instruments FLS 920 instrument and a 5.0 mW HeNe laser from Thor Labs as the excitation source (λ_{ex} = 633 nm). All the samples were excited with the HeNe laser

with a 645 and 695 nm filter to cut off the excitation light from reaching the detector. The excitation light was focused on a square quartz cuvette (1 x 1 cm^2) containing the QD solution in TCE. The emitted light was fed to a monochromator (600 lines/mm grating) and collected with a liquid nitrogen-cooled Hamamatsu R5509 photomultiplier tube (PMT) with sensitivity up to 1700 nm. A silicon filter in front of the emission monochromator was used throughout the measurements. The emission spectra were corrected for the instrument response.

6.4.9 Transmission Electron Microscopy (TEM)

The TEM images of the QDs were obtained using a JEOL 1400 instrument operating at 80 kV equipped with a charge-coupled device (CCD) camera. The QDs dispersed in hexane were dropcasted onto a carbon coated formwar grid and dried under air.

Chapter 7. Conclusions and Future Outlook

7.1 Conclusions

This thesis elucidates the synthesis and surface modification of two different kinds of nanocrystals followed by their applicability as bioimaging agents. Chapter 2 deals with the synthesis of LaF_3 nanocrystals doped with Yb^{3+} and Ho^{3+} ions followed by their surface modification with a silica matrix using the sol-gel process. With these nanocrystals an effective control over the red to green ratio obtained from the upconversion process can be observed. In the best case scenario, the ratio of red to green achieved was about 40 to 1. The red light emitted by the Yb^{3+} and Ho^{3+} codoped LaF_3 nanocrystals scatters less than the green emission which would an advantage for imaging deeper inside the tissue. However, to utilize them as bioimaging agents these nanocrystals have to be dispersible in water. These nanocrystals did not disperse in water even after etching with HF.

A different strategy was employed which involved synthesizing the nanocrystals in organic media, followed by surface modification to render them dispersible in aqueous media. The matrix was changed from LaF_3 to $NaYF_4$ to obtain better efficiency with upconversion and control over the size of the nanocrystals obtained from the synthesis. The method of coprecipitation has been used to synthesize the $NaYF_4$ nanocrystals doped with Yb^{3+} and Er^{3+} or Tm^{3+} ions. These nanocrystals were dispersed in water by two surface modification techniques. The first technique was to coat the nanocrystals with polyethylene glycol-monooleate (PEG-oleate) to disperse them in water. The

nanocrystals dispersed in water well for several days (30 days); however the colloidal stability of these nanocrystals after coating with PEG-oleate was poor in physiological saline buffers. The advantage of intercalation is that the luminescence was retained with minimal quenching by solvents. The poor colloidal stability of the nanocrystals was solved by intercalating an amphiphilic polymer poly(maleicanhydride-*alt*-1-octadecene) (PMAO) functionalized with PEG molecules with the oleates on the surface of the nanocrystals. Subsequently, the anhydride rings present in the coated PMAO are crosslinked with a triamine molecule to enhance the colloidal stability of the nanocrystals in physiological saline buffers and serum-supplemented growth media. The coated nanocrystals showed excellent stability in various aqueous media and at different pH values.

In chapter 4 the PEG-oleate and PMAO-PEG coated nanocrystals were tested as bioimaging agents *in-vivo* and *in-vitro*. Upconversion laser scanning two-photon microscopy results suggested that the long life times and poor quantum yield of the nanocrystals do not allow one to image at the same speed when fluorescent proteins and organic moleculesare used as imaging agents. The time taken to obtain a stack of images when imaging inside a tissue over a depth of 100 to 200 µm was a few hours long. Furthermore, imaging could not be done more than 400 to 500 µm deep inside tissue with lanthanide-doped nanocrystals. The above results suggest that using lanthanide-doped nanocrystals as bioimaging agents for two-photon upconversion laser scanning microscopy is not viable. To avoid the long scanning time required for imaging, wide field microscopy was employed. This resulted in obtaining images in a few minutes over

a depth of 100 μm inside the brain of a mouse with optical sectioning. This microscopy technique has the disadvantage of giving lower resolution images when compared with scanning microscopy. However, with this technique, imaging could be done twice as deep with 800 nm emission from lanthanides when compared to the green emission typically used. The poor resolution coupled with poor quantum yield and scattering of light by tissues restricts the imaging to a depth of 300 to 400 μm inside the tissue. Hence, this method also does not solve the goal of imaging deeper than 500 μm. All the above results restrict the applicability of lanthanide doped nanocrystals as imaging agents.

In chapter 5, the lanthanide doped $NaYF_4$ nanocrystals are examined with variable energy X-ray photoelectron microscopy at the synchrotron light source at Saskatoon. This study was done to understand the fundamental properties of the materials in order to synthesize nanocrystals with improved optical properties so that it could become much more viable for bioimaging than the current lanthanide-doped nanocrystals. The results show that the chemical speciation of surface yttriums ions is different for $NaYF_4$ nanocrystals of size more than 10 nm when compared to smaller nanocrystals. This can be observed with the extra doublet peak observed for yttrium ions (3d electrons) in addition to the usual doublet at lower excitation energies where the surface of the nanocrystals is probed. The new doublet slowly disappears as the excitation energy is increased. This phenomenon was observed for nanocrystals with sizes more than 10 nm. A single doublet for 3d photoelectrons of yttrium ions are observed with nanocrystals smaller than 10 nm in size. This suggests that the nanocrystals are significantly different when the size regime changes. Interestingly, when the doped lanthanide ions were examined with the variable

energy XPS there was no signal. The 4d peak emission was observed only with resonant XPS measurements. The preliminary results suggest that to probe the lanthanide ions doped inside a matrix resonant XPS is a favorable method when compared to the energy-dependent XPS.

In chapter six lead-based quantum dots have been explored as bioimaging agents. This chapter explains in detail the four different surface modifications employed to disperse the QDs in water and various aqueous media. The crosslinked polymer-coated QDs exhibit the best stability in all kinds of buffers and in serum-supplemented growth media. This kind of stability was not observed before with lead-based nanocrystals. The luminescence and colloidal stability of the QDs was retained in buffers and serum-supplemented growth media for 7 months which is a remarkable improvement over 7 days observed by Hinds *et al.*[211]

7.2 Future Outlook

As it is observed, the current optical properties of lanthanides are not particularly suitable for deep-tissue imaging with TPULSM. The long lifetimes of lanthanides have to be shortened so that the number of photocycles can be increased. This result in the increase the number of photons released per second thereby augumenting the quantum yield. The radiative rates of the lanthanides can be increased by coupling the nanocrystals to nobel metal nanocrystals such as gold and silver. This has been reported for europium complexes by Lakowitz.[223] Polman and coworkers have shown that the luminescence intensity of 980 nm emission from Er^{3+} ions could be increased by factor of 450.[224] This was shown on thin films of Er^{3+} ions and gold islands separated by a distance of 35 nm.

So the same could possibly be achieved by coupling lanthanide doped nanocrystals with gold or silver nanocrystals. To achieve the goal of increasing the radiative rates, following are the conditions which should be achieved.

1) The distance between the gold and lanthanide nanocrystals has to be controlled and it is imperative that the optimum distance (5 to 15 nm) between them is found out.

2) The emission from the lanthanides has to be resonant with the surface plasmons of the gold so that the surface plasmons would increase the radiative rates of the lanthanides without quenching. If sensitized quenching with Yb^{3+} ions is employed then the radiative rates of Yb^{3+} ions should also be increased so that it would influence the overall process.

3) All the lanthanide ions have to be within the optimum distance from the gold nanocrystals to achieve the maximum effect.

4) The size and shape of gold nanocrystals is important as it decides the surface plamson resonance wavelength.

The other interesting study to take this work forward is the detailed study of resonant XPS on various lanthanides as dopants and as matrices. This might shed light on how they get doped inside a matrix like $NaYF_4$. This would also shed light on the growth of these nanocrystals which could potentially improve their physical properties. Furthermore the appearance of the new doublet for yttrium ions should be investigated in detail to understand why there is a size dependence behavior. A systematic study of different sizes

of $NaYF_4$ nanocrystals raging from 5 to 30 nm with variable energy-dependent XPS along with HAADF, and HRTEM will be useful in explaining the size dependence behavior.

The crosslinking strategy to disperse the both lanthanide doped nanocrystals and the QDs are quite effective. However the crosslinked polymer-coated nanocrystals are not stable in presence of calcium and magnesium salts which are present in blood of small animals. This is due to the large number of carboxylic acid groups from opening the anhydride rings present in PMAO. The carboxylic acid groups have to be quenched so that the interaction between divalent cations and the polymer are reduced to a minimum. This could be achieved through two ways.

1) Coat the QDs or lanthanide doped nanocrystals with the crosslinked polymer. Following this convert the carboxylic acid groups to an activated ester using either DCC or EDC coupling agent. The activated ester could be reacted with a small amine molecule to form the amide bond. This could in principle be used for controlling the surface charge of the nanocrystals. The surface charge of the nanocrystals plays a vital role in avoiding non-specific binding.
2) The anhydride rings are opened using amine molecules to form amides and carboxylic acid groups. If the rings are closed again it would result in an imide which is a more stable than the anhydride rings in water and various pH conditions.

In case of QDs a shell of ZnS has to be grown to reduce the toxicity of these QDs. There is one report in which they have grown a shell of ZnS over a PbS/CdS core/shell QD. The

authors add that the ZnS shell growth is a preliminary study and further investigation is necessary to optimize the shell growth. The other study which should be undertaken is to study the structure of PbS/CdS/ZnS using energy-dependent XPS. This will shed light on the growth and the structure of ZnS shell over the core/shell QDs. It could be speculated that the ZnS shell grown need not be a shell, but could convert the core/shell QDs to an alloy structure. Furthermore the analysis of the structure will reveal whether the core/shell structure exists after the ZnS shell growth.

Bibliography

(1) Medintz, I. L.; Uyeda, H. T.; Goldman, E. R.; Mattoussi, H. *Nat. Mater.* **2005**, *4*, 435.

(2) Nirmal, M.; Brus, L. *Acc. Chem. Res.* **1999**, *32*, 407.

(3) Raymond, K. N.; Pierre, V. C. *Bioconjugate Chem.* **2005**, *16*, 3.

(4) Trindade, T.; O'Brien, P.; Pickett, N. L. *Chem. Mater.* **2001**, *13*, 3843.

(5) Wang, F.; Liu, X. G. *Chem. Soc. Rev.* **2009**, *38*, 976.

(6) Whitesides, G. M. *Small* **2005**, *1*, 172.

(7) Tseng, G. Y.; Ellenbogen, J. C. *Science* **2001**, *294*, 1293.

(8) Schmid, G. *Chem. Rev.* **1992**, *92*, 1709.

(9) Schmid, G.; Corain, B. *Eur. J. Inorg. Chem.* **2003**, *2003*, 3081.

(10) Turkevich, J.; Stevenson, P. C.; Hillier, J. *Discuss. Faraday Soc.* **1951**, *11*, 55.

(11) Feynman, R. P. *Engineering and Science* **1960**, *23*, 22.

(12) Graham-Rowe, D. *Nature Photon.* **2009**, *3*, 307.

(13) Rosi, N. L.; Mirkin, C. A. *Chem. Rev.* **2005**, *105*, 1547.

(14) Laurent, S.; Forge, D.; Port, M.; Roch, A.; Robic, C.; Elst, L. V.; Muller, R. N. *Chem. Rev.* **2008**, *108*, 2064.

(15) Johnson, N. J. J.; Oakden, W.; Stanisz, G. J.; Prosser, R. S.; van Veggel, F. C. J. M. *Chem. Mater.* **2011**, *23*, 3714.

(16) Michalet, X.; Pinaud, F. F.; Bentolila, L. A.; Tsay, J. M.; Doose, S.; Li, J. J.; Sundaresan, G.; Wu, A. M.; Gambhir, S. S.; Weiss, S. *Science* **2005**, *307*, 538.

(17) So, P. T. C.; Dong, C. Y.; Masters, B. R.; Berland, K. M. *Annu. Rev. Biomed. Eng.* **2000**, *2*, 399.

(18) Albota, M.; Beljonne, D.; Bredas, J. L.; Ehrlich, J. E.; Fu, J. Y.; Heikal, A. A.; Hess, S. E.; Kogej, T.; Levin, M. D.; Marder, S. R.; McCord-Maughon, D.; Perry, J. W.; Rockel, H.; Rumi, M.; Subramaniam, C.; Webb, W. W.; Wu, X. L.; Xu, C. *Science* **1998**, *281*, 1653.

(19) Giepmans, B. N. G.; Adams, S. R.; Ellisman, M. H.; Tsien, R. Y. *Science* **2006**, *312*, 217.

(20) Kawano, H.; Kogure, T.; Abe, Y.; Mizuno, H.; Miyawaki, A. *Nat. Methods* **2008**, *5*, 373.

(21) Denk, W.; Svoboda, K. *Neuron* **1997**, *18*, 351.

(22) Helmchen, F.; Denk, W. *Nat. Methods* **2005**, *2*, 932.

(23) Denk, W.; Strickler, J. H.; Webb, W. W. *Science* **1990**, *248*, 73.

(24) Polman, A. *Physica B* **2001**, *300*, 78.

(25) Burzo, E. *Rep. Prog. Phys* **1998**, *61*, 1099.

(26) Lauffer, R. B. *Chem. Rev.* **1987**, *87*, 901.

(27) Gschneidner, K. A.; Eyring, L. In *Handbook on the Physics and Chemistry of Rare Earths*; Elsevier North-Holland: Amsterdam, 1982; Vol. 5.

(28) Cotton, S. *Lanthanides and Actinides*; Macmillan Education Ltd, 1991.

(29) Hou, Z. M.; Luo, Y. J.; Li, X. F. *J. Organomet. Chem.* **2006**, *691*, 3114.

(30) Balda, R.; Fernandez, J.; de Ocariz, I. S.; Voda, M.; Garcia, A. J.; Khaidukov, N. *Phys. Rev. B* **1999**, *59*, 9972.

(31) Fernandez, J.; Sanz, M.; Mendioroz, A.; Balda, R.; Chaminade, J. P.; Ravez, J.; Lacha, L. M.; Voda, M.; Arriandiaga, M. A. *J. Alloys Compd.* **2001**, *323*, 267.

(32) Wang, X.; Kong, X. G.; Shan, G. Y.; Yu, Y.; Sun, Y. J.; Feng, L. Y.; Chao, K. F.; Lu, S. Z.; Li, Y. J. *J. Phys. Chem. B* **2004**, *108*, 18408.

(33) Capobianco, J. A.; Vetrone, F.; Boyer, J. C.; Speghini, A.; Bettinelli, M. *J. Phys. Chem. B* **2002**, *106*, 1181.

(34) Capobianco, J. A.; Vetrone, F.; Boyer, J. C.; Speghini, A.; Bettinelli, M. *Opt. Mater.* **2002**, *19*, 259.

(35) Auzel, F. E. *Proc. IEEE* **1973**, *61*, 758.

(36) Vetrone, F.; Boyer, J. C.; Capobianco, J. A.; Speghini, A.; Bettinelli, M. *J. Phys. Chem. B* **2003**, *107*, 1107.

(37) Vetrone, F.; Boyer, J. C.; Capobianco, J. A.; Speghini, A.; Bettinelli, M. *J. Appl. Phys.* **2004**, *96*, 661.

(38) Boyer, J. C.; Vetrone, F.; Capobianco, J. A.; Speghini, A.; Bettinelli, M. *Chem. Phys. Lett.* **2004**, *390*, 403.

(39) Carnall, W. T.; Goodman, G. L.; Rajnak, K.; Rana, R. S. *J. Chem. Phys.* **1989**, *90*, 3443.

(40) Nakazawa, E.; Shionoya, S. *Phys. Rev. Lett.* **1970**, *25*, 1710.

(41) Salley, G. M.; Valiente, R.; Güdel, H. U. *J. Lumin.* **2001**, *94*, 305.

(42) Salley, G. M.; Valiente, R.; Güdel, H. U. *Phys. Rev. B* **2003**, *67*, 134111.

(43) Maciel, G. S.; Biswas, A.; Prasad, P. N. *Opt. Commun.* **2000**, *178*, 65.

(44) Ostermayer, F. W.; van Uitert, L. G. *Phys. Rev. B* **1970**, *1*, 4208.

(45) Chivian, J. S.; Case, W. E.; Eden, D. D. *Appl. Phys. Lett.* **1979**, *35*, 124.

(46) Krasutsky, N. J.; Case, W. E.; Chivian, J. S. *J. Appl. Phys.* **1979**, *50*, 3142.

(47) Auzel, F.; Chen, Y. H.; Meichenin, D. *J. Lumin.* **1994**, *60-1*, 692.

(48) Scheife, H.; Huber, G.; Heumann, E.; Bar, S.; Osiac, E. *Opt. Mater.* **2004**, *26*, 365.

(49) Sivakumar, S.; van Veggel, F. C. J. M.; May, P. S. *J. Am. Chem. Soc.* **2007**, *129*, 620.

(50) Wang, F.; Banerjee, D.; Liu, Y. S.; Chen, X. Y.; Liu, X. G. *Analyst* **2010**, *135*, 1839.

(51) Auzel, F. *Chem. Rev.* **2004**, *104*, 139.

(52) Wang, G. F.; Peng, Q.; Li, Y. D. *Acc. Chem. Res.* **2011**, *44*, 322.

(53) Sudarsan, V.; van Veggel, F. C. J. M.; Herring, R. A.; Raudsepp, M. *J. Mater. Chem.* **2005**, *15*, 1332.

(54) Stöber, W.; Fink, A.; Bohn, E. *J. Colloid Interface Sci.* **1968**, *26*, 62.

(55) Sudarsan, V.; Sivakumar, S.; van Veggel, F. C. J. M.; Raudsepp, M. *Chem. Mater.* **2005**, *17*, 4736.

(56) Wang, Z. L.; Quan, Z. W.; Lin, J.; Fang, J. Y. *J. Nanosci. Nanotechnol.* **2005**, *5*, 1532.

(57) Wei, Y.; Lu, F. Q.; Zhang, X. R.; Chen, D. P. *Mater. Lett.* **2007**, *61*, 1337.

(58) Wei, Y.; Lu, F. Q.; Zhang, X. R.; Chen, D. P. *J. Alloys Compd.* **2008**, *455*, 376.

(59) Liu, J. F.; Li, Y. D. *J. Mater. Chem.* **2007**, *17*, 1797.

(60) Wang, X.; Li, Y. D. *Chem. Eur. J.* **2003**, *9*, 5627.

(61) Wang, X.; Zhuang, J.; Peng, Q.; Li, Y. D. *Nature* **2005**, *437*, 121.

(62) Wang, X.; Zhuang, J.; Peng, Q.; Li, Y. D. *Inorg. Chem.* **2006**, *45*, 6661.

(63) Boyer, J. C.; Cuccia, L. A.; Capobianco, J. A. *Nano Lett.* **2007**, *7*, 847.

(64) Boyer, J. C.; Gagnon, J.; Cuccia, L. A.; Capobianco, J. A. *Chem. Mater.* **2007**, *19*, 3358.

(65) Boyer, J. C.; Vetrone, F.; Cuccia, L. A.; Capobianco, J. A. *J. Am. Chem. Soc.* **2006**, *128*, 7444.

(66) Mai, H. X.; Zhang, Y. W.; Si, R.; Yan, Z. G.; Sun, L. D.; You, L. P.; Yan, C. H. *J. Am. Chem. Soc.* **2006**, *128*, 6426.

(67) Mai, H. X.; Zhang, Y. W.; Sun, L. D.; Yan, C. H. *J. Phys. Chem. C.* **2007**, *111*, 13721.

(68) Ye, X. C.; Collins, J. E.; Kang, Y. J.; Chen, J.; Chen, D. T. N.; Yodh, A. G.; Murray, C. B. *Proc. Natl. Acad. Sci. U. S. A.* **2010**, *107*, 22430.

(69) Li, Z. Q.; Zhang, Y. *Nanotechnology* **2008**, *19*, 345606.

(70) Li, Z. Q.; Zhang, Y.; Jiang, S. *Adv. Mater.* **2008**, *20*, 4765.

(71) Menyuk, N.; Pierce, J. W.; Dwight, K. *Appl. Phys. Lett.* **1972**, *21*, 159.

(72) Johnson, N. J. J.; Oakden, W.; Stanisz, G. J.; Prosser, R. S.; van Veggel, F. C. J. M. *Chem. Mater.* **2011**, *23*, 3714.

(73) Li, C. X.; Yang, J.; Yang, P. P.; Zhang, X. M.; Lian, H. Z.; Lin, J. *Cryst. Growth Des.* **2008**, *8*, 923.

(74) Mahalingam, V.; Vetrone, F.; Naccache, R.; Speghini, A.; Capobianco, J. A. *Adv. Mater.* **2009**, *21*, 4025.

(75) Scholes, G. D.; Rumbles, G. *Nat. Mater.* **2006**, *5*, 683.

(76) Sze, S. M.; Ng, K. K. *Physics of Semiconductor Devices*; John Wiley & Sons, Inc.: New Jersey, 2007.

(77) Klimov, V. I. *Nanocrystal Quantum Dots*; Taylor and Francis Group, LLC: Boca Raton, 2010.

(78) Klimov, V. I. *Annu. Rev. Phys. Chem.* **2007**, *58*, 635.

(79) Carbone, L.; Cozzoli, P. D. *Nano Today* **2010**, *5*, 449.

(80) Choi, C. L.; Alivisatos, A. P. *Annu. Rev. Phys. Chem.* **2010**, *61*, 369.

(81) Scholes, G. D. *Adv. Func. Mater.* **2008**, *18*, 1157.

(82) Wise, F. W. *Acc. Chem. Res.* **2000**, *33*, 773.

(83) Murray, C. B.; Norris, D. J.; Bawendi, M. G. *J. Am. Chem. Soc.* **1993**, *115*, 8706.

(84) Borrelli, N. F.; Smith, D. W. *J. Non-Cryst. Solids* **1994**, *180*, 25.

(85) Olkhovets, A.; Hsu, R. C.; Lipovskii, A.; Wise, F. W. *Phys. Rev. Lett.* **1998**, *81*, 3539.

(86) Chithrani, D.; Williams, R. L.; Lefebvre, J.; Poole, P. J.; Aers, G. C. *Appl. Phys. Lett.* **2004**, *84*, 978.

(87) Skolnick, M. S.; Mowbray, D. J. *Ann. Rev. Mater. Res.* **2004**, *34*, 181.

(88) Talapin, D. V.; Lee, J.-S.; Kovalenko, M. V.; Shevchenko, E. V. *Chem. Rev.* **2009**, *110*, 389.

(89) Alivisatos, A. P. *Science* **1996**, *271*, 933.

(90) Alivisatos, A. P. *J. Phys. Chem. C* **1996**, *100*, 13226.

(91) Reiss, P.; Protiere, M.; Li, L. *Small* **2009**, *5*, 154.

(92) Underwood, D. F.; Kippeny, T.; Rosenthal, S. J. *J. Phys. Chem. B* **2001**, *105*, 436.

(93) Zhang, J. Z. *J. Phys. Chem. B* **2000**, *104*, 7239.

(94) Murray, C. B.; Norris, D. J.; Bawendi, M. G. *J. Am. Chem. Soc.* **1993**, *115*, 8706.

(95) Dabbousi, B. O.; Rodriguez-Viejo, J.; Mikulec, F. V.; Heine, J. R.; Mattoussi, H.; Ober, R.; Jensen, K. F.; Bawendi, M. G. *J. Phys. Chem. B* **1997**, *101*, 9463.

(96) Li, J. J.; Wang, Y. A.; Guo, W. Z.; Keay, J. C.; Mishima, T. D.; Johnson, M. B.; Peng, X. G. *J. Am. Chem. Soc.* **2003**, *125*, 12567.

(97) Son, D. H.; Hughes, S. M.; Yin, Y.; Alivisatos, A. P. *Science* **2004**, *306*, 1009.

(98) Pietryga, J. M.; Werder, D. J.; Williams, D. J.; Casson, J. L.; Schaller, R. D.; Klimov, V. I.; Hollingsworth, J. A. *J. Am. Chem. Soc.* **2008**, *130*, 4879.

(99) Abel, K. A.; FitzGerald, P. A.; Wang, T. Y.; Regier, T. Z.; Raudsepp, M.; Ringer, S. P.; Warr, G. G.; van Veggel, F. C. J. M. *J. Phys. Chem. C* **2012**, *116*, 3968.

(100) Larson, D. R.; Zipfel, W. R.; Williams, R. M.; Clark, S. W.; Bruchez, M. P.; Wise, F. W.; Webb, W. W. *Science* **2003**, *300*, 1434.

(101) Pichaandi, J.; van Veggel, F. C. J. M.; Raudsepp, M. *ACS Appl. Mater. Interfaces* **2010**, *2*, 157.

(102) Auzel, F.; Pecile, D. *J. Lumin.* **1973**, *8*, 32.

(103) Joubert, M. F. *Opt. Mater.* **1999**, *11*, 181.

(104) Pandozzi, F.; Vetrone, F.; Boyer, J. C.; Naccache, R.; Capobianco, J. A.; Speghini, A.; Bettinelli, M. *J. Phys. Chem. B* **2005**, *109*, 17400.

(105) Rapaport, A.; Milliez, J.; Szipocs, F.; Bass, M.; Cassanho, A.; Jenssen, H. *Appl. Opt.* **2004**, *43*, 6477.

(106) Sivakumar, S.; Diamente, P. R.; van Veggel, F. C. J. M. *Chem. Eur. J.* **2006**, *12*, 5878.

(107) Auzel, F.; Pecile, D. *J. Lumin.* **1976**, *11*, 321.

(108) Suyver, J. F.; Aebischer, A.; Biner, D.; Gerner, P.; Grimm, J.; Heer, S.; Kramer, K. W.; Reinhard, C.; Gudel, H. U. *Opt. Mater.* **2005**, *27*, 1111.

(109) Bazzi, R.; Brenier, A.; Perriat, P.; Tillement, O. *J. Lumin.* **2005**, *113*, 161.

(110) Aebischer, A.; Heer, S.; Biner, D.; Kramer, K.; Haase, M.; Güdel, H. U. *Chem. Phys. Lett.* **2005**, *407*, 124.

(111) Bril, A.; Sommerdijk, J. L.; De Jager, A. W. *J. Electrochem. Soc.* **1975**, *122*, 660.

(112) Dong, B.; Song, H. W.; Yu, H. Q.; Zhang, H.; Qin, R. F.; Bai, X.; Pan, G. H.; Lu, S. Z.; Wang, F.; Fan, L. B.; Dai, Q. L. *J. Phys. Chem. C* **2008**, *112*, 1435.

(113) Heer, S.; Kompe, K.; Güdel, H. U.; Haase, M. *Adv. Mater.* **2004**, *16*, 2102.

(114) Li, Z. Q.; Zhang, Y. *Angew. Chem.* **2006**, *45*, 7732.

(115) Yi, G. S.; Chow, G. M. *Adv. Funct. Mater.* **2006**, *16*, 2324.

(116) Chatteriee, D. K.; Rufalhah, A. J.; Zhang, Y. *Biomaterials* **2008**, *29*, 937.

(117) Das, G. K.; Tan, T. T. Y. *J. Phys. Chem. C* **2008**, *112*, 11211.

(118) Diamente, P. R.; Burke, R. D.; van Veggel, F. C. J. M. *Langmuir* **2006**, *22*, 1782.

(119) Downing, E.; Hesselink, L.; Ralston, J.; Macfarlane, R. *Science* **1996**, *273*, 1185.

(120) Jalil, R. A.; Zhang, Y. *Biomaterials* **2008**, *29*, 4122.

(121) Mahalingam, V.; Mangiarini, F.; Vetrone, F.; Venkatramu, V.; Bettinelli, M.; Speghini, A.; Capobianco, J. A. *J. Phys. Chem. C* **2008**, *112*, 17745.

(122) Schäfer, H.; Ptacek, P.; Zerzouf, O.; Haase, M. *Adv. Funct. Mater.* **2008**, *18*, 2913.

(123) Sivakumar, S.; van Veggel, F. C. J. M.; Raudsepp, M. *J. Am. Chem. Soc.* **2005**, *127*, 12464.

(124) Zhao, J.; Sun, Y.; Kong, X.; Tian, L.; Wang, Y.; Tu, L.; Zhao, J.; Zhang, H. *J. Phys. Chem. B* **2008**, *112*, 15666.

(125) Li, Y. H.; Hong, G. Y.; Zhang, Y. M.; Yu, Y. M. *J. Alloys Compd.* **2008**, *456*, 247.

(126) Boyer, J. C.; Vetrone, F.; Capobianco, J. A.; Speghini, A.; Bettinelli, M. *J. Appl. Phys.* **2003**, *93*, 9460.

(127) Boyer, J. C.; Vetrone, F.; Capobianco, J. A.; Speghini, A.; Zambelli, M.; Bettinelli, M. *J. Lumin.* **2004**, *106*, 263.

(128) Naccache, R.; Vetrone, F.; Mahalingam, V.; Cuccia, L. A.; Capobianco, J. A. *Chem. Mater.* **2009**, *21*, 717.

(129) Yi, G. S.; Chow, G. M. *J. Mater. Chem.* **2005**, *15*, 4460.

(130) Lisiecki, R.; Dominiak-Dzik, G.; Ryba-Romanowski, W.; Lukasiewicz, T. *J. Appl. Phys.* **2004**, *96*, 6323.

(131) Sangeetha, N. M.; van Veggel, F. C. J. M. *J. Phys. Chem. C* **2009**, *113*, 14702.

(132) Kumar, G. A.; Chen, C. W.; Ballato, J.; Riman, R. E. *Chem. Mater.* **2007**, *19*, 1523.

(133) Bahtat, A.; deLucas, M. C. M.; Jacquier, B.; Varrel, B.; Bouazaoui, M.; Mugnier, J. *Opt. Mater.* **1997**, *7*, 173.

(134) Xiang, Q.; Zhou, Y.; Ooi, B. S.; Lam, Y. L.; Chan, Y. C.; Kam, C. H. *Thin Solid Films* **2000**, *370*, 243.

(135) Zampedri, L.; Ferrari, M.; Armellini, C.; Visintainer, F.; Tosello, C.; Ronchin, S.; Rolli, R.; Montagna, M.; Chiasera, A.; Pelli, S.; Righini, G. C.; Monteil, A.; Duverger, C.; Goncalves, R. R. *J. Sol-Gel. Sci. Technol.* **2003**, *26*, 1033.

(136) Dong, C.; Raudsepp, M.; van Veggel, F. C. J. M. *J. Phys. Chem. C* **2009**, *113*, 472.

(137) Liang, D. T.; Readey, D. W. *J. Am. Ceram. Soc.* **1987**, *70*, 570.

(138) Pichaandi, J.; Boyer, J. C.; Delaney, K. R.; van Veggel, F. C. J. M. *J. Phys. Chem. C* **2011**, *115*, 19054.

(139) Jiang, G. C.; Pichaandi, J.; Johnson, N. J. J.; Burke, R. D.; van Veggel, F. C. J. M. *Langmuir* **2012**, *28*, 3239.

(140) Wang, F.; Chatterjee, D. K.; Li, Z. Q.; Zhang, Y.; Fan, X. P.; Wang, M. Q. *Nanotechnology* **2006**, *17*, 5786.

(141) Zhuang, J. L.; Liang, L. F.; Sung, H. H. Y.; Yang, X. F.; Wu, M. M.; Williams, I. D.; Feng, S. H.; Su, Q. *Inorg. Chem.* **2007**, *46*, 5404.

(142) Bogdan, N.; Vetrone, F.; Ozin, G. A.; Capobianco, J. A. *Nano Lett.* **2011**, *11*, 835.

(143) Li, Z. Q.; Zhang, Y.; Jiang, S. *Adv. Mater.* **2008**, *20*, 4765.

(144) Nyk, M.; Kumar, R.; Ohulchanskyy, T. Y.; Bergey, E. J.; Prasad, P. N. *Nano Lett.* **2008**, *8*, 3834.

(145) Boyer, J. C.; van Veggel, F. C. J. M. *Nanoscale* **2010**, *2*, 1417.

(146) Johnson, N. J. J.; Sangeetha, N. M.; Boyer, J. C.; van Veggel, F. C. J. M. *Nanoscale* **2010**, *2*, 771.

(147) Boyer, J. C.; Manseau, M. P.; Murray, J. I.; van Veggel, F. C. J. M. *Langmuir* **2010**, *26*, 1157.

(148) Chen, Z. G.; Chen, H. L.; Hu, H.; Yu, M. X.; Li, F. Y.; Zhang, Q.; Zhou, Z. G.; Yi, T.; Huang, C. H. *J. Am. Chem. Soc.* **2008**, *130*, 3023.

(149) Cheng, L.; Yang, K.; Zhang, S.; Shao, M. W.; Lee, S. T.; Zhang, L. *Nano Res.* **2010**, *3*, 722.

(150) Yi, G. S.; Chow, G. M. *Chem. Mater.* **2007**, *19*, 341.

(151) Basiruddin, S. K.; Saha, A.; Pradhan, N.; Jana, N. R. *Langmuir* **2010**, *26*, 7475.

(152) Jana, N. R.; Patra, P. K.; Saha, A.; Basiruddin, S. K.; Pradhan, N. *J. Phys. Chem. C* **2009**, *113*, 21484.

(153) Shibasaki, Y.; Kim, B. S.; Young, A. J.; McLoon, A. L.; Ekker, S. C.; Taton, T. A. *J. Mater. Chem.* **2009**, *19*, 6324.

(154) Aldana, J.; Lavelle, N.; Wang, Y.; Peng, X. *J. Am. Chem. Soc.* **2005**, *127*, 2496.

(155) Di Corato, R.; Quarta, A.; Piacenza, P.; Ragusa, A.; Figuerola, A.; Buonsanti, R.; Cingolani, R.; Manna, L.; Pellegrino, T. *J. Mater. Chem.* **2008**, *18*, 1991.

(156) Parak, W. G. J.; Lin, C. A. J.; Sperling, R. A.; Li, J. K.; Yang, T. Y.; Li, P. Y.; Zanella, M.; Chang, W. H. *Small* **2008**, *4*, 334.

(157) Qin, J.; Jo, Y. S.; Muhammed, M. *Angew. Chem. Int. Ed.* **2009**, *48*, 7845.

(158) Yu, W. W.; Chang, E.; Falkner, J. C.; Zhang, J. Y.; Al-Somali, A. M.; Sayes, C. M.; Johns, J.; Drezek, R.; Colvin, V. L. *J. Am. Chem. Soc.* **2007**, *129*, 2871.

(159) Basiruddin, S. K.; Saha, A.; Pradhan, N.; Jana, N. R. *J. Phys. Chem. C* **2010**, *114*, 11009.

(160) Pellegrino, T.; Manna, L.; Kudera, S.; Liedl, T.; Koktysh, D.; Rogach, A. L.; Keller, S.; Radler, J.; Natile, G.; Parak, W. J. *Nano Lett.* **2004**, *4*, 703.

(161) Guo, W. H.; Li, J. J.; Wang, Y. A.; Peng, X. G. *J. Am. Chem. Soc.* **2003**, *125*, 3901.

(162) Abel, K. A.; Boyer, J. C.; Andrei, C. M.; van Veggel, F. C. J. M. *J. Phys. Chem. Lett.* **2011**, *2*, 185.

(163) Abel, K. A.; Boyer, J. C.; van Veggel, F. C. J. M. *J. Am. Chem. Soc.* **2009**, *131*, 14644.

(164) Wang, Z. L.; Quan, Z. W.; Jia, P. Y.; Lin, C. K.; Luo, Y.; Chen, Y.; Fang, J.; Zhou, W.; O'Connor, C. J.; Lin, J. *Chem. Mater.* **2006**, *18*, 2030.

(165) Yang, D. M.; Li, C. X.; Li, G. G.; Shang, M. M.; Kang, X. J.; Lin, J. *J. Mater. Chem.* **2011**, *21*, 5923.

(166) Wheeler, D. H.; Potente, D.; Wittcoff, H. *J. Am. Oil Chem. Soc.* **1971**, *48*, 125.

(167) Lin, C. A. J.; Sperling, R. A.; Li, J. K.; Yang, T. Y.; Li, P. Y.; Zanella, M.; Chang, W. H.; Parak, W. G. J. *Small* **2008**, *4*, 334.

(168) Yu, W. W.; Chang, E.; Falkner, J. C.; Zhang, J. Y.; Al-Somali, A. M.; Sayes, C. M.; Johns, J.; Drezek, R.; Colvin, V. L. *J. Am. Chem. Soc.* **2007**, *129*, 2871.

(169) Gai, S. L.; Yang, P. P.; Li, C. X.; Wang, W. X.; Dai, Y. L.; Niu, N.; Lin, J. *Adv. Funct. Mater.* **2010**, *20*, 1166.

(170) Zhou, J.; Yao, L. M.; Li, C. Y.; Li, F. Y. *J. Mater. Chem.* **2010**, *20*, 8078.

(171) Xu, C.; Zipfel, W.; Shear, J. B.; Williams, R. M.; Webb, W. W. *Proc. Natl. Acad. Sci. U. S. A.* **1996**, *93*, 10763.

(172) Zipfel, W. R.; Williams, R. M.; Christie, R.; Nikitin, A. Y.; Hyman, B. T.; Webb, W. W. *Proc. Natl. Acad. Sci. U. S. A.* **2003**, *100*, 7075.

(173) Zipfel, W. R.; Williams, R. M.; Webb, W. W. *Nat. Biotechnol.* **2003**, *21*, 1368.

(174) Bharali, D. J.; Lucey, D. W.; Jayakumar, H.; Pudavar, H. E.; Prasad, P. N. *J. Am. Chem. Soc.* **2005**, *127*, 11364.

(175) Ferrara, D. E.; Weiss, D.; Carnell, P. H.; Vito, R. P.; Vega, D.; Gao, X. H.; Nie, S. M.; Taylor, W. R. *Am. J. Physiol-Reg. I.* **2006**, *290*, R114.

(176) Ferrara, D. E.; Weiss, D.; Gao, X. H.; Nie, S. M.; Taylor, W. R. *Arterioscler. Thromb. Vasc. Biol.* **2005**, *25*, E63.

(177) Fountaine, T. J.; Wincovitch, S. M.; Geho, D. H.; Garfield, S. H.; Pittaluga, S. *Mod. Pathol.* **2006**, *19*, 1181.

(178) Tu, C. Q.; Ma, X. C.; Pantazis, P.; Kauzlarich, S. M.; Louie, A. Y. *J. Am. Chem. Soc.* **2010**, *132*, 2016.

(179) Xing, Y.; Rao, J. H. *Cancer Biomarkers* **2008**, *4*, 307.

(180) Dooley, C. T.; Dore, T. M.; Hanson, G. T.; Jackson, W. C.; Remington, S. J.; Tsien, R. Y. *J. Biol. Chem.* **2004**, *279*, 22284.

(181) Mainen, Z. F.; Maletic-Savatic, M.; Shi, S. H.; Hayashi, Y.; Malinow, R.; Svoboda, K. *Methods* **1999**, *18*, 231.

(182) Shaner, N. C.; Steinbach, P. A.; Tsien, R. Y. *Nat. Methods* **2005**, *2*, 905.

(183) Li, C. X.; Lin, J. *J. Mater. Chem.* **2010**, *20*, 6831.

(184) Budijono, S. J.; Shan, J. N.; Yao, N.; Miura, Y.; Hoye, T.; Austin, R. H.; Ju, Y. G.; Prud'homme, R. K. *Chem. Mater.* **2010**, *22*, 311.

(185) Yu, M. X.; Li, F. Y.; Chen, Z. G.; Hu, H.; Zhan, C.; Yang, H.; Huang, C. H. *Anal. Chem.* **2009**, *81*, 930.

(186) Xiong, L.; Chen, Z.; Tian, Q.; Cao, T.; Xu, C.; Li, F. *Anal. Chem.* **2009**, *81*, 8687.

(187) Kobayashi, H.; Kosaka, N.; Ogawa, M.; Morgan, N. Y.; Smith, P. D.; Murray, C. B.; Ye, X. C.; Collins, J.; Kumar, G. A.; Bell, H.; Choyke, P. L. *J. Mater. Chem.* **2009**, *19*, 6481.

(188) Kumar, R.; Nyk, M.; Ohulchanskyy, T. Y.; Flask, C. A.; Prasad, P. N. *Adv. Funct. Mater.* **2009**, *19*, 853.

(189) Nyk, M.; Kumar, R.; Ohulchanskyy, T. Y.; Bergey, E. J.; Prasad, P. N. *Nano Lett.* **2008**, *8*, 3834.

(190) Schietinger, S.; Barth, M.; Alchele, T.; Benson, O. *Nano Lett.* **2009**, *9*, 1694.

(191) Kleinfeld, D.; Mitra, P. P.; Helmchen, F.; Denk, W. *Proc. Natl. Acad. Sci. U. S. A.* **1999**, *95*, 15741.

(192) Svoboda, K.; Denk, W.; Kleinfeld, D.; Tank, D. W. *Nature* **1997**, *385*, 161.

(193) Ng, D. C.; Tokuda, T.; Yamamoto, A.; Matsuo, M.; Nunoshita, M.; Tamura, H.; Ishikawa, Y.; Shiosaka, S.; Ohta, J. *Sens. Actuators, B* **2006**, *119*, 262.

(194) Kömpe, K.; Borchert, H.; Storz, J.; Lobo, A.; Adam, S.; Möller, T.; Haase, M. *Angew. Chem. Int. Ed.* **2003**, *42*, 5513.

(195) Henderson, G. S.; Baker, D. R. *Synchrotron radiation: earth, environmental and material sciences applications*; Mineralogical Association of Canada: Saskatoon, 2002; Vol. 30.

(196) Borchert, H.; Haubold, S.; Haase, M.; Weller, H. *Nano Lett.* **2002**, *2*, 151.

(197) Borchert, H.; Talapin, D. V.; McGinley, C.; Adam, S.; Lobo, A.; de Castro, A. R. B.; Möller, T.; Weller, H. *J. Chem. Phys.* **2003**, *119*, 1800.

(198) McGinley, C.; Borchert, H.; Talapin, D. V.; Adam, S.; Lobo, A.; de Castro, A. R. B.; Haase, M.; Weller, H.; Möller, T. *Phys. Rev. B* **2004**, *69*, 045301/1.

(199) Moulder, J. F.; Stickle, W. F.; Sobol, P. E.; Bomben, K. D. *Handbook of X-Ray Photoelectron Spectroscopy*; Physical Electronics, Inc.: Chanhassen, 1995.

(200) Seah, M. P.; Dench, W. A. *Surf. Interface Anal.* **1979**, *1*, 2.

(201) Dong, C. H.; Pichaandi, J.; Regier, T.; van Veggel, F. C. J. M. *Nanoscale* **2011**, *3*, 3376.

(202) Abel, K. A.; Boyer, J.-C.; van Veggel, F. C. J. M. *J. Am. Chem. Soc.* **2009**, *131*, 14644.

(203) Dong, C.; Pichaandi, J.; Regier, T.; van Veggel, F. C. J. M. *J. Phys. Chem. C* **2011**, *115*, 15950.

(204) Chan, W. C. W.; Maxwell, D. J.; Gao, X. H.; Bailey, R. E.; Han, M. Y.; Nie, S. M. *Curr. Opin. Biotechnol.* **2002**, *13*, 40.

(205) Nie, S. M. *Cytometry* **2002**, 25.

(206) Alivisatos, A. P.; Gu, W. W.; Larabell, C. *Annu. Rev. Biomed. Eng.* **2005**, *7*, 55.

(207) Zhao, H. G.; Wang, D. F.; Zhang, T.; Chaker, M.; Ma, D. L. *Chem. Commun.* **2010**, *46*, 5301.

(208) Sun, J. T.; Zhu, M. Q.; Fu, K.; Lewinski, N.; Drezek, R. A. *Int. J. Nanomed.* **2007**, *2*, 235.

(209) Zhao, H. G.; Wang, D. F.; Chaker, M.; Ma, D. L. *J. Phys. Chem. C* **2011**, *115*, 1620.

(210) Ma, Q. A.; Su, X. G. *Analyst* **2010**, *135*, 1867.

(211) Hinds, S.; Myrskog, S.; Levina, L.; Koleilat, G.; Yang, J.; Kelley, S. O.; Sargent, E. H. *J. Am. Chem. Soc.* **2007**, *129*, 7218.

(212) Lin, W.; Fritz, K.; Guerin, G.; Bardajee, G. R.; Hinds, S.; Sukhovatkin, V.; Sargent, E. H.; Scholes, G. D.; Winnik, M. A. *Langmuir* **2008**, *24*, 8215.

(213) Hyun, B. R.; Chen, H. Y.; Rey, D. A.; Wise, F. W.; Batt, C. A. *J. Phys. Chem. B* **2007**, *111*, 5726.

(214) Abel, K. A.; Shan, J. N.; Boyer, J. C.; Harris, F.; van Veggel, F. C. J. M. *Chem. Mater.* **2008**, *20*, 3794.

(215) Yu, W. W.; Falkner, J. C.; Shih, B. S.; Colvin, V. L. *Chem. Mater.* **2004**, *16*, 3318.

(216) Zhao, H. G.; Chaker, M.; Ma, D. L. *Phys. Chem. Chem. Phys.* **2010**, *12*, 14754.

(217) Gerion, D.; Pinaud, F.; Williams, S. C.; Parak, W. J.; Zanchet, D.; Weiss, S.; Alivisatos, A. P. *J. Phys. Chem. B* **2001**, *105*, 8861.

(218) Joo, S. H.; Park, J. Y.; Tsung, C. K.; Yamada, Y.; Yang, P. D.; Somorjai, G. A. *Nat. Mater.* **2009**, *8*, 126.

(219) Darbandi, M.; Lu, W. G.; Fang, J. Y.; Nann, T. *Langmuir* **2006**, *22*, 4371.

(220) Koole, R.; van Schooneveld, M. M.; Hilhorst, J.; Donegá, C. D.; 't Hart, D. C.; van Blaaderen, A.; Vanmaekelbergh, D.; Meijerink, A. *Chem. Mater.* **2008**, *20*, 2503.

(221) Tan, T. T.; Selvan, S. T.; Zhao, L.; Gao, S. J.; Ying, J. Y. *Chem. Mater.* **2007**, *19*, 3112.

(222) Ranucci, E.; Macchi, L.; Annunziata, R.; Ferruti, P.; Chiellini, F. *Macromol. Biosci.* **2004**, *4*, 706.

(223) Lakowicz, J. R. *Principles of Fluorescence Spectroscopy*; Springer: Newyork, 2006.

(224) Verhagen, E.; Kuipers, L.; Polman, A. *Opt. Express* **2009**, *17*, 14586.

Appendix

Appendix A. : Supporting information for chapter 2

Appendix B. : Supporting information for chapter 3

Appendix C. : Supporting information for chapter 4

Appendix D. : Supporting information for chapter 5

Appendix E. : Supporting information for chapter 6

Appendix A. : Supporting information for chapter 2

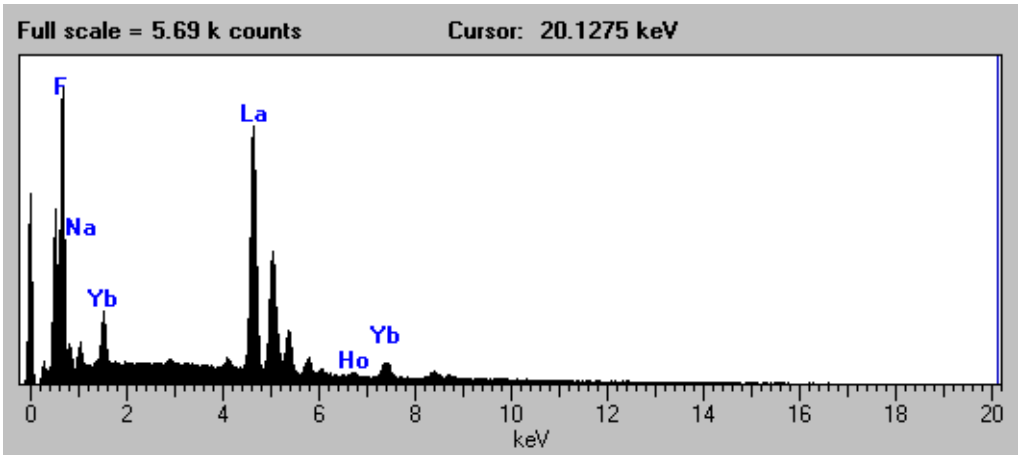

Figure A.1. EDS Spectrum of $La_{0.76}Yb_{0.22}Ho_{0.02}F_3$

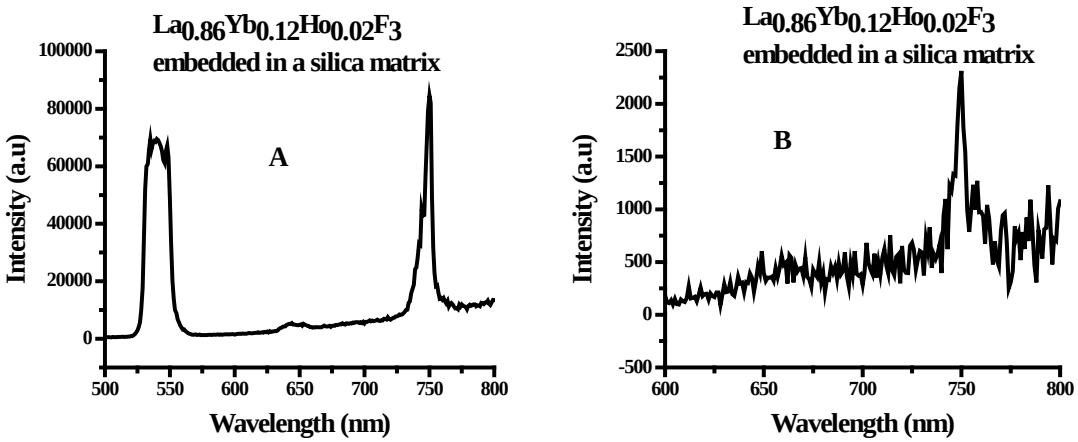

Figure A.2. (A) Green and 750 nm emission obtained by exciting Ho^{3+} ions directly at 450 nm using an OPO laser. The experiment was done at 2 nm resolution with a 495 nm filter to block the excitation light. The ratio of 540 nm to 750 nm is different in this case due to the direct excitation of Ho^{3+}ions; (B) 750 nm emission observed by direct excitation of $^5S_2$ (540 nm) using an OPO laser. The experiment was done at 2 nm resolution with a 590 nm filter to block the excitation light.

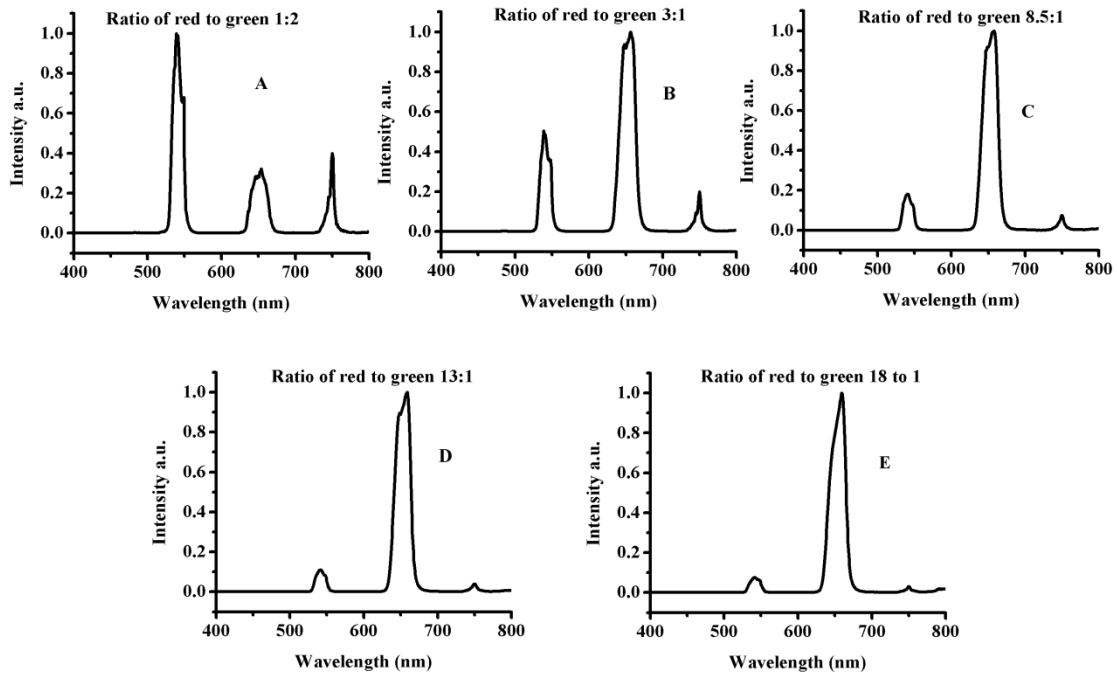

Figure A.3. Different Red to green ratio seen in upconversion luminescence from samples of the same composition ($La_{0.86}Yb_{0.12}Ho_{0.02}F_3$ embedded in a silica matrix).

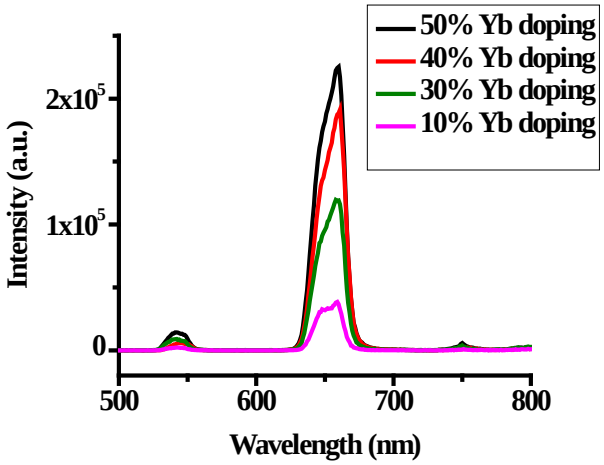

Figure A.4. Upconversion spectra for various Yb concentrations of $La_{1-x-0.02}Yb_xHo_{0.02}$ particles embedded in a silica matrix.

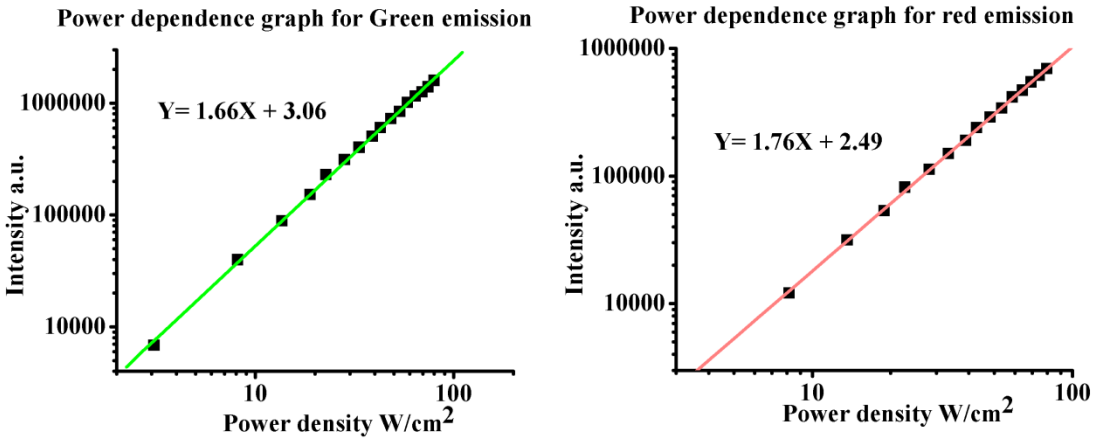

Figure A.5. Power Dependence Curve for (A) Green emission from $La_{0.76}Yb_{0.22}Ho_{0.02}F_3$ embedded in a silica matrix (sample 1); (B) Red emission from $La_{0.76}Yb_{0.22}Ho_{0.02}F_3$ embedded in a silica matrix (sample 6).

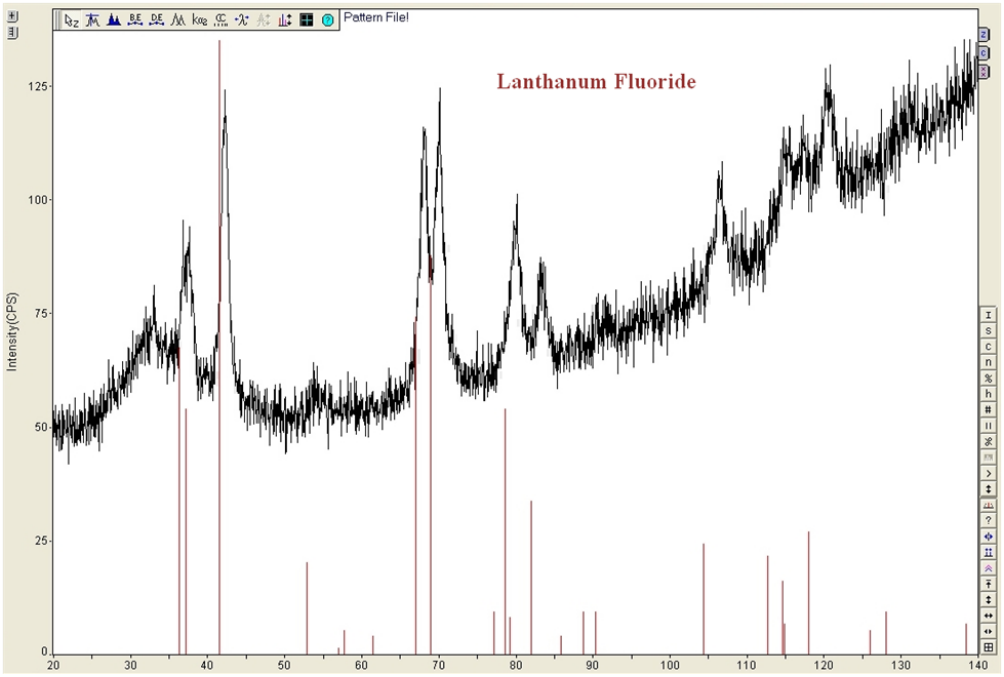

Figure A.6. XRD of baked $La_{0.76}Yb_{0.22}Ho_{0.02}F_3$ nanoparticles embedded in a silica matrix after complete etching (enhanced red emission before etching). The red sticks correspond to LaF_3 (P-3c1) JCPDS- 00-032-0483.

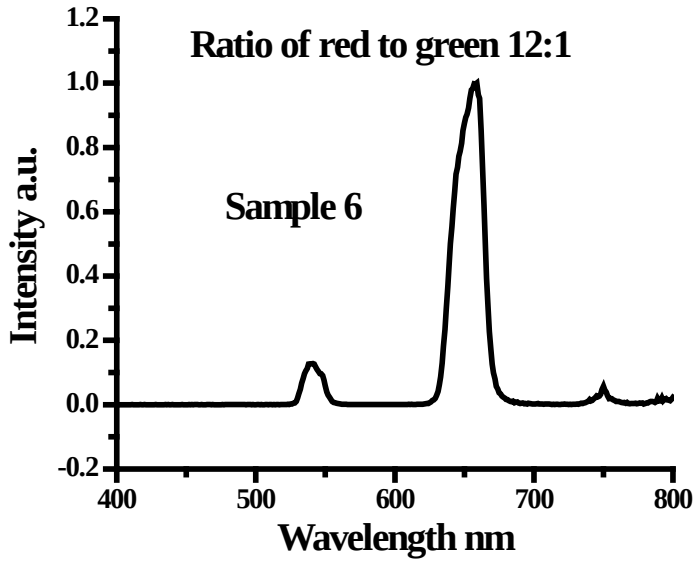

Figure A.7. Upconversion luminescence from $La_{0.76}Yb_{0.22}Ho_{0.02}F_3$ nanoparticles embedded in a silica matrix after partial etching with HF.

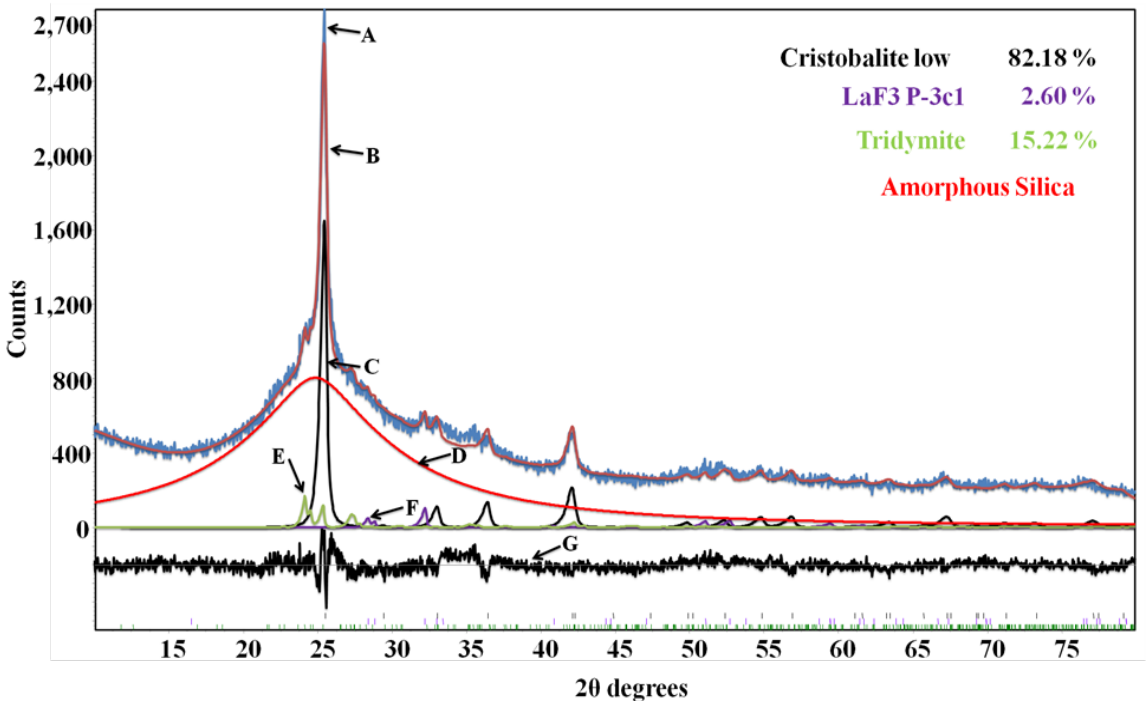

Figure A.8. XRD of baked $La_{0.86}Yb_{0.12}Ho_{0.02}F_3$ nanoparticles embedded in a silica matrix (enhanced red emission) ratio of red to green 13:1 (Sample D in Fig. S2) A) Observed Pattern, B) Calculated pattern, C) Cristobalite D) Amorphous Silica, E) Tridymite F) LaF_3 P-3c1, G) Residual curve. The weight percent does not include amorphous silica.

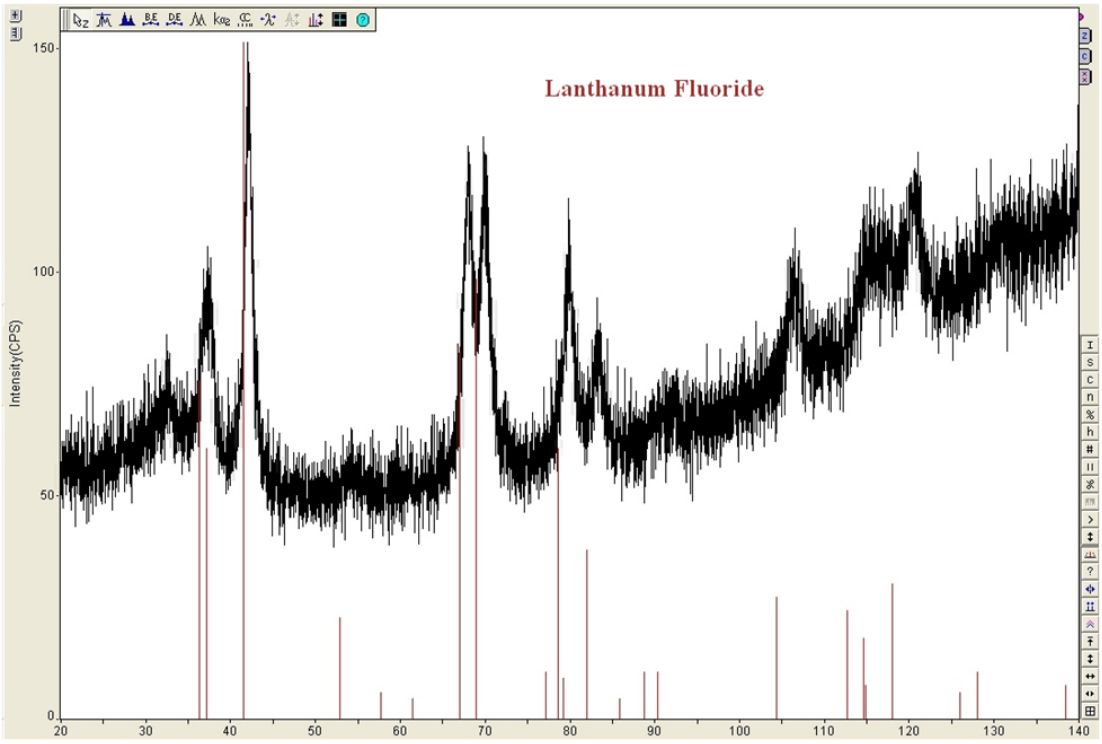

Figure A.9. XRD of baked $La_{0.76}Yb_{0.22}Ho_{0.02}F_3$ nanoparticles embedded in a silica matrix after complete etching (enhanced green emission before etching). The red sticks correspond to LaF_3 (P-3c1) JCPDS- 00-032-0483.

Appendix B. : Supporting information for chapter 3

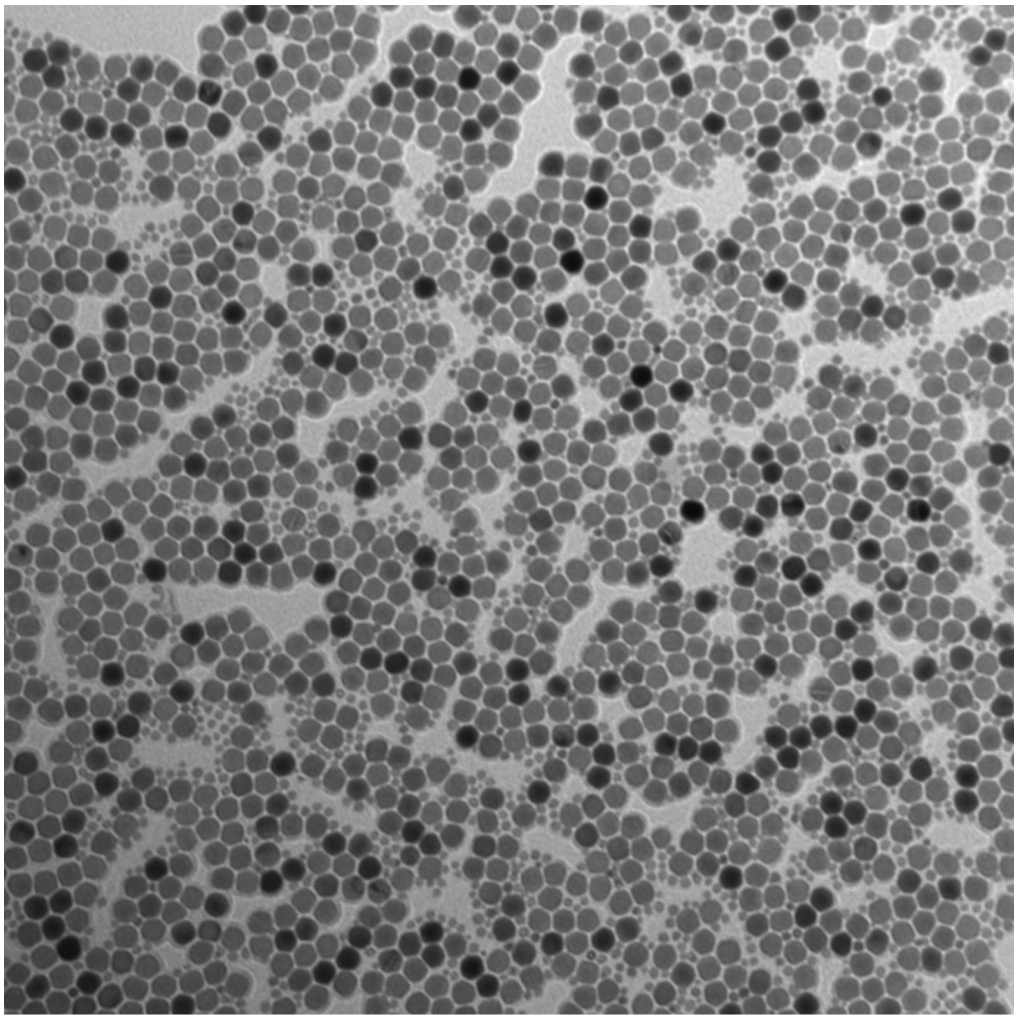

Figure B.1. TEM of Core/shell; $NaYF_4$:Yb(20%):Tm(2%)/$NaYF_4$.

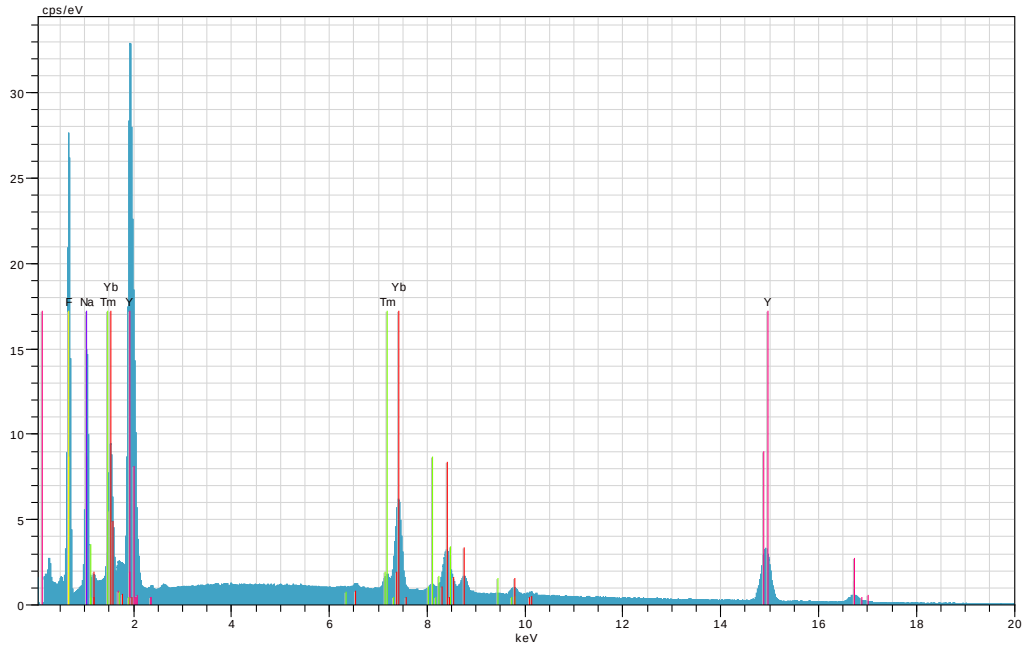

Figure B.2. EDS measurements showing the peaks of lanthanide elements and sodium in a Core/shell; $NaYF_4$:Yb(20%):Tm(2%)/$NaYF_4$:Yb(20%):Tm(2%) nanocrystals. The ratio between Yb^{3+} and Tm^{3+} ions is around 10:1. The ratio between Yb^{3+} and Y^{3+} ions is around 1:4. The ratios between lanthanide elements in the nanocrystal show that it is close to what was added in the reaction flask.

1 wt% dispersion 0.5 wt% dispersion

Figure B.3. Photographs of water dispersible core/shell/shell; NaYF4:Yb(20%):Tm(2%)/$NaYF_4$: Yb(20%):Tm(2%)/$NaYF_4$ nanocrystals.

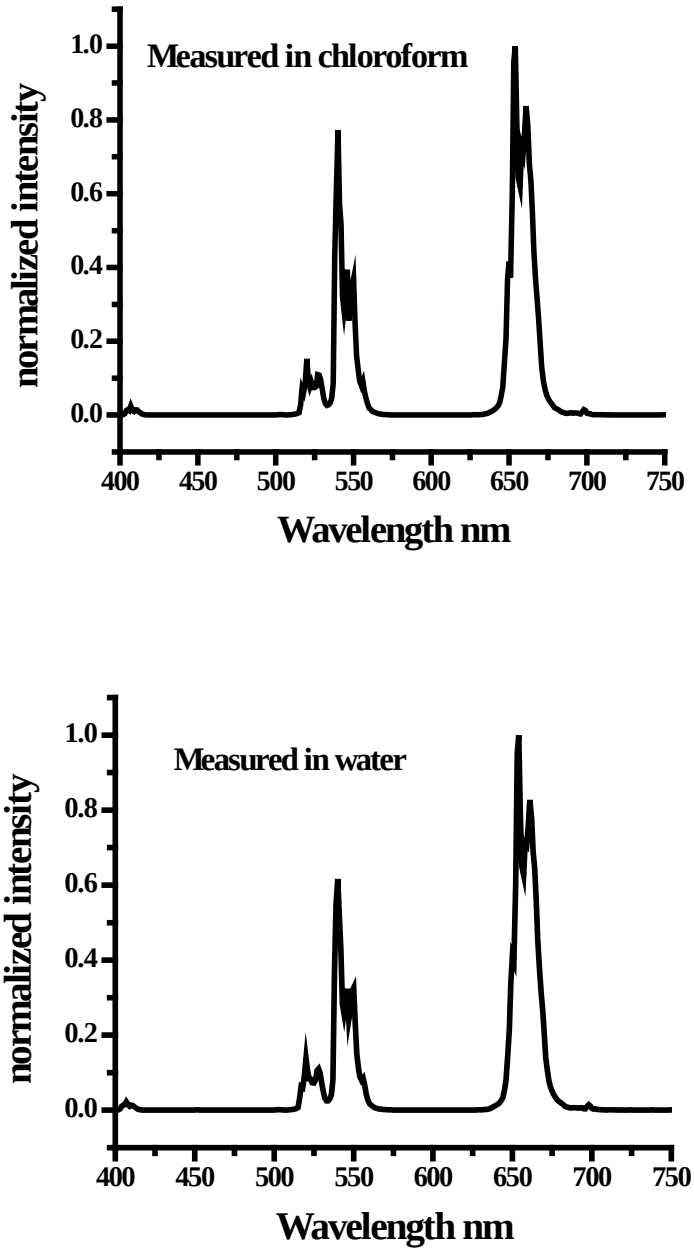

Figure B.4. Upconversion spectra for oleate-stabilized (top) and PEG-oleate coated (bottom) $NaYF_4$:Yb(20%):Er(2%) in chloroform (top) and Water (bottom), upon 980 nm excitation. The power density employed was 150 W/cm^2.

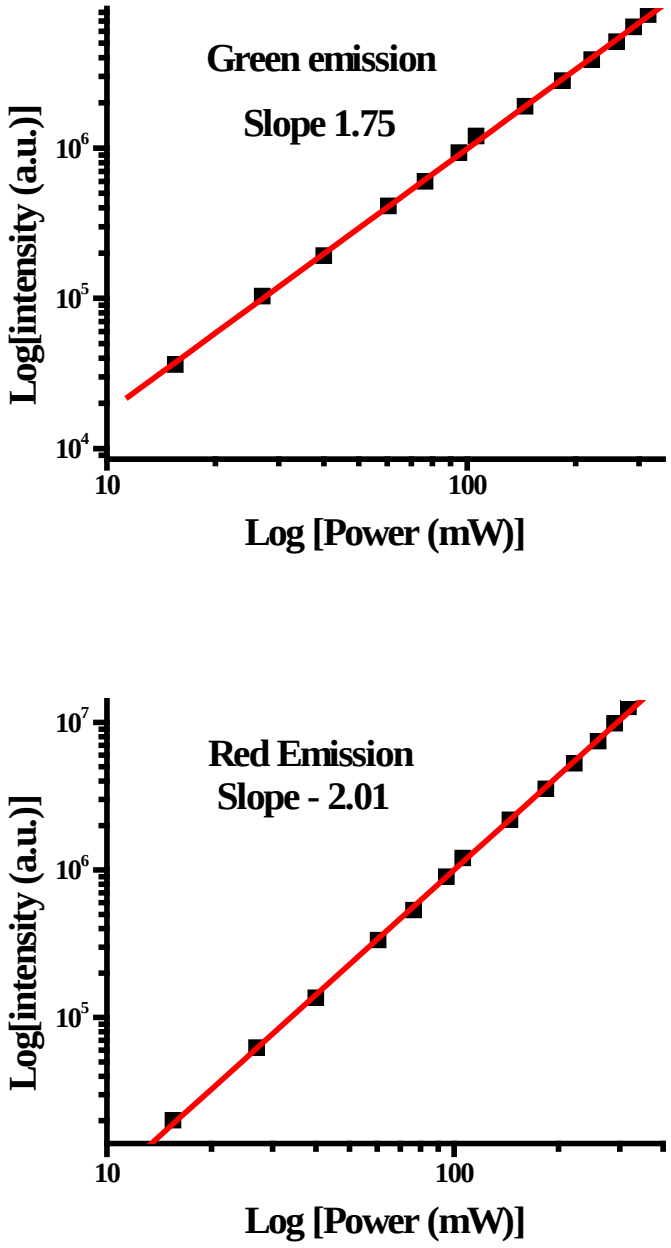

Figure B.5. Power Dependence curve for green and red emission from $NaYF_4$:Yb(20%):Er(2%) upon 980 nm excitation.

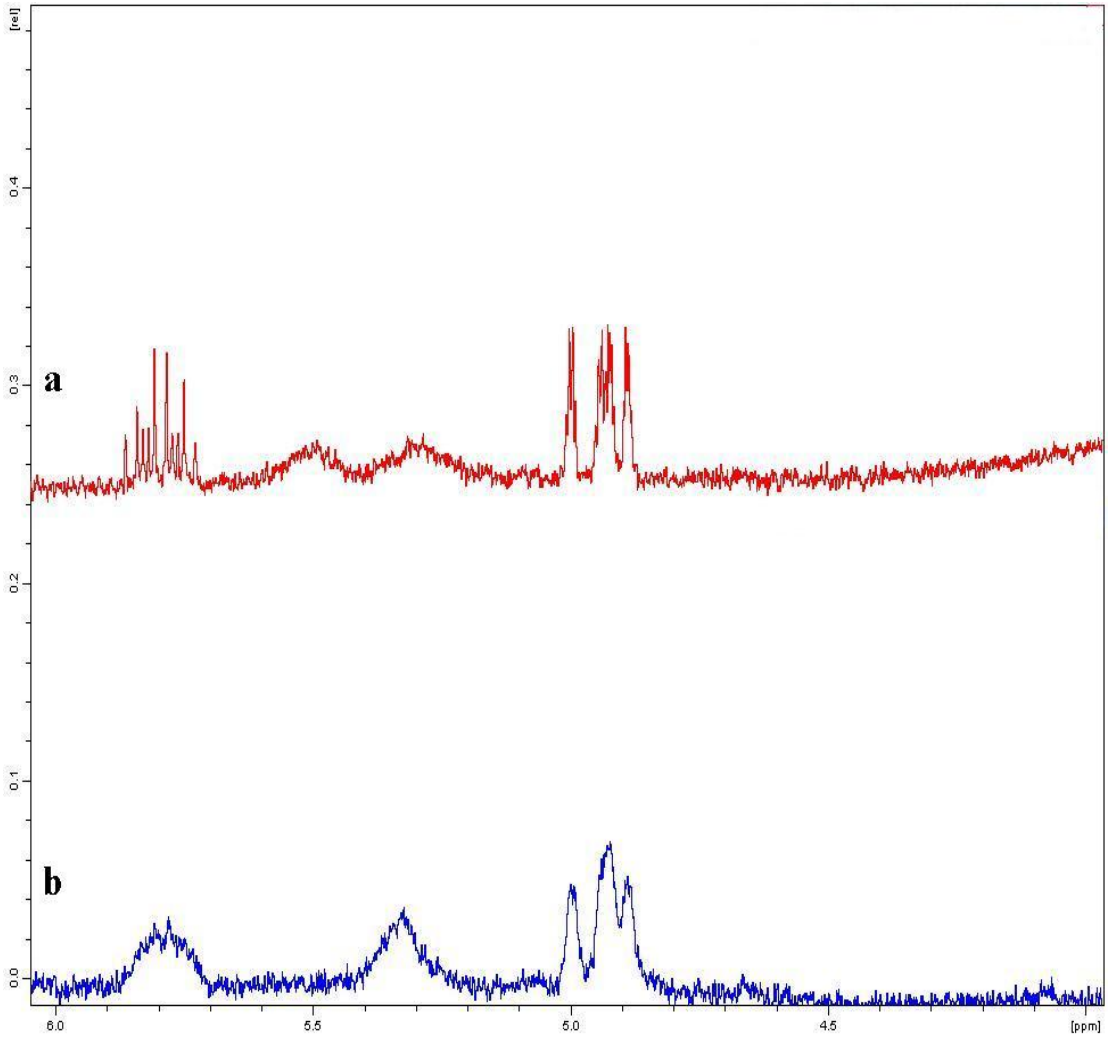

Figure B.6. ^{1}H NMR spectra of (a) polymer PMAO, and (b) nanocrystals-PMAO-BHMT in chloroform-d. The peaks at δ = 4.8-5.0 and 5.7-5.9 ppm correspond to –CH=CH2 coming from octadecene (impurity of PMAO).

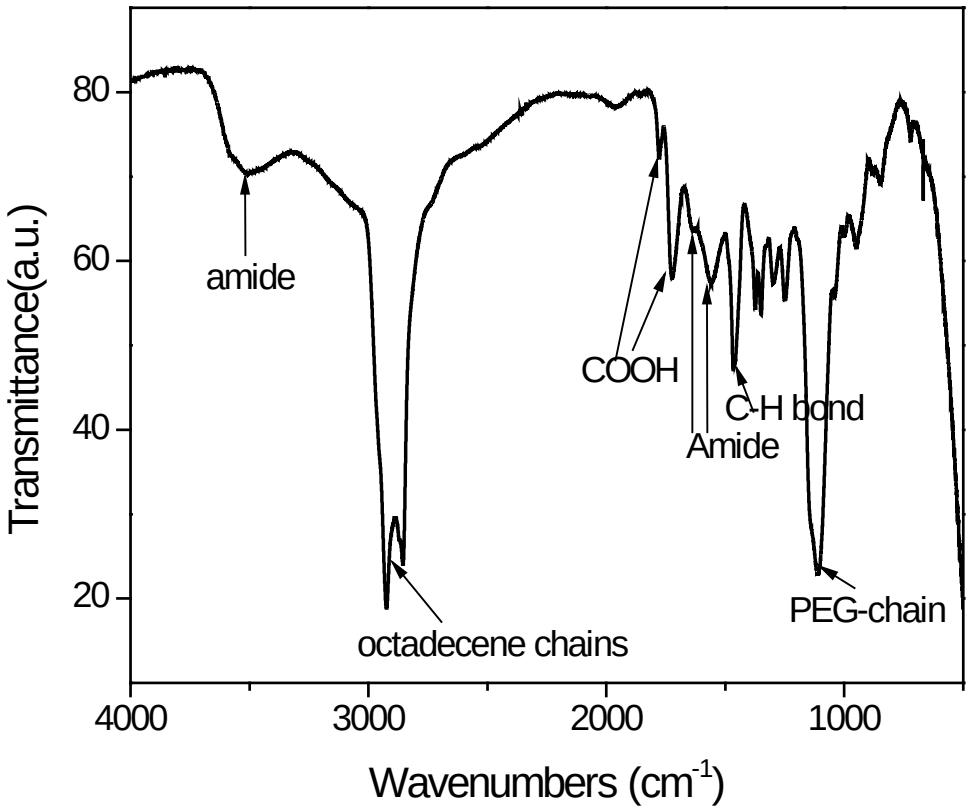

Figure B.7. FTIR spectrum of nanocrystals coated with PMAO-PEG-BHMT.

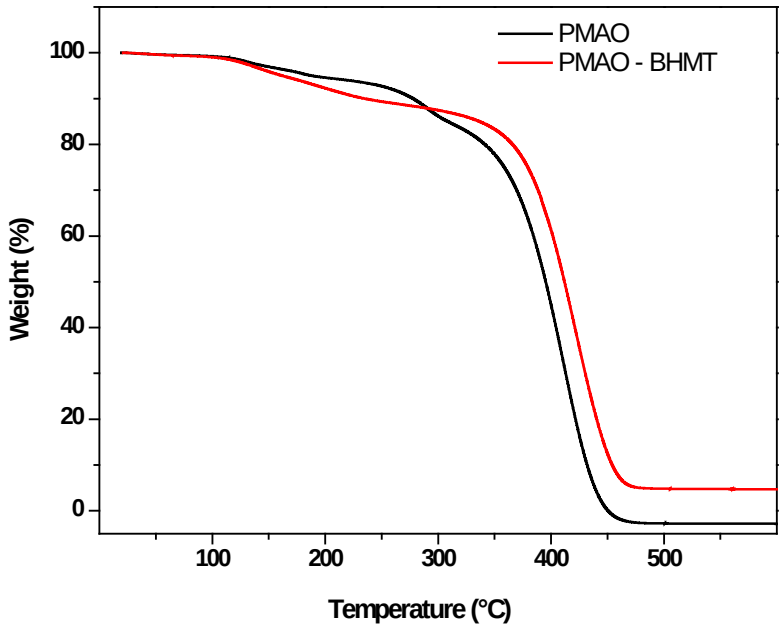

Figure B.8. Thermo gravimetric analysis (TGA) of PMAO and cross-linked PMAO-BHMT.

Appendix C. : Supporting information for chapter 4

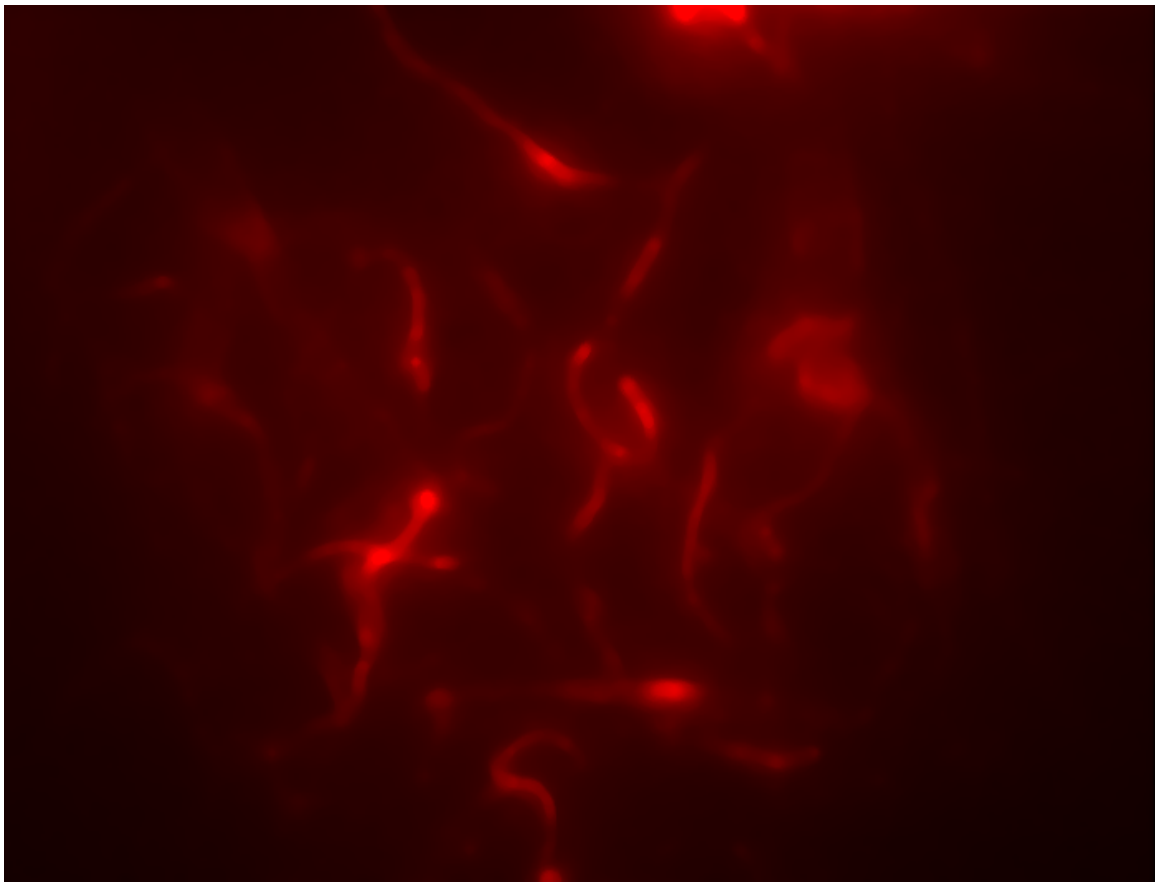

Figure C.1. Projection of blood vessels 100 µm deep inside the brain of a live mouse. The image shown here is a maximum intensity projection of 9 successive images taken at 10 µm step size along the z direction. The images were taken at 5 W/cm^2 with an exposure of 10 s at a gain of 34.7. The area of the image is 128/128 pixels with a 4x4 binning. 800 nm emission from Core/ shell/shell; $NaYF_4$:Yb(20%):Tm(2%)/$NaYF_4$:Yb(20%):Tm(2%)/$NaYF_4$ nanocrystals were used for imaging. The image is false colored.

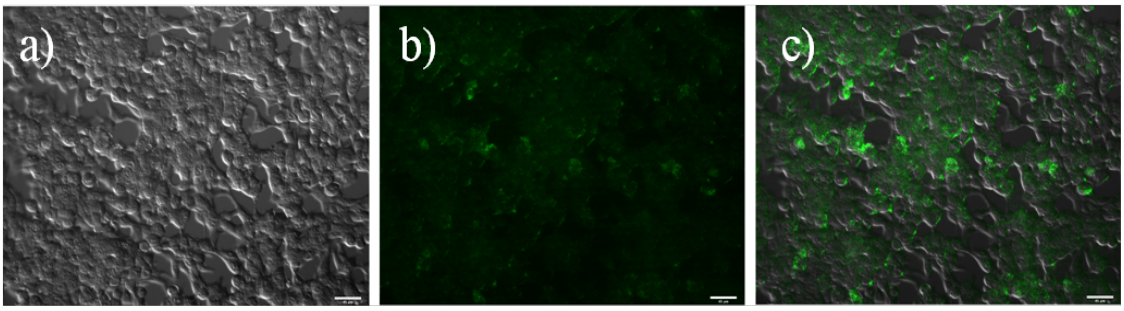

Figure C.2. LNCaP cell imaging (A) bright field, (B) under 980 nm excitation, and (C) overlap of bright field and green emission from PMAO-PEG-BHMT coated UCNPs.

Appendix D. : Supporting information for chapter 5

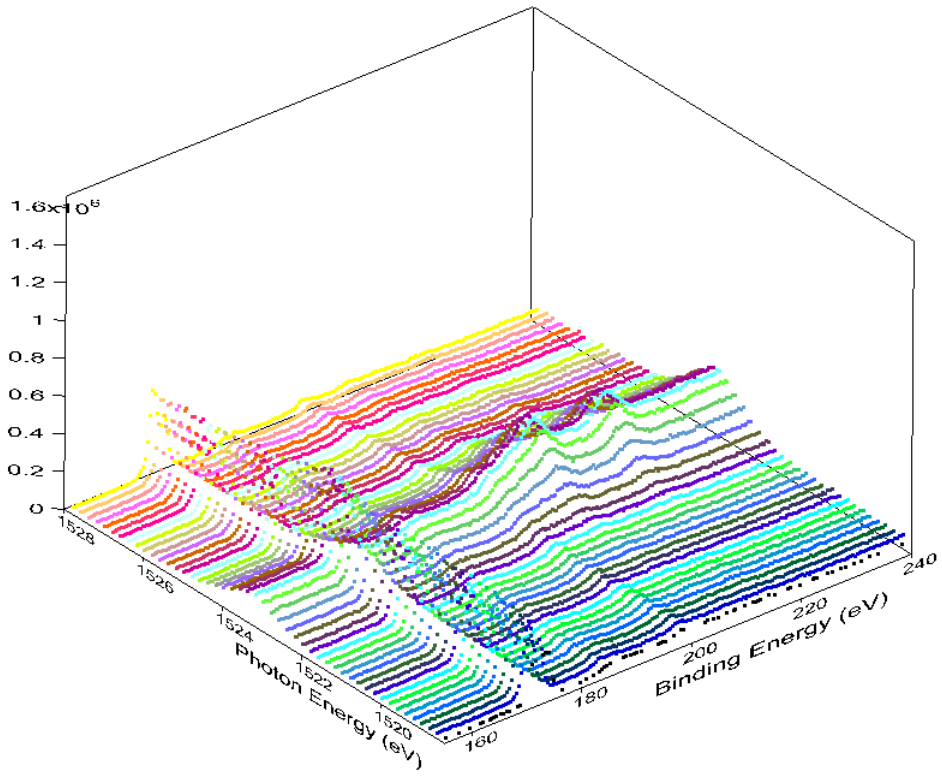

Figure D.1. 3-Dimensional graph depicting the 4d photoelectron peaks of $NaYF_4$:Yb(20%) at resonant and non-resonant photon energies. The peaks around 200 to 220 eV belong to 4d photoelectrons of Yb^{3+} ions. The peaks from 165 to 175 eV belong to the 3d photoelectrons of Y^{3+} ions. These spectra have not been corrected with respect to the reference gold spectrum.

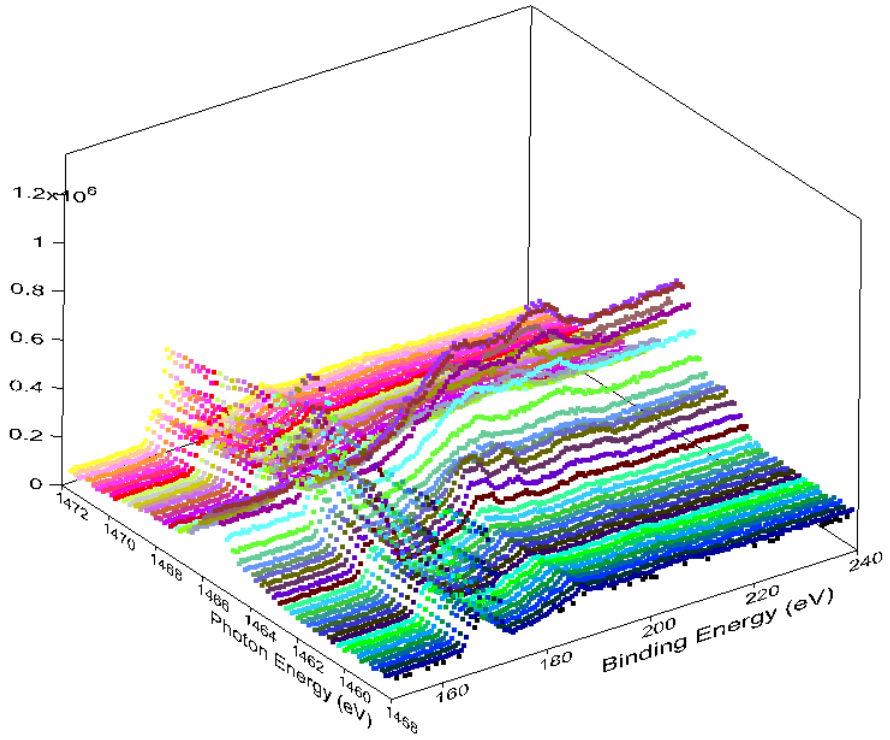

Figure D.2. 3-Dimensional graph depicting the 4d photoelectron peaks of to $NaYF_4$:Tm(20%) at resonant and non-resonant photon energies. The peaks around 193 to 207 eV belong to 4d photoelectrons of Tm^{3+} ions. The peaks from 165 to 175 eV belong to the 3d photoelectrons of Y^{3+} ions. These spectra have not been corrected with respect to the reference gold spectrum.

Appendix E. : Supporting information for chapter 6

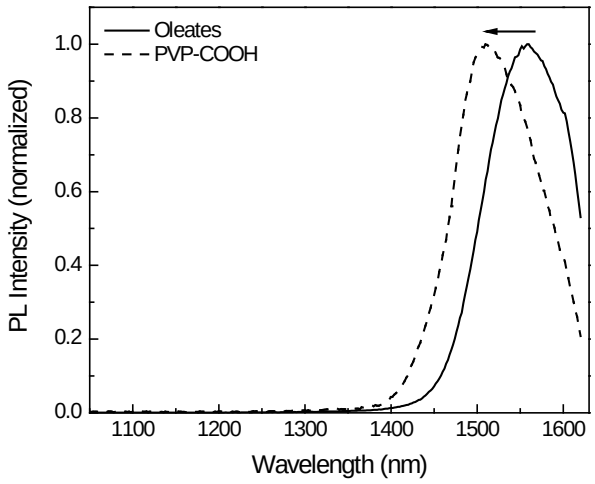

Figure E.1. Photoluminescence spectra of PbSe QDs before and after exchange in TCE and DMF, respectively.

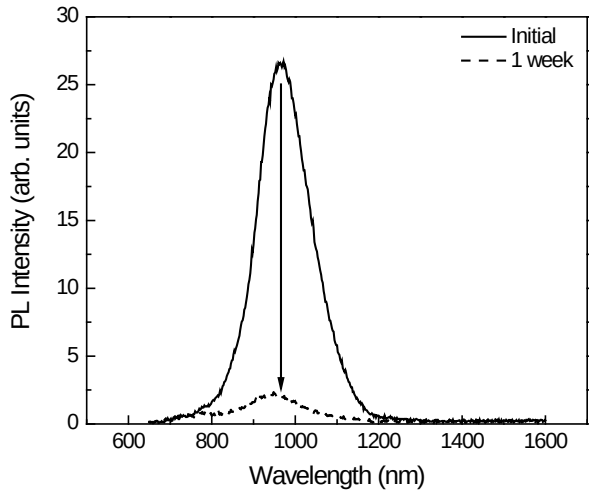

Figure E.2. Photoluminescence spectra of PVP coated PbSe QDs in ethanol.

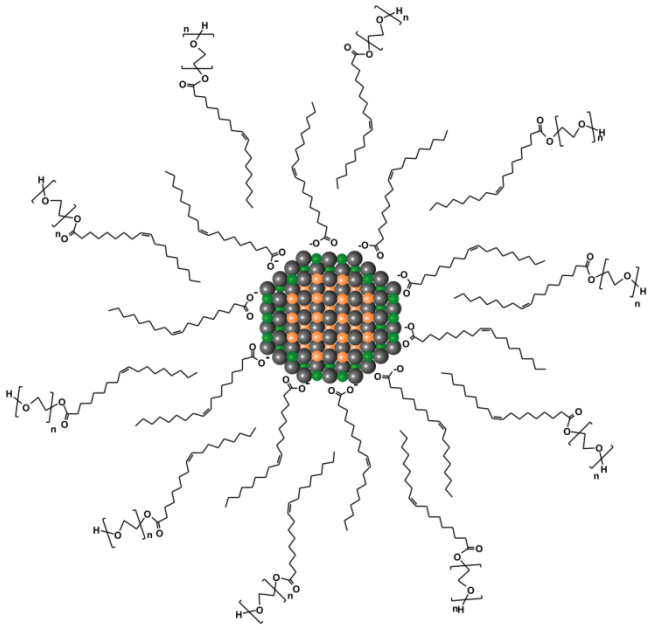

Figure E.3. Schematic representation of PEG-oleate intercalated QDs.

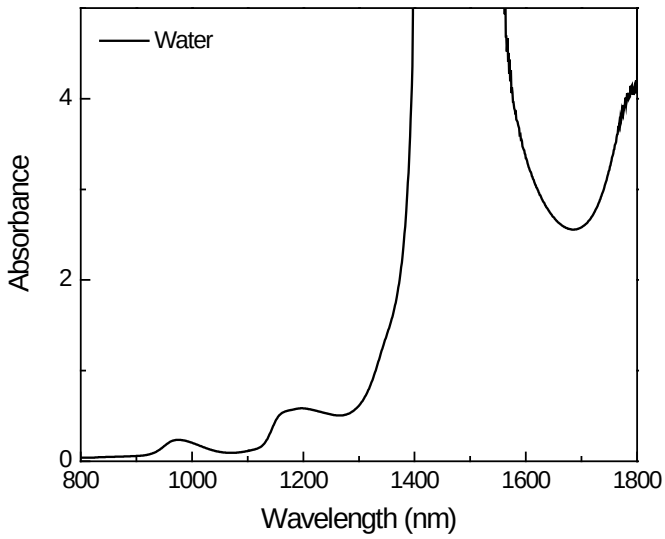

Figure E.4. Absorption spectrum of water.

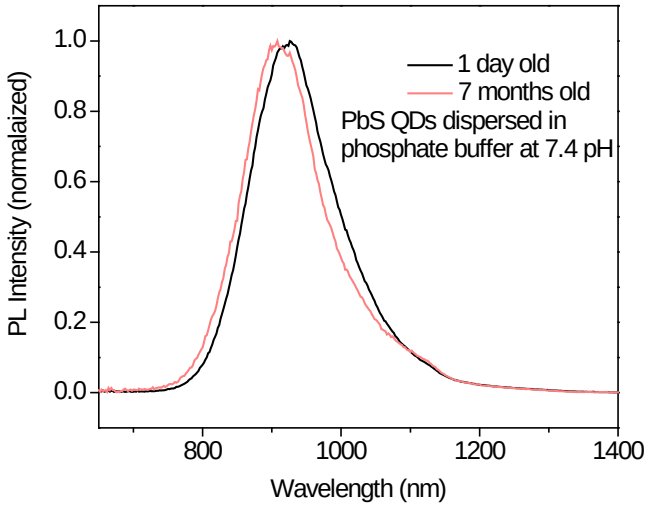

Figure E.5. Photoluminescence spectra of PMAO-PEG-BHMT coated PbS QDs dispersed in phosphate buffer at 7.4 pH.

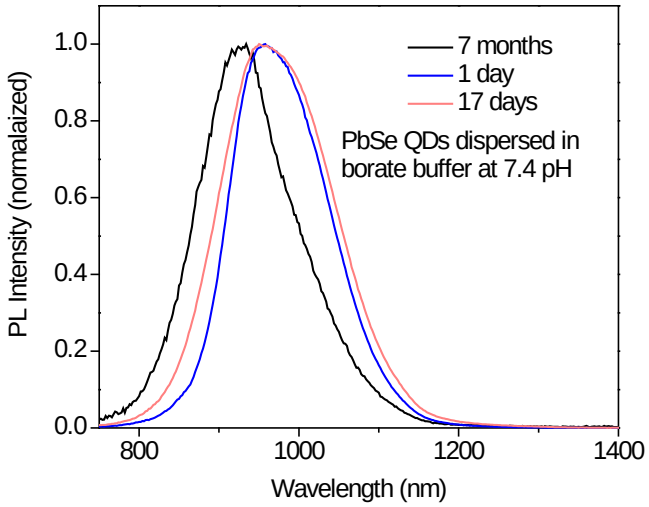

Figure E.6. Photoluminescence spectra of PMAO-PEG-BHMT coated PbS QDs dispersed in borate buffer at 8.6 pH.

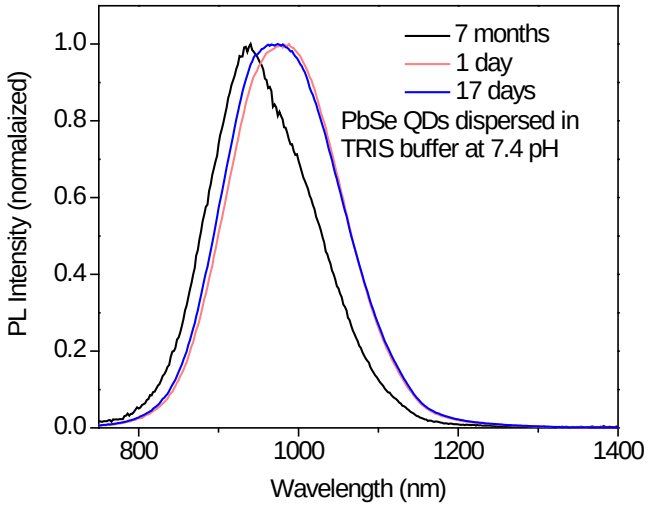

Figure E.7. Photoluminescence spectra of PMAO-PEG-BHMT coated PbS QDs dispersed in TRIS buffer at 7.4 pH.

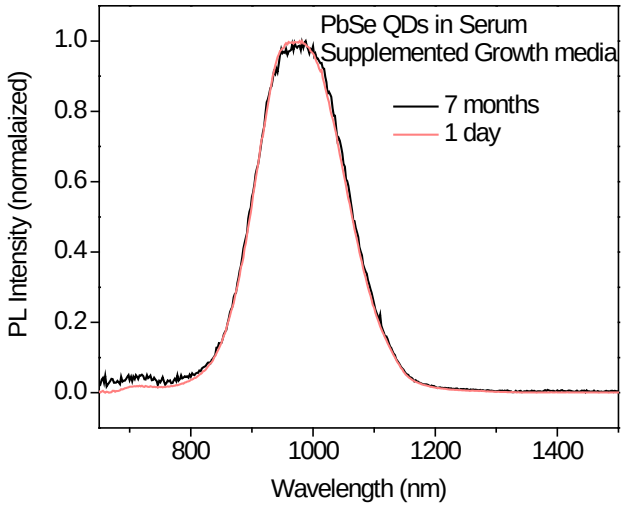

Figure E.8. Photoluminescence spectra of PMAO-PEG-BHMT coated PbSe QDs dispersed in serum-supplemented growth media.

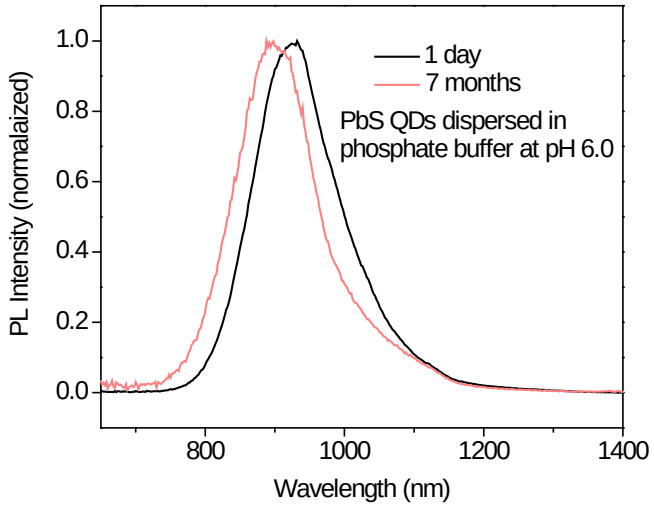

Figure E.9. Photoluminescence spectra of PMAO-PEG-BHMT coated PbS QDs dispersed in Phosphate buffer at pH 6.0.